Title
Liquid liquid phase separation and self-assembly of block copolymers

Author
Rizvi, Aoon

Publication Date
2023

UNIVERSITY OF CALIFORNIA,
IRVINE

Liquid-liquid Phase Separation and Self-assembly of Block copolymers

DISSERTATION

submitted in partial satisfaction of the requirements
for the degree of

DOCTOR OF PHILOSOPHY

in Chemistry

by

Aoon Rizvi

Thesis Committee:
Assistant Professor Joseph P. Patterson, Chair
Assistant Professor Seunghyun Sim
Professor Kenneth J. Shea
Professor Zhibin Guan

2023

DEDICATION

To my parents who have given me everything.

Table of Contents

LIST OF FIGURES

ACKNOWLEDGEMENTS

I would like to thank Joe Patterson for the support and guidance that has changed my life. I arrived at UC Irvine with a burning passion to do science, and in the last 5 years that passion has only increased, and I have gained tools to keep fueling the fire, thanks to you. I admire your perspective not just as a scientist, but as a mentor and a leader. It has truly been an honor to explore the world of science with you. Thank you for making my graduate school experience incredible.

Thank you to my lab mates who joined and initiated The Patterson lab together, Brooke, and Paul. I couldn't have asked for better friends, lab-mates, colleagues. Seeing you two motivated and inspired me and it has been a blast to work alongside you all.

Thanks to my committee members, Seu Sim, Zhibin Guan and Ken Shea. Thanks to Seu for always sharing words of encouragement and discussing ideas with me for possible collaborations. Thanks to Zhibin for meeting with me during my UCI visit and making me excited to attend Irvine. It has always been nice to interact with you in seminars or elsewhere. Thank you to Ken for helpful advice on navigating academia and letting me and other Patterson lab members use his lab equipment when we first started.

Thank you to my collaborators, Ben Schuster and Bruna Favetta who agreed to send me their proteins so I can explore the nanoscale structures of their condensates. Thank you, Bruna, for always finding excitement for this, I really appreciate it.

Thank you to Suzanne Blum for accepting my collaboration request at the very end of my PhD to use fluorescence microscopy methods and understand condensate behavior. Thank you, Pia, for carrying out these experiments and explaining to me what is going on.

Thank you to my undergraduate advisor Steve Zimmerman who inspired my initial interest in research and provided me with an opportunity to do research in his lab. Thank you, Steve, for being a role model and continuously supporting my journey as an academic.

Thank you to my friends that I made in graduate school, who were always (mostly) up for adventures with me in nature and elsewhere. Thank you, Cynthia, Mariana, Sarah, Alissa, Chris, Mooji, Dave, Ali, Sadie, Rain, Brooke, Pia. Thank you to the Camping Crew for always making the time to go out in the wilderness with me! Thanks to Girls Night for having me as an honorary member. Having you all as friends made graduate school so much more fun, and the pandemic survivable.

Thank you to Hola Adios Coffee shop, for being the most welcoming coffee shop with the kindest crew at the bar. Thank you, Ceci and Alex.

Thanks to my family who have supported my endeavors in graduate school, even when not understanding the appeal of it.

Some of the text of this dissertation is a reprint of the material as it appears in *Macromolecules, Chemical Reviews, and Nanoletters*. It is fairly used with permission according to the guidelines. All co-authors are mentioned at the beginning of each chapter.

Curriculum Vitae

A. Academic History

1. **Harper Community College** Aug 2014-May 2015
   Pre-requisite coursework to transfer to a 4-year institute.
2. **University of Illinois, Urbana Champaign** Aug 2015-May 2018
   B.S Specialized Chemistry, Research Advisor: Steven C. Zimmerman
3. **University of California, Irvine** Sept 2018-Jun 2023
   PhD Candidate, Research Advisor: Joseph P. Patterson

B. Publications

1. Junfeng Chen, **Aoon Rizvi**, Joseph Patterson, Craig Hawker. Discrete Libraries of Amphiphilic Poly(ethylene glycol) Graft Copolymers: Synthesis, Assembly and Bioactivity. *Journal of American Chemical Society* 2022, 144, 19466-19474.
2. **Aoon Rizvi**, Justin Mulvey, Joseph P Patterson. "Observation of Liquid–Liquid-Phase Separation and Vesicle Spreading during Supported Bilayer Formation via Liquid-Phase Transmission Electron Microscopy." *Nano Lett. 2021, 21, 24, 10325–10332*
3. **Aoon Rizvi**, Justin Mulvey, Rain Talsoig, Brooke Carpenter, Joseph P Patterson. A Close Look at Molecular Self-Assembly with the Transmission Electron Microscope. *Chem. Rev. 2021, 121, 22, 14232–14280*
4. **Aoon Rizvi**, Urja Patel, Alessandro Ianiro, Paul J Hurst, Jovany G Merham, Joseph P Patterson. Nonionic Block Copolymer Coacervates. *Macromolecules* 2020, 53 (14), 6078–6086.
5. Ephraim Morado, Douglas Ivanoff, Hsuan-Chin Wang, Alayna Johnson, Mara Paterson, Darius Daniels, **Aoon Rizvi**, Nancy Sottos, Steven C Zimmerman. End-of-life upcycling of robust polyurethanes using a room temperature, mechanism-based degradation *Nature Chemistry* 2023, 15, 569–577
6. Robert H Lambeth, **Aoon Rizvi**. Mechanical and Adhesive Properties of Hybrid Epoxy-Polyhydroxyurethane Network Polymers. *Polymer* 2019, 183, 121881.
7. Hsuan-Chin Wang, Joshua M Grolman, **Aoon Rizvi**, Grant S Hisao, Chad M Rienstra, Steven C Zimmerman. PH-Triggered Release from Polyamide Microcapsules Prepared by Interfacial Polymerization of a Simple Diester Monomer. *ACS Macro Lett*. 2017, 6 (3), 321–325

C. Fellowships and Awards

1. <u>Beckman Coulter Scholar</u>: Recognizing top PhD candidates as leaders in STEM.
2. <u>Lindau Nobel Laureate Delegate</u>: Selected as one of the representatives of the University of California to attend the annual Lindau Nobel Laureate meeting held in Germany.
3. <u>PRISM Scholar (Stanford University)</u>: Selected as a PRISM scholar to visit Stanford and present my work at three different labs to find the best fit. The programs' goal is to offer underrepresented groups opportunities to find a Postdoctoral home at Stanford.

4. UCI Chemistry Rowland Fellowship: For the original research proposal to develop living composite materials from block copolymers in collaboration with Prof. Seu Sim, 2021.
5. Achievement Rewards for College Scientists (ARCS Scholar Award) 2021: ARCS Scholar Awards are intended to recognize and reward UC Irvine's most academically superior doctoral students exhibiting outstanding promise as scientists, researchers, and leaders.
6. Undergraduate Thesis, Honors Award 2018
7. Oak Ridge Institute for Science and Education Research Fellow at United States Army Research Lab (2017).

D. Conferences and Presentations

03/29/2023	Invited Speaker: 23rd Annual ARCS Scholar Awards hosted by the Beckman Foundation
02/03/2023	Semi-Finalist: Grad Slam Competition UCI wide
10/11/2022	Invited Talk: *"Observation of Supported Bilayer formation"* Gordon Research Conference.
07/9/2022	Invited Talk: *"Synthetic Condensates of block copolymers"* Chemical, Applied, and Materials Physics Seminar for Biophysics and Biomaterial science at UC Irvine.
04/21/2022	Invited Talk: Young Macro Talks hosted by the University of Warwick and supported by the Polymer Chemistry divisions of the Royal Society of Chemistry "*Liquid-liquid phase separation and Coacervation of block copolymer solutions*"
12/16/2021	PacifiChem: A Creative vision for the future. Oral Presentation
12/08/2021	Invited Talk: National Institute of Science and Technology (NIST): Complex Fluids and Soft Matter Group Seminar.
8/11/2021	Virtual Polymer Physics Symposium 2021, APS. Oral Presentation
4/12/2021	American Chemical Society, Spring Meeting (Virtual). Oral Presentation
10/09/2020	"*Liquid-liquid phase separation in amphiphilic self-assembly"* Graduate Seminar at UC Irvine
1/26/2020	Gordon Research Conference, Liquid Phase Electron Microscopy, Poster
8/25/2019	American Chemical Society, Fall National Meeting. Poster
10/14/2017	ACS, Eastern Illinois Undergraduate Research Conference, Poster

E. Leadership and Service

1. Gordon Research Seminar Chair for Liquid Phase Electron Microscopy GRC (2022)
   Organizing and developing forward looking scientific program for an international audience. Appointing discussion leaders from the field to facilitate thought-provoking discussions. Raising funds from private sources to grant travel awards for early career participants. (https://www.grc.org/liquid-phase-electron-microscopy-grs-conference/2022/)
2. Materials Research Seminar Organizer

Initiated a student led seminar series which invites speakers of student interests and organizes networking sessions for materials focused students across Chemistry, Physics, Bio-Sciences and Engineering departments.

  - 8/11/2019 “Quantitative Control Over Electron Beam Nanochemistry During Liquid Cell TEM”, Taylor Woehl, University of Maryland
  - Hold due to covid-19 global pandemic.
  - 11/15/2021 “Cryo-EM for sensitive battery materials and interfaces”, Yuzhang Li, University of California, Los Angeles

3. <u>Local Chemistry Outreach</u>: Organized an all-day event for middle school kids from local districts to visit the Discovery Cube Science Museum in Orange County. Currently this event was sponsored by the Younger Chemists Committee and the UCI School of Physical Sciences Outreach office.
4. <u>Mentorship and Networking Panel at PacifiChem (12/2021)</u>
   Organized a mentorship panel in collaboration with the Younger Chemists Committee (YCC).
5. SoCal Undergraduate Chemistry Research Symposium Mentoring Panel (08/2021)
   Panelist for a career panel at the SoCal Undergraduate Research Symposium. Led discussions about graduate life and share my personal experiences as an undergraduate researcher.
6. SISTERS Outreach (UCR Chapter)
   Virtual outreach event organized with undergraduate mentors for highschoolers. The event included a laboratory tour via zoom and a demonstration of a color changing experiment, followed by a Q&A session.

F. Mentorship

<u>Graduate Student Mentor</u>: Mentoring 1st and 2nd year graduate students, developing research plans and academic plans with new students. Leading them to consider goals that areachievable in the beginning of their PhD. I organize monthly meetings to discuss progress and weekly shadowing time to learn laboratory skills. (2 Students)

<u>Departmental Mentor (CHEMUnity)</u>: Mentoring outside graduate students to navigate different stages of PhD and provide insight on career development. (2 students)

<u>Undergraduate Mentor</u>: Mentoring undergraduate students in the lab to gain research experience and career development. Provide insight on transition from undergraduate to graduate school. (3 Students)

G. Teaching

Lead Instructor of Organic Chemistry 51C (Summer 2022): Delivered lectures with handwritten notes and mechanisms for easier understanding of the subject. Managed a class of 120 students and provided academic guidance to students looking for extra help.

Guest Lecturer for Instrumental Analysis (California State University, Long Beach): “*Electron microscopy of soft and biological matter”* Engaged undergraduates with modern electron microscopy methods for understanding soft matter structure and dynamics.

Workshop Leader (Fall 2019): Liquid Phase TEM for Soft Matter at The UCI School for Transmission Electron Microscopy held by Irvine Materials Research Institute.

Teaching Assistant:

Organic Chemistry: My approach on teaching organic chemistry is focused on real world examples to inspire the students, because of this, four students from my class went on to join research labs.

General Chemistry: Held office hours for students and provided an environment where chemistry can be enjoyed by focusing on the parallels of daily life to general chemistry, i.e. the modification of cooking instructions depending on the altitude as due to waters boiling point changes.

Atmospheric Chemistry: Lead discussions and office hours for students and engaged them with local California laws that are in place to minimize the climate impact of our communities.

ABSTRACT OF THE DISSERTATION

Liquid-liquid phase separation and self-assembly of block copolymers

by

Aoon Rizvi

Doctorate in Chemistry

University of California, Irvine, 2023

Professor Joe Patterson, Chair

Liquid-liquid phase separation (LLPS) is a process through which a homogeneous phase separates into two or multiple phases. This process is observed in systems spanning biology and synthetic polymeric systems. The distinct phases have direct influence on things like material properties, morphology, and material interactions with other interfaces. In my research, I explore how phase separated droplets influence self-assembled polymer morphologies in solution and on solid substrates. I used techniques like cryogenic electron microscopy (cryo-EM), liquid phase electron microscopy (LP-EM), and optical microscopy to study my systems. I developed the first example of nonionic block copolymer coacervates and demonstrated how the coacervates encode morphological information towards the solid phase self-assembly. Using LPEM, I showed block copolymer coacervates are also intermediates during supported bilayer formation. This new mechanism of bilayer assembly should be beneficial for forming pristine supported bilayers. Additionally, I discovered the auto-confining effects within the phase separated droplets were shown to favor complex block copolymer morphologies that are usually accessed by inducing confinement of block copolymers in emulsions. Furthermore, I developed a model block copolymer system in which LLPS occurs during light-induced polymerization mimicking active biological processes. Lastly, I developed a workflow to image phase separated droplets of polymers or proteins using cryo-EM which enabled 2D and 3D nanoscale characterization. The collection of this work informs how phase separated droplets behave and influence block copolymer self-assembly.

.

Chapter 1: Introduction

This Chapter was adapted from a published article (**Aoon Rizvi,** Justin Mulvey, Rain Talsoig, Brooke Carpenter, Joseph P Patterson. A Close Look at Molecular Self-Assembly with the Transmission Electron Microscope. *Chem. Rev. 2021, 121, 22, 14232–142800*)

.

1.1 Self-Assembled Materials

Molecular self-assembly is the spontaneous organization of molecules into higher order structures.[1–3] The use of the term spontaneous is important as it indicates that the process of self-assembly has a negative free energy change. As such, self-assembly processes can be represented by a free energy landscape.[4] The free energy landscape describes all possible microstates (configurations) as a function of their free energy. Self-assembly processes are a change in the microstate, going from a high energy position in the free energy landscape to a lower energy position. The free energy landscape is determined by the thermodynamics of the system, which depends on parameters such as the molecular structure of the building blocks, the medium of self-assembly, and the temperature. Self-assembly processes are initiated by a change in the system parameters such that a new, lower energy microstate becomes accessible. A full understanding of a self-assembly process requires a description of the initial and final microstates as well as the mechanisms by which these microstates are connected. This complete understanding is essential for the rational design of functional self-assembled systems as their functionality is dependent on their structure and structural dynamics.

Self-assembly processes can be described by a complexity continuum. Simple processes consist of a small number of building blocks and microstates, assemble down a single pathway, evolve homogeneously (only one microstate is observed at each sampled time point), and form atomically precise structures that can be described by a few parameters. Complex processes can have multiple building blocks and microstates, assemble by multiple pathways, evolve heterogeneously, and form high dispersity structures that are described by many parameters. Self-assembly processes are studied throughout the chemical, biological, and materials sciences and have been applied in medicine, catalysis, separation science, energy conversion and storage, and sensing applications.[1–3] Common precursors for self-assembled materials include small molecules, polymers, and biological molecules. These building blocks range from a few angstroms to nanometers in size, while their assembled structures can range from the nanoscale to the macroscopic scale.[1,5] The assembly process can occur in 1, 2, or 3 dimensions (3D) and can take place over timescales that range from nanoseconds to multiple days.[6] The vast continuum of space, time, and complexity makes understanding self-assembly a grand challenge, requiring multiple experimental, computational, and theoretical methods. Within our method arsenal, the transmission electron microscope (TEM) stands out as unique for its ability to *discover, visualize, and quantify* self-assembly mechanisms and structural features with atomic resolution. Throughout the chapters of this thesis, the TEM will be a common tool used to understand self-assembly processes and characterized nanoscale structures.

1.2 Liquid-liquid phase separation

Liquid-liquid phase separation has been studied now in a wide range of self-assembling systems, including proteins, DNA, block copolymers, and small molecules. Liquid-liquid phase separated precursors can lead to solid self-assembled materials, but also stable phase separated droplets known as coacervates or condensates. The design and understanding of such systems is crucial to prepare biological analogues and new liquid phase polymeric materials. Furthermore, active systems in which the LLPS occurs by an ongoing chemical reaction is of great importance to mimic biological processes and develop active materials. Our understanding of phase separating systems is limited as the research on these materials has only taken off in the past decade. Many aspects of LLPS systems remain unresolved, including the internal organization of macromolecules and partitioning within the multiple phases.

1.3 Dissertation Overview

This dissertation focuses on the development and characterization of phase separated and self-assembled systems mainly made of block copolymers except for Chapter X where protein condensates were also studied. All chapters involve droplet formation of polymers or proteins in solution. In each chapter, LP-TEM or Cryo-EM is used to characterize the structure within droplets and the mechanism of droplet formation. A detailed discussion on the electron microscopy techniques can be found in my review article.[7]

Chapter 2 presents the discovery of non-ionic block copolymer coacervates. A general strategy to form coacervates from nonionic block copolymers by controlling the molecular structure and solvent composition was developed. The mechanism of coacervation is studied using a combination of optical microscopy and cryogenic and liquid phase electron microscopy, revealing a coalescence-driven growth process is also presented. Knowledge of the mechanism enabled the design of experiments where morphological information was encoded into the coacervate phase and developed into the solid phase. The results show that self-assembled materials can be formed with multiple morphologies from the nanoscale up to the macroscale by controlling the kinetics of the coacervation and self-assembly process. Prior to this publication, polymeric coacervates were mainly prepared using a combination of oppositely charged polyelectrolytes.

Chapter 3 is a mechanistic study of supported bilayer formation. Here, we studied the formation of block-copolymer-supported bilayers using LP-TEM. We observe two formation pathways that involve either liquid droplets or vesicles as intermediates toward supported bilayers. Quantitative image analysis methods were used to characterize vesicle spread rates and show the origin of defect formation in supported bilayers. Our results suggest that bilayer assembly methods that proceed via liquid droplet intermediates should be beneficial for forming pristine supported bilayers. Furthermore, supported bilayers inside the liquid cells may be used to image membrane interactions with proteins and nanoparticles in the future.

Chapter 4 presents a polymerization induced coacervation system. We used RAFT polymerization to develop a block copolymer that forms phase separated droplets as the polymerization progresses. We followed the reaction kinetics of this process and learned that the onset of LLPS does not affect the reaction kinetics as hypothesized. However, the apparent reaction rate increases dramatically when the droplets turn into solid like particles. Chapter 5 presents a new way to access “confined” assemblies of block copolymers based on the LLPS mediated self-assembly mechanism. We discovered that block copolymers can form complex morphologies during the solvent switch method, but traditionally these complex morphologies are only produced using a biphasic confinement protocol. We show that when the system undergoes LLPS there is an auto-confinement effect which leads to the formation of confined morphologies. We mapped out phase trajectories of polystyrene-block-poly acrylic acid in multiple solvent systems to modulate phase separation propensity. Using cryo-EM we characterized the final morphologies that were made by the solvent switch process.

Chapter 6 presents a method to use cryo-EM to visualize nanoscale structure within phase separated droplets. We developed a method that applies cryo-electron microscopy (EM) to investigate the internal structure of condensates *in vitro* at the nanoscale. By bypassing the drying of material for conventional EM, we preserve the internal organization of molecules. We tested a range of material preparation protocols, including varying the temperature, concentration, and buffer conditions of the solution, along with vitrification procedures. We are able to produce both micron-sized spherical droplets and thin films of condensed material that are amenable to cryo-EM imaging. We applied this method to study condensates composed of intrinsically disordered proteins, polyelectrolytes, and block copolymers. Our results reveal the internal organization of the different materials at the nanoscale. We anticipate the use of cryo-EM beyond single particle analysis to understand phase separation of intrinsically disordered proteins and other macromolecules.

Lastly, Chapter 7 is a summary of the intellectual progress this thesis has contributed to the understanding of phase separating systems. In which I offer some perspective on where I think the field is going and what kinds of questions are critical to answer for advancing our understanding of phase separating systems.

1.4 References

(1) Whitesides, G. M.; Grzybowski, B. Self-Assembly at All Scales. *Science* **2002**, *295* (5564), 2418–2421. https://doi.org/10.1126/science.1070821.
(2) Lehn, J.-M. Toward Self-Organization and Complex Matter. *Science* **2002**, *295* (5564), 2400–2403. https://doi.org/10.1126/science.1071063.
(3) Mattia, E.; Otto, S. Supramolecular Systems Chemistry. *Nature Nanotechnology* **2015**, *10* (2), 111–119. https://doi.org/10.1038/nnano.2014.337.

(4) Wales, D. J.; Bogdan, T. V. Potential Energy and Free Energy Landscapes. *J. Phys. Chem. B* **2006**, *110* (42), 20765–20776. https://doi.org/10.1021/jp0680544.

(5) Palermo, V.; Samorì, P. Molecular Self-Assembly across Multiple Length Scales. *Angewandte Chemie International Edition* **2007**, *46* (24), 4428–4432. https://doi.org/10.1002/anie.200700416.

(6) Frederix, P. W. J. M.; Patmanidis, I.; Marrink, S. J. Molecular Simulations of Self-Assembling Bio-Inspired Supramolecular Systems and Their Connection to Experiments. *Chem. Soc. Rev.* **2018**, *47* (10), 3470–3489. https://doi.org/10.1039/C8CS00040A.

(7) Rizvi, A.; Mulvey, J. T.; Carpenter, B. P.; Talosig, R.; Patterson, J. P. A Close Look at Molecular Self-Assembly with the Transmission Electron Microscope. *Chem. Rev.* **2021**. https://doi.org/10.1021/acs.chemrev.1c00189.

Chapter 2: Nonionic Block Copolymer Coacervates

This Chapter was adapted from a published article (**Aoon Rizvi**, Urja Patel, Alessandro Ianiro, Paul J Hurst, Jovany G Merham, Joseph P Patterson. Nonionic Block Copolymer Coacervates. *Macromolecules* 2020, 53 (14), 6078–6086)

.

2.1 Introduction

Coacervation, often used interchangeably with liquid-liquid phase separation, refers to the phase separation of a colloidal system into two liquid phases.[1–8] The phase more concentrated in the colloidal component is referred to as the coacervate, and the dilute phase is referred to as the equilibrium solution.[9] The most common colloidal components that form coacervates are proteins,[4] peptides[7], polyelectrolytes,[10] and mixtures of synthetic polymers.[11] The term complex coacervation is used when coacervates are formed using two oppositely charged colloidal components (e.g, polyelectrolytes),[10] whereas simple coacervation is used when coacervates are formed from a single component (e.g, proteins).[12] Simple coacervation is typically induced by changes in the solution temperature, pH, or the addition of a non-solvent.[13,14] Coacervates are important in biological,[15–17] and synthetic systems.[18,19] In general, the function of a coacervate is either to act as a compartment for storage, or as a precursor to a solid phase material.[20] Within the cell membranes, coacervates are formed from proteins and RNA molecules,[21] are known to organize cellular components,[22] and serve as nanoreactors for biochemical reactions.[23] Outside the cell, protein coacervation can be pathological[24], or functional[25,26], depending on the system. For example, coacervation of the protein tau is linked to multiple neurodegenerative diseases,[27] including Alzheimer's.[24] A functional role of coacervating proteins is seen in spider silk, where silk proteins form a coacervate precursor prior to the extrusion process that creates the silk fibers.[28] In both cases coacervation provides a concentrated precursor to the solid assembled protein structure. Coacervates made from biomacromolecules are widely used in fragrance,[29] pharmaceutical,[30,31] and the food industries,[32] and coacervates made from synthetic homopolymers have been used in the formation of microporous membranes.[33] More recently, coacervation has been used to direct the formation of nanostructures that find application in catalysis and drug delivery.[34–36] By designing complementary block copolymers with a polyelectrolyte block and a neutral block, coacervation can be used to drive the assembly of coacervate core micelles,[37–39] giving rise to a similar phase behavior that is seen in the amphiphilic self-assembly of non-ionic block copolymers.[40] We recently reported that coacervation can occur as an intermediate phase during the solvent switch self-assembly of non-ionic block amphiphilic copolymers.[41] Using liquid phase electron microscopy (LP-EM), we observed the formation of transient nanoscale liquid droplets that directed the assembly of the poly(ethylene oxide)-*block*-poly(caprolactone) (PEO-*b*-PCL) block copolymers into vesicles, influencing their size and membrane thickness. Our explanation for this observation was that during the solvent-switch process, a specific composition exists where liquid-liquid phase separation is more thermodynamically favorable than dissolution or self-assembly. The implication for this is that it should be possible to form thermodynamically stable coacervates using non-ionic block copolymer by controlling the solution composition. This would be a surprising result as the phase behavior of amphiphilic block copolymers in solution has been studied for decades,[40,42–45] and there have been no examples of block copolymer coacervates being formed during a solvent switch process reported to the best of our knowledge. Previous studies have reported macrophase separation of block copolymer solutions,[46,47] however, there exists no discussion about macrophase separation or coacervation as an intermediate phase in the self-assembly of block copolymers.

Here, we report the formation of thermodynamically stable block copolymer coacervates made from polyethylene oxide-*block*-poly methyl methacrylate (PEO-*b*-PMMA), poly dimethylacrylamide-*block*-poly methyl methacrylate (PDMA-*b*-PMMA) and PEO-*b*-PCL in mixtures of organic solutions and water. All block copolymers were synthesized using modified literature procedures (see supplementary section 2-i).[48] Using PEO-*b*-PMMA as a model system, we show that the thermodynamic phase behavior of the polymers is dependent on the solution composition, the polymer concentration, and the molecular weight of the PMMA block. We show that the coacervate phase can be used to confine the assembly process such that a single block copolymer (PEO_{45}-*b*-$PMMA_{300}$) can be assembled into nanoscale and micro-scale particles, hierarchically porous polymer membranes, and macroscopic polymer fibers, by controlling the formation of the coacervate intermediate. The structural features in the materials are controlled by both the coacervate intermediate and the molecular structure of the block copolymer, the latter providing control over phase separation at the nanoscale.[49] We also provide a theoretical model that shows how the concentration of polymer in the coacervate can be used to direct the morphology of the final nanoscale and microscale particles. These experiments provide a framework for designing coacervates using non-ionic block copolymers and selecting appropriate solution conditions. These coacervates could serve as compartments for storage or transportation, or be used as precursors to self-assembled materials, where the coacervate encodes structural features to be developed and incorporated into the self-assembled materials on demand. Furthermore, the results show the importance of considering the role that coacervation plays as an intermediate phase during the self-assembly of block copolymers using solvent switch processes.

2.2 RESULTS AND DISCUSSION:

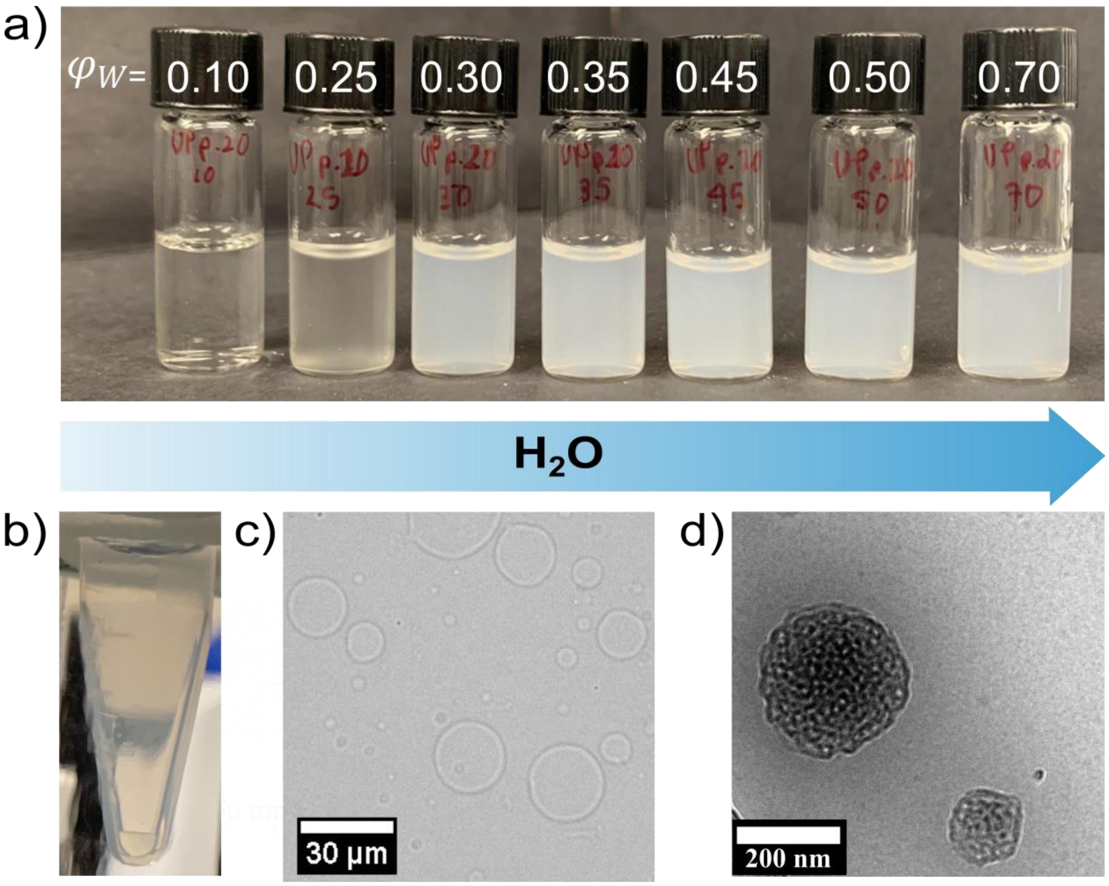

Figure 2.1: Phase behavior of PEO-*b*-PMMA diblock copolymers in water-dioxane mixtures: a) Photographs of PEO$_{45}$-*b*-PMMA$_{300}$ water-dioxane mixtures at 5 mg/mL, the water volume fractions (φ_W) are labeled on top of each sample. b) Photograph of $\varphi_W = 0.25$ sample showing the macro phase separated system post centrifugation. c) Optical micrograph of the coacervate sample at $\varphi_W = 0.25$ showing the micron sized liquid droplets. d) Cryo-TEM image of PEO$_{45}$-*b*-PMMA$_{300}$ bicontinuous nanoparticles.

.

Phase behavior of amphiphilic block copolymers in organic-water mixtures

The phase behavior of PEO-*b*-PMMA, PDMA-*b*-PMMA and PEO-*b*-PCL block copolymers was studied by preparing stock solutions of polymer in an organic solvent (dioxane, THF and acetone) and adding a fixed volume of water, to create solutions with a range of water volume fractions (φ_W) (Figure 1, S2 and supplementary section 2-ii). Note: the final polymer concentration is diluted from the stock solution to mimic a solvent switch self-assembly process.[40] Visual inspection of the solutions revealed three primary phases (Figures 1a), a homogeneous phase (clear solutions, φ_W<0.25), a coacervate phase (cloudy solutions, φ_W=0.25), and a self-assembled phase (blue solutions due to the Tyndall effect, φ_W>0.275). Centrifugation of the coacervate phase resulted in the formation of two macroscopic phase separated domains (Figure 1b). In general, the volume of the coacervate layer was ~10-20 µL for 1 mL samples. Vortexing the macroscopically phase separated solutions resulted in the reformation of micron-sized droplets, visualized by optical microscopy (Figure 1c). Cryogenic transmission electron microscopy (Cryo-TEM) of the self-assembled phase revealed nanoparticles (Figure 1d), where the morphology was dependent on the polymer concentration (as discussed later). Dynamic light scattering (DLS) of the clear solutions shows a number average hydrodynamic diameter of ~2 nm, consistent with a dissolved polymer (Figure S6). The qualitative explanation for these results is that coacervation is favored under weakly-amphiphilic conditions.[41,50] In solutions with low water content, both blocks are very soluble and the block copolymer is dissolved, i.e. no amphiphilicity. In solutions with high water content, the hydrophilic block is very soluble while the hydrophobic block is very insoluble. This high amphiphilicity drives the segregation of the two blocks leading to self-assembly .[40] In solutions with intermediate water content, the hydrophilic block is soluble and the hydrophobic block is sparingly soluble. This small difference in solubility is not sufficient to drive the block segregation, hence the block copolymers undergo coacervation. Quantitatively, the results can be explained by comparing the free energy densities of phase separation and micelle formation.[41,50] Previously, critical solvent composition where coacervation occurs ($\varphi_{\mathrm{S1}}^{\mathrm{crit}}$) has been derived by mapping the Flory-Huggins free energy of mixing[51] of a block copolymer in a binary solvent mixture into that of a homopolymer-solvent system.[41] Here we derive $\varphi_{\mathrm{S1}}^{\mathrm{crit}}$ from the derivatives of the copolymer and solvent chemical potentials[51] which results in the following equation (see supplementary section 3-ii).

$$\varphi_{\mathrm{S1}}^{\mathrm{crit}} = \frac{\left[\frac{N_{\mathrm{A}} + N_{\mathrm{B}} + N_{\mathrm{S}} + 2\sqrt{(N_{\mathrm{A}} + N_{\mathrm{B}})N_{\mathrm{S}}}}{2N_{\mathrm{S}}} + \frac{\chi_{\mathrm{AB}} N_{\mathrm{A}} N_{\mathrm{B}}}{N_{\mathrm{A}} + N_{\mathrm{B}}} - N_{\mathrm{A}}\chi_{\mathrm{AS2}} - N_{\mathrm{B}}\chi_{\mathrm{BS2}}\right]}{N_{\mathrm{A}}(\chi_{\mathrm{AS1}} - \chi_{\mathrm{AS2}}) + N_{\mathrm{B}}(\chi_{\mathrm{BS1}} - \chi_{\mathrm{BS2}})} \tag{1}$$

In equation (1), N_{A} and N_{B} are the chain length of the A (lyophilic) and B (lyophobic) blocks respectively, $N_{\mathrm{S}} = N_{\mathrm{S1}} = N_{\mathrm{S2}}$ represents the solvent size, which is assumed to be the same for both good (S2) and selective (S1) solvents, and the χ_{ij} terms are the Flory-Huggins interaction parameters between any two components *i* and *j.* The limitations of this model are that it does not account for the block nature of the polymer, polymer concentration (which is important for determining the critical point of phase separation)[52,53] or any kinetic effects in the phase behavior. However, the benefit of this model is that it is computationally simple and therefore large phase spaces can be explored quickly. Consequently, the model is useful as a back of the envelope calculation for guiding experimental work.

Using PEO-*b*-PMMA as a model system, experimental and theoretical phase diagrams were compared. The free energy densities of micelle formation were calculated as previously reported.[41,50] The phase behavior was explored as a function of the starting polymer concentration, PMMA block length, and water volume fraction, φ_W (Figure 2). As seen in the experimental phase diagrams, the phase space in which coacervation is favored increases when the hydrophobic content of the system is increased (Figure 2, a, c, e). This can be achieved by either increasing the polymer concentration or the PMMA block length. The calculated phase boundaries are not affected by the polymer concentration and therefore the theoretical phase boundaries presented in Figure 2 a, c, and e, are identical. Our experimental data shows there is indeed a critical concentration at which coacervation occurs, and that the theoretical model does not accurately reproduce the shape of the phase boundaries. These differences are likely in part due to the limitations mentioned above, but also due to the fact that χ_{ij} parameters are known to be effectively concentration-dependent,[54] therefore it is likely that some effective χ_{ij} parameters would more accurately describe the thermodynamics of the phase behavior. Despite the limitations of the model, the predicted and experimental phase boundaries are in good agreement, validating our theory that the phase behavior of block copolymers can be controlled by both the molecular structure and solution composition. The theoretical phase diagram was generated using a python script which has been included in the supplementary information.

The mass ratio of polymer between the coacervate and equilibrium solution (supernatant) was determined by decanting the top layer, evaporating the solvents and measuring the remaining polymer mass (Figure 2 b, d, f). In general, it appears that the mass ratio is a function of the position in the phase space with respect to the phase boundaries, the polymer concentration, and the polymer molecular structure. For a single block copolymer at a fixed starting concentration, the volume fraction of polymer in the equilibrium phase decreases as the water content increases (i.e. the system is close to the phase boundary where self-assembly will occur). PEO_{45}-b-$PMMA_{400}$ at 10 mg mL^{-1} starting concentration, formed the coacervate with the lowest volume fraction of polymer in the equilibrium solution (< 3 %), comparable to other coacervate systems.[4,36] The extent of the two solvents partitioning amongst the two phases would be of interest here, however, for our current system we did not study this property. Future studies will be published regarding that subject matter. To test the pathway dependence on coacervate formation, we performed two experiments. 1) dioxane was added to solutions containing self-assembled particles, 2) solid polymer was directly dispersed in solutions where coacervation takes place. In both cases, the sample formed coacervates identical to those formed using the solvent switch procedure (Figure S1). This indicates that coacervate formation is under thermodynamic control in the studied conditions.[55,56] As discussed later, this is in contrast to the self-assembled domain, which is under kinetic control.

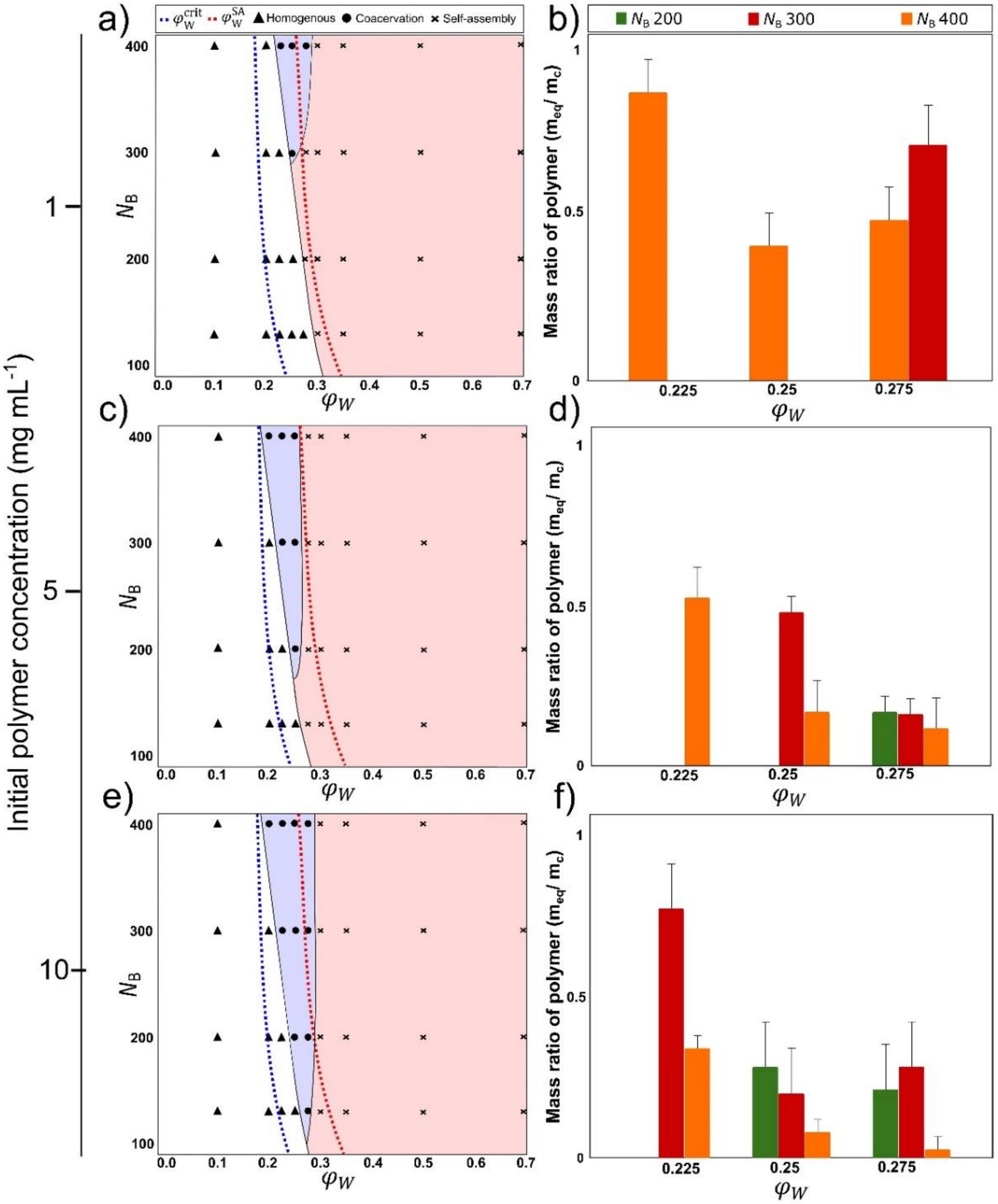

Figure 2.2: Comparison of calculated and experimental phase diagrams of PEO$_{45}$-*b*-PMMA$_{x.}$ a, c and e show phase diagrams as a function of PMMA block length (N_B) and the volume fraction of water φ_W for initial polymer concentrations of 1, 5, and 10 mg mL-1 respectively. The data points (triangles, circles, crosses) mark the experimental data points. The regions of the phase diagram (white, blue, red) were drawn based on these data points. The dashed lines, blue and red, show the calculated critical water volume fraction for coacervation ($\varphi_w^{\mathrm{crit}}$) and self-assembly($\varphi_{\mathrm{w}}^{\mathrm{SA}}$) respectively. ($\varphi_w^{\mathrm{crit}}$) is calculated using equation 1 and ($\varphi_{\mathrm{w}}^{\mathrm{SA}}$) is calculated as described in previous reports.[41,50] Graphs b, d and f show the experimental data and present the distribution of polymer between the coacervate phase and the equilibrium phase as a mass ratio of polymer $m_{\mathrm{equilibirium}}/m_{\mathrm{coacervate}}$ ($m_{\mathrm{eq}}/m_{\mathrm{c}}$) for samples that undergo coacervation

.

The mechanism of PEO-*b*-PMMA block copolymer coacervation

A combination of LP-EM, Cryo-TEM and optical microscopy was used to study the mechanism of coacervation. In general, experiments were performed by preparing solutions close to, or inside, the coacervation region of the phase diagram. Sample preparation for analysis by all techniques can result in partial evaporation of the solutions and the application of shear forces, both of which will likely affect the

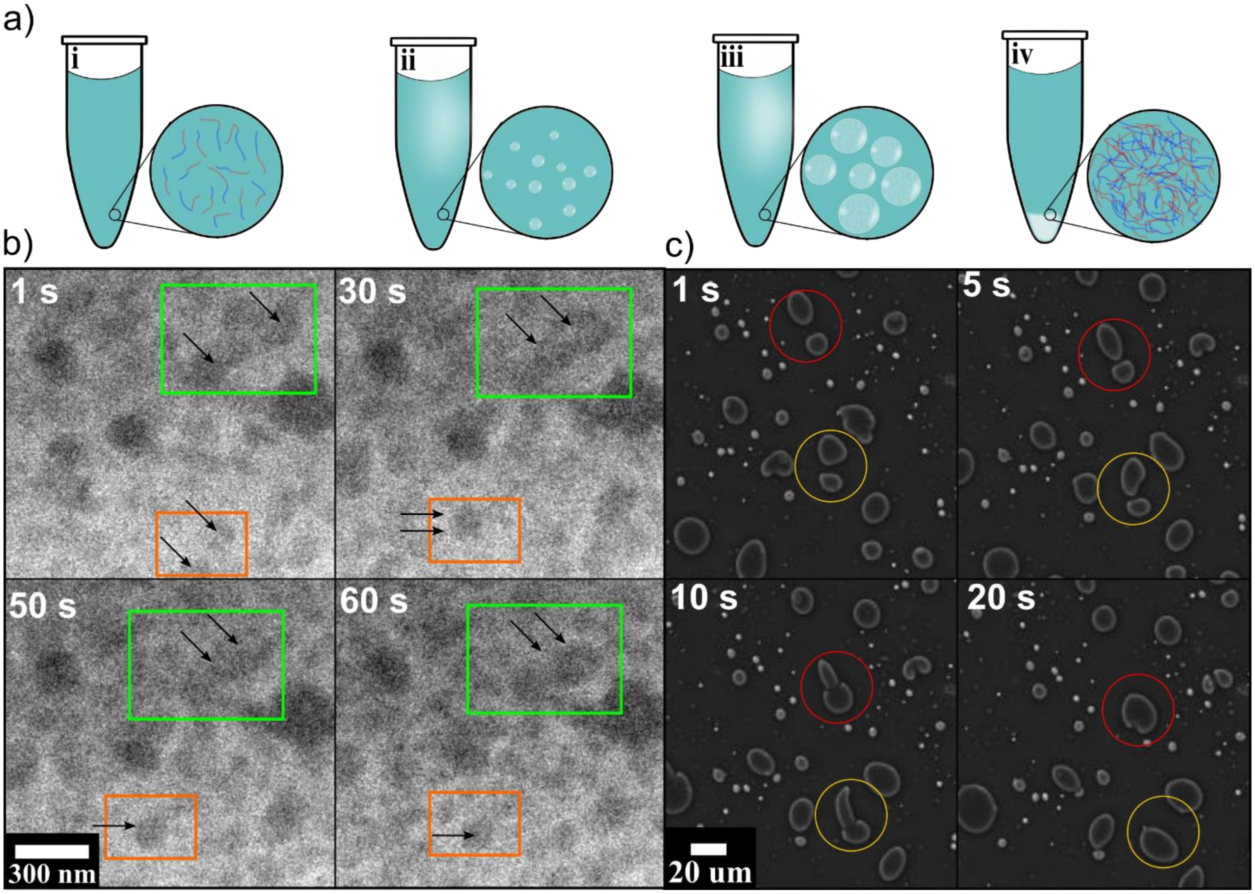

Figure 2.3: Coacervation mechanism of PEO_{45}-*b*-PMMA in dioxane water mixtures. a) Schematic of the coacervation mechanism from dissolve unimers to nano droplets, microdroplets and a macro phase separated system. b) Snap shots from the LP-TEM movie (Supplementary Movie 1) of nano droplets formed in-situ (PEO_{45}-*b*-$PMMA_{300}$ in water dioxane mixture) and undergoing coalescence. c) Snapshots from the phase contrast microscopy movie (Supplementary Movie 2) of micro droplets (PEO_{45}-*b*-$PMMA_{300}$ in φ_W = 0.25 water-dioxane mixture) undergoing coalescence.

coacervation process.[57–59] Consequently, it is challenging to precisely control the onset of coacervation and make quantitative measurements across all scales of the coacervation process, however, the collective experiments indicate that the mechanism of coacervation occurs through the formation of nanoscale droplets, (consistent with our previous observations for PEO-*b*-PCL),[41] which then grow to form microdroplets via coalescence, and eventually sediment under gravity to form a macroscopic two phase system. In our previous study of block copolymer coacervation by LPEM we did not observe any coalescence, however in our previous experiments the coacervates were fixed to the surface of the liquid cell which prevented droplet interaction and therefore coalescence. In the experiments reported here for PEO-*b*-PMMA we observed droplet growth via coalescence events at both the nanoscale, using liquid phase EM (Figure 3b, Movie S1), and at the microscale, using optical microscopy (Figure 3c, Movie S2), see supplementary information for experimental details. Cryo-TEM experiments also support a droplet growth via fusion, as we observed anisotropic vesicles with one membrane (Figure S3, see supplementary section 2-x). This indicates that the fusion event takes place prior to the self-assembly while the polymer is in the coacervate form. Furthermore, we also observed many anisotropic microparticles by SEM (Figure S5). Although these data provide strong evidence for a fusion driven growth mechanism, we cannot rule out that unimer addition also plays a role in the conversion of the nanodroplets to microdroplets. Therefore, further work is needed to determine the concentration of polymer inside the nanoscale and microscale coacervate droplets in the pre-equilibrium stage. When the microdroplets become sufficiently large, they begin to sediment and form a macroscopically phase separated system. The formation of two distinct layers takes about 15 hours to complete, however, centrifugation at 10,000 g for 10 minutes provided the same result. It is important to note that the data presented in Figure 2 b, d and f was obtained after centrifugation.

Using block copolymer coacervates to control self-assembly over multiple length scales

After establishing that coacervates are precursors to self-assembled structures, and that coacervates evolve in size via coalescence, we prepared self-assembled materials at multiple length scales by controlling the size of the coacervate phase and driving the system towards self-assembly with the addition of excess water. The addition of excess water changes the solvent composition so that self-assembly becomes thermodynamically favorable. Using PEO_{45}-*b*-$PMMA_{300}$ as a model system, macroscopic pellets, micron sized particles, and nanoscale particles were prepared, using the corresponding coacervate phase as an intermediate (Figure 4). The macroscopic pellet was cut open and imaged by scanning electron microscopy (SEM), revealing a porous polymer network (Figure 4c). Our hypothesis is that the structure in the coacervate creates the porous structure, and that upon addition of excess water, the block copolymer phase separates to impart nanoscale structure within the network (although we could not visualize the nanoscale morphology of the network directly). The micron sized particles were imaged by SEM, revealing an average size of 3±2 µm in diameter (Figure S10) with particle sizes as large as 10 µm. The microparticles displayed a porous surface structure, with average pore sizes of 42±10 nm (Figure S11) and an average pore-to-pore spacing of ~ 83±49 nm. Optimization of the microdroplet to microparticle assembly method, for example, using microfluidic devices would result in the creation of microparticles with a narrow size distribution.[60] The pore diameter and pore to pore separation distance are not consistent with a classical block copolymer bicontinuous structure, (see supplementary section 3-i). Consequently, our hypothesis is that the pore structure is determined by the assembly mechanisms as described in the following section. The nanoscale particles were imaged in water by cryo-TEM revealing an average size of 110±50 nm (Figure S8) and a morphology consistent with a bicontinuous phase [61,62]. The nanopores on the bicontinuous sphere were the average size of 14 ± 3 nm (Figure S9), consistent with the molecular structure of the block copolymer and previous examples of block copolymer bicontinuous particles.[63]

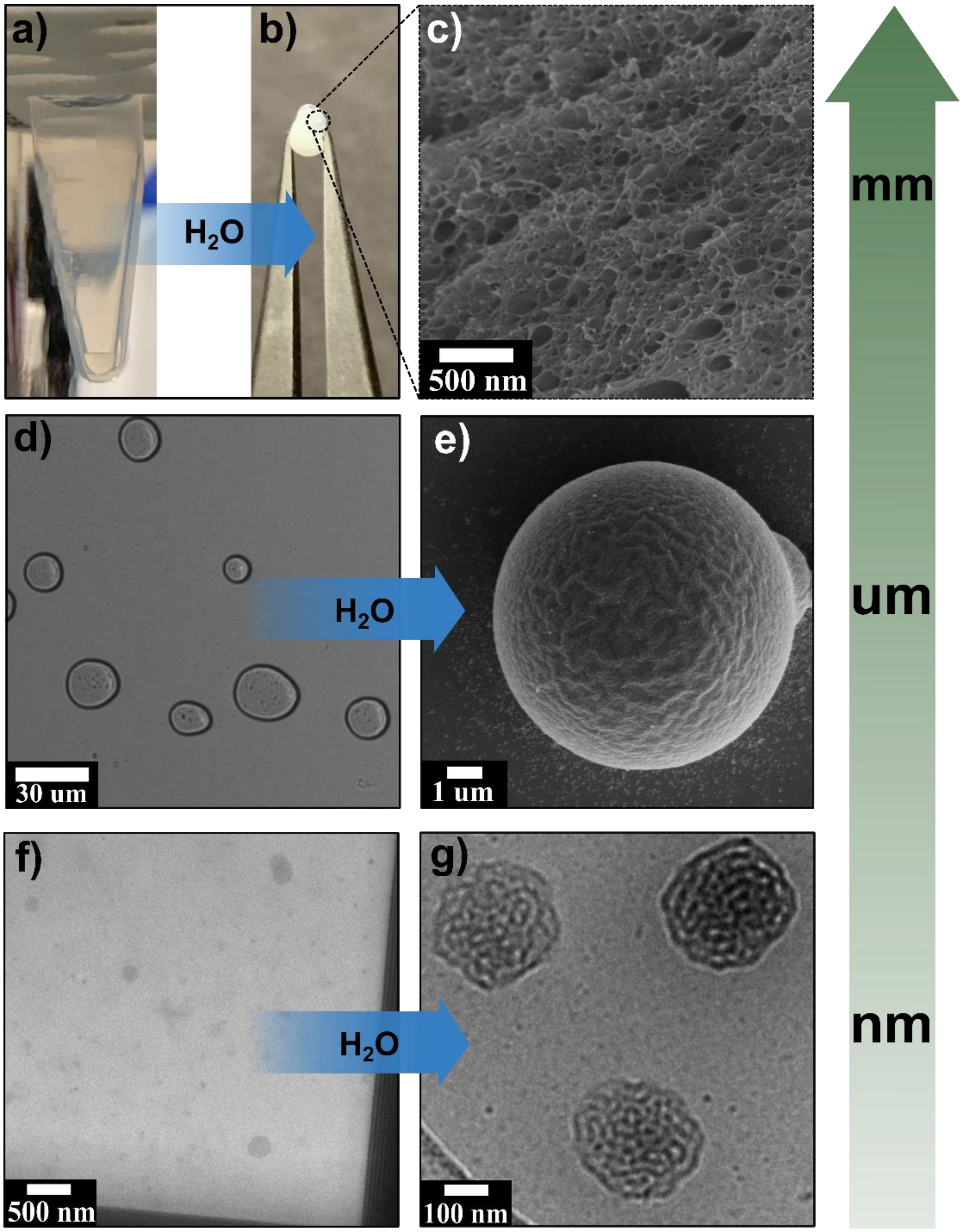

Figure 2.4: Macroscale to nanoscale self-assembly of PEO$_{45}$-*b*-PMMA$_{300}$. a) Photograph of a macro phase separated coacervate solution of PEO$_{45}$-*b*-PMMA$_{300}$ at φ_W = 0.25 in dioxane. b) Photograph of a millimeter size pellet formed by driving the coacervate phase to self-assembly via excess water addition. c) SEM image of a cross section of the pellet formed showing the bicontinuous microstructure within the self-assembled pellet. d) Bright-field optical microscopy image of the dispersed coacervate droplets of PEO$_{45}$-*b*-PMMA$_{300}$ at φ_W = 0.25 in dioxane mixture. e) SEM image of the microparticles self-assembled from the dispersed coacervate solution via excess water addition. f) In-situ TEM image of nano-coacervates formed using PEO$_{45}$-*b*-PMMA$_{300}$. g) Cryo-TEM image of bicontinuous structures formed at φ_W > 0.3 water in dioxane on the Cryo-TEM grid.

.

The results show that coacervation is a powerful method to control the self-assembly of block copolymers into particles over nanoscale to macroscopic length scales. Phase separated systems, like complex coacervates of polyelectrolytes and engineered proteins, have been used to make synthetic fibers by simply pulling fibers from the coacervate phase or electrospinning the phase separated solution.[28,64] Inspired by these previous works, we wanted to test if we could form fibers from our non-ionic block copolymer coacervates. The coacervate phase was taken on a glass slide and a pipette tip was used to pull fibers from the solution (Figure 5a). Pulling fibers from the coacervate resulted in the formation of a solid material due to the evaporation of the solvent, in contrast to our previous experiments where the formation of self-assembled structures was driven by changing the solution composition. SEM revealed fibers with a

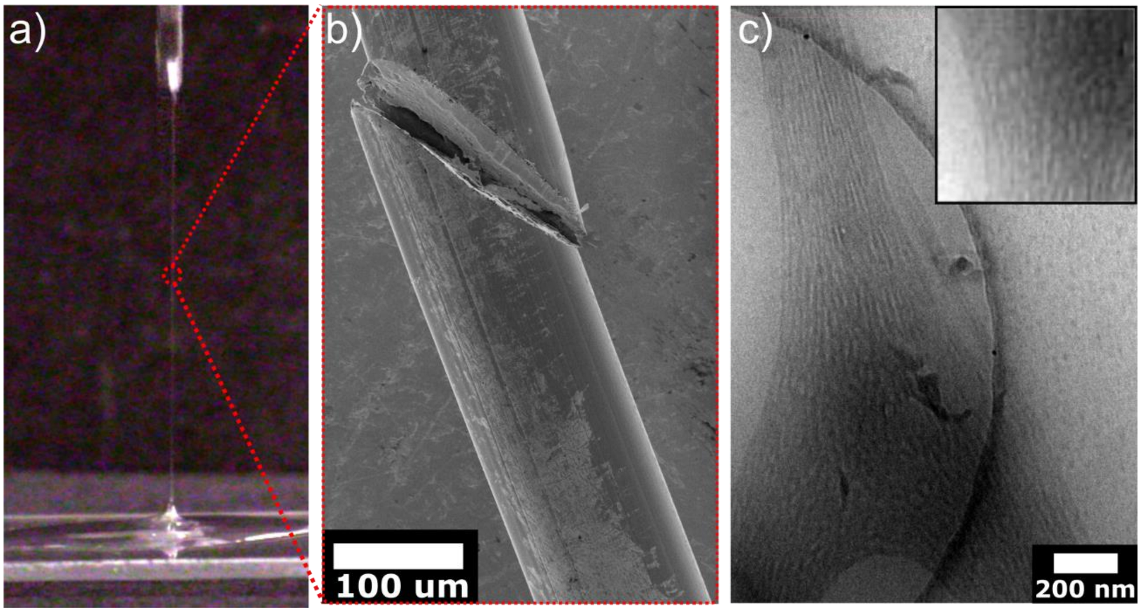

Figure 2.5: Fiber formation from PEO$_{45}$-*b*-PMMA$_{300}$ coacervate solution. a) Photograph of fiber formation as it is being pulled out of a concentration coacervate solution from a glass slide. b) SEM image of the fiber formed showing smooth surface and dense interior of the fibers. C) Cryo-TEM image of a fiber formed on the TEM grid during sample preparation, inset shows porous internal structure of the fibers (see supplementary section 2-x).

range of diameters (~ 60 µm) and a smooth surface structure (Figure 5b). Cryo-TEM of the fibers revealed a nanoscale porous structure within the fibers (Figure 5c). Control experiments were performed using the same block copolymer (PEO$_{45}$-b-PMMA$_{300}$) as a homogenous solution (φ_W < 0.25) and a nanoparticle solution (φ_W > 0.30). In both cases, it was not possible to pull fibers from the solution.

The role of polymer concentration in the mechanisms of block copolymer self-assembly from a coacervate intermediate

Cryo-TEM was used to image self-assembled particles formed by a solvent switch process, using PEO-*b*-PMMA$_{300}$ at initial polymer concentrations of 5 and 1 mg mL^{-1} (see supporting information sections 2-ix,2x for more details). In both samples, a mixture of morphologies was observed which included hemi-vesicles, vesicles and bicontinuous particles (Figure 6, Figure S4). Our hypothesis is that for block copolymer self-assembly processes that proceed via a coacervate intermediate, the morphology of the particles is dependent on the volume fraction of the polymer within the liquid droplet. It is important to recognize that if coacervation occurs as an intermediate phase during the solvent switch process, it is only possible to form nanoparticles by kinetically controlling the coacervate intermediate. As the coacervates in the nano-scale have not reached equilibrium, the concentrations within the droplets will likely vary stochastically. However, it is reasonable to assume that a lower starting polymer concentration will result in the formation of nano-scale coacervates with, on average, a lower concentration of polymer which could result in the range of morphologies seen in Figure 6. In the coacervate phase, the polymer chains will be homogeneously distributed throughout the liquid droplet. Upon the increase of water in the local environment of the droplet, where self-assembly is favored, the polymer chains are forced to reorganize in the confined space of the coacervate droplet. In addition to our previous work,[41] Wong et al. have also recently reported a droplet precursor during the solvent switch self-assembly of a block copolymer.[65] This is analogous to the self-assembly of polymers within phase separated liquids,[66] such as oil/water emulsions.[67,68]

Our previous LPEM observations showed that the polymer chains can assemble at the interface between the droplet and the bulk environment.[41] If the polymer volume fraction is insufficient to saturate the surface, a hemi-vesicle or porous vesicle will be formed (Figure 6a and S5). If the volume fraction of polymer chains in the droplet is sufficient to saturate the interfacial region, then the final structure formed will be hollow (e.g. a vesicle, Figure 6b). If the volume fraction of polymer chains within the droplet is more than sufficient to saturate the surface, then the final structures will be non-hollow morphologies (e.g. a bicontinuous structure, Figure 6c and Figure S4, further discussion is provided in the supplementary information). This can be described quantitatively using a geometric model for AB type block copolymers (where B is the solvophobic block) as follows:

The volume occupied by the B blocks in an AB block copolymer coacervate droplet can be expressed as

$$V_{\mathrm{B}}^{\mathrm{d}} = \frac{4}{3}\pi R_{\mathrm{d}}^{3}\varphi_{\mathrm{B}}^{\mathrm{d}}, \qquad (1)$$

where $\varphi_{\mathrm{B}}^{\mathrm{d}}$ is the polymer volume fraction in the droplet and $R_{\mathrm{d}}$is the droplet radius.

The volume of B blocks in the B-rich domain of a block copolymer bilayer is given by

$$V_{\mathrm{B}}^{\mathrm{v}} \approx SL\varphi_{\mathrm{B}}^{\mathrm{v}}, \tag{2}$$

with S and L representing surface-area (counting only one side) and thickness of the B-rich domain of the bilayer, respectively. The parameters $\varphi_{\mathrm{B}}^{\mathrm{v}}$ and $\varphi_{\mathrm{B}}^{\mathrm{d}}$ depend on the interaction of the block copolymer molecules with the solvent molecules and are independent, in theory, of S and R_{d} . Making the assumption that mass, radius and shape are conserved, i.e. no exchange of unimers with the surrounding solution and no rearrangement of the droplet morphology, $V_{\mathrm{B}}^{\mathrm{d}} \approx V_{\mathrm{B}}^{\mathrm{v}}$ and hence the following relationship can be considered:

$$\frac{4}{3}\pi R_{\mathrm{d}}^{3}\varphi_{\mathrm{B}}^{\mathrm{d}} \approx SL\varphi_{\mathrm{B}}^{\mathrm{v}}. \tag{3}$$

Rearranging (3) we can estimate the total internal surface of the self-assembled structure:

$$S \approx \frac{4\pi R_{\mathrm{d}}^{3}\varphi_{\mathrm{B}}^{\mathrm{d}}}{3L\varphi_{\mathrm{B}}^{\mathrm{v}}.} \tag{4}$$

The droplet will rearrange into a vesicle if $S \approx 4\pi R_{\mathrm{d}}^{2}$ (curvature effects can be neglected for $L \ll R_{\mathrm{d}}$), into a hemi-vesicle or porous vesicle if $S \ll 4\pi R_{\mathrm{d}}^{2}$ and into a particle with internal structure if $S \gg 4\pi R_{\mathrm{d}}^{2}$. This allows to define a shape parameter which determines what kind of structure is formed:

$$\Upsilon = \frac{R_{\mathrm{d}}\varphi_{\mathrm{B}}^{\mathrm{d}}}{3L\varphi_{\mathrm{B}}^{\mathrm{v}}}. \tag{5}$$

If $\Upsilon \approx 1$ a vesicle is formed, If $\Upsilon \ll 1$ a hemi or porous vesicle is formed and if $\Upsilon \gg 1$ a particle with internal structure is expected.

The estimation of four parameters ($R_\mathrm{d}, L, \varphi_\mathrm{B}^\mathrm{d}$ and $\varphi_\mathrm{B}^\mathrm{v}$), is beyond the scope of this report but will be discussed in a subsequent publication. It is also important to note that the experiments presented in Figure 6 were not performed with the objective of controlling the concentration of polymer in the nanoscale coacervate, however the mechanism presented here is our hypothesis for the observed results. Further work is underway to confirm this hypothesis by tracking the evolution of droplets into self-assembled structure, where the concentration of polymer in the droplet is varied and can be measured quantitatively.

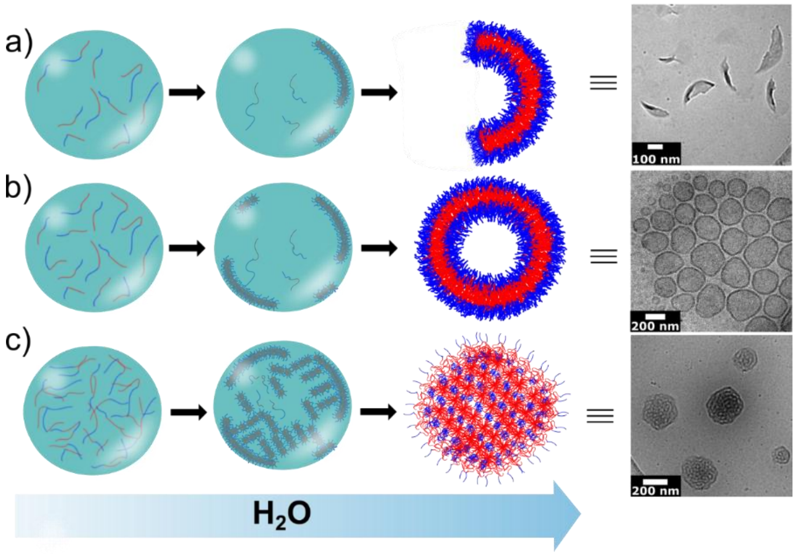

Figure 2.6: Proposed mechanism for the self-assembly of nano-scale block copolymer structures from a coacervate precursor droplet. The mechanism shows the relationship between the concentration of polymer in the droplet and the final self-assembled structure. a) Droplets with $\Upsilon \ll 1$ that arrange the polymer chains at the liquid-liquid interface to yield the hemi vesicles as shown in the respective Cryo-TEM image. b) Droplets with $\Upsilon \approx 1$ that arrange the polymer chains at the liquid-liquid interface to yield vesicles as shown in the respective Cryo-TEM image. c) Droplets with $\Upsilon \gg 1$ that arrange the polymer chains at the liquid-liquid interface to yield the bicontinuous spheres as shown in the respective Cryo-TEM image.

2.2 2.2 CONCLUSION

In conclusion we report, to the best of our knowledge, the first example of thermodynamically stable coacervates formed using non-ionic block copolymers by tuning the solvent composition during a solvent switch process. This work supports our previous observations that coacervation can occur during the self-assembly of amphiphilic polymers.[41] Here we have shown that three different diblock copolymers can form stable coacervates. We derived new equations to predict the phase behavior of block copolymers based on molecular structure and solvent composition that can be used as a guide for experimental work. This guide is important as the coacervation may only occur in a narrow region of the phase space. Although our model system undergoes coacervation in mixtures of organic solvent and water, it should be possible to design non-ionic block copolymers that undergo coacervation in pure aqueous solutions. Using PEO-*b*-PMMA block copolymers as a model system, we have shown quantitative agreement between our theoretical and experimental phase diagrams. We have also shown that the polymer coacervates can be used to direct the formation of solid phase materials with dimensions that span over six orders of magnitude. Our data indicates that the concentration of polymer in the coacervate phase plays a role in determining the morphology of self-assembled structures formed through a coacervate intermediate and we developed a theoretical model understanding and predicting morphology *a priori*. We anticipate new applications of neutral block copolymers will arise from this work and that non-ionic block copolymer coacervates will be applied at the interface between the biological and materials sciences. This work highlights the importance of considering coacervation as an intermediate phase during the solvent switch self-assembly of block copolymers. Lastly, we have demonstrated that if coacervation is a thermodynamically stable precursor, it must be overcome kinetically to achieve the formation of nanoscale or microscale polymer particles.

2.4 References

(1) Marciel, A. B.; Srivastava, S.; Tirrell, M. V. Structure and Rheology of Polyelectrolyte Complex Coacervates. *Soft Matter* **2018**, *14* (13), 2454–2464. https://doi.org/10.1039/C7SM02041D.

(2) Burgess, D. J. Practical Analysis of Complex Coacervate Systems. *Journal of Colloid and Interface Science* **1990**, *140* (1), 227–238. https://doi.org/10.1016/0021-9797(90)90338-O.

(3) Menger, F. M.; Sykes, B. M. Anatomy of a Coacervate. *Langmuir* **1998**, *14* (15), 4131–4137. https://doi.org/10.1021/la980208m.

(4) C. Obermeyer, A.; E. Mills, C.; Dong, X.-H.; J. Flores, R.; D. Olsen, B. Complex Coacervation of Supercharged Proteins with Polyelectrolytes. *Soft Matter* **2016**, *12* (15), 3570–3581. https://doi.org/10.1039/C6SM00002A.

(5) M. Johnston, B.; W. Johnston, C.; A. Letteri, R.; K. Lytle, T.; E. Sing, C.; Emrick, T.; L. Perry, S. The Effect of Comb Architecture on Complex Coacervation. *Organic & Biomolecular Chemistry* **2017**, *15* (36), 7630–7642. https://doi.org/10.1039/C7OB01314K.

(6) Huang, G.-Q.; Sun, Y.-T.; Xiao, J.-X.; Yang, J. Complex Coacervation of Soybean Protein Isolate and Chitosan. *Food Chemistry* **2012**, *135* (2), 534–539. https://doi.org/10.1016/j.foodchem.2012.04.140.

(7) Priftis, D.; Tirrell, M. Phase Behaviour and Complex Coacervation of Aqueous Polypeptide Solutions. *Soft Matter* **2012**, *8* (36), 9396–9405. https://doi.org/10.1039/C2SM25604E.

(8) Weinbreck, F.; de Vries, R.; Schrooyen, P.; de Kruif, C. G. Complex Coacervation of Whey Proteins and Gum Arabic. *Biomacromolecules* **2003**, *4* (2), 293–303. https://doi.org/10.1021/bm025667n.

(9) Everett, D. H. Manual of Symbols and Terminology for Physicochemical Quantities and Units, Appendix II: Definitions, Terminology and Symbols in Colloid and Surface Chemistry. *Pure and Applied Chemistry* **1972**, *31* (4), 577–638. https://doi.org/10.1351/pac197231040577.

(10) Wang, Q.; Schlenoff, J. B. The Polyelectrolyte Complex/Coacervate Continuum. *Macromolecules* **2014**, *47* (9), 3108–3116. https://doi.org/10.1021/ma500500q.

(11) Nishi, T.; Wang, T. T.; Kwei, T. K. Thermally Induced Phase Separation Behavior of Compatible Polymer Mixtures. *Macromolecules* **1975**, *8* (2), 227–234. https://doi.org/10.1021/ma60044a025.

(12) DE Jong, H. G. B.; Kruyt, H. R. Coacewation (Partial Miscibility in Colloid Systems). (Preliminary Communication). *Proc. Koninkl. Med. Akad. Wetersjap.* **1929**, *32*, 849–856.

(13) Urry, D. W.; Starcher, B.; Partridge, S. M. Coacervation of Solubilized Elastin Effects a Notable Conformational Change. *Nature* **1969**, *222* (5195), 795–796. https://doi.org/10.1038/222795a0.

(14) Martin, N. Dynamic Synthetic Cells Based on Liquid–Liquid Phase Separation. *ChemBioChem* **2019**, *20* (20), 2553–2568. https://doi.org/10.1002/cbic.201900183.

(15) Brangwynne, C. P.; Eckmann, C. R.; Courson, D. S.; Rybarska, A.; Hoege, C.; Gharakhani, J.; Jülicher, F.; Hyman, A. A. Germline P Granules Are Liquid Droplets That Localize by Controlled Dissolution/Condensation. *Science* **2009**, *324* (5935), 1729–1732. https://doi.org/10.1126/science.1172046.

(16) Hyman, A. A.; Weber, C. A.; Jülicher, F. Liquid-Liquid Phase Separation in Biology. *Annual Review of Cell and Developmental Biology* **2014**, *30* (1), 39–58. https://doi.org/10.1146/annurev-cellbio-100913-013325.

(17) Babinchak, W. M.; Surewicz, W. K. Liquid–Liquid Phase Separation and Its Mechanistic Role in Pathological Protein Aggregation. *Journal of Molecular Biology* **2020**, *432* (7), 1910–1925. https://doi.org/10.1016/j.jmb.2020.03.004.

(18) Patel, S. G.; Patel, M. D.; Patel, A. J.; Chougule, M. B.; Choudhury, H. Solid Lipid Nanoparticles for Targeted Brain Drug Delivery. In *Nanotechnology-Based Targeted Drug Delivery Systems for Brain Tumors*; Elsevier, 2018; pp 191–244. https://doi.org/10.1016/B978-0-12-812218-1.00008-7.

(19) Mason, A. F.; Buddingh', B. C.; Williams, D. S.; van Hest, J. C. M. Hierarchical Self-Assembly of a Copolymer-Stabilized Coacervate Protocell. *J. Am. Chem. Soc.* **2017**, *139* (48), 17309–17312. https://doi.org/10.1021/jacs.7b10846.

(20) Dogra, P.; Joshi, A.; Majumdar, A.; Mukhopadhyay, S. Intermolecular Charge-Transfer Modulates Liquid–Liquid Phase Separation and Liquid-to-Solid Maturation of an Intrinsically Disordered PH-Responsive Domain. *J. Am. Chem. Soc.* **2019**, *141* (51), 20380–20389. https://doi.org/10.1021/jacs.9b10892.

(21) Gomes, E.; Shorter, J. The Molecular Language of Membraneless Organelles. *J. Biol. Chem.* **2019**, *294* (18), 7115–7127. https://doi.org/10.1074/jbc.TM118.001192.

(22) Schmidt, H. B.; Görlich, D. Transport Selectivity of Nuclear Pores, Phase Separation, and Membraneless Organelles. *Trends in Biochemical Sciences* **2016**, *41* (1), 46–61. https://doi.org/10.1016/j.tibs.2015.11.001.

(23) Nott, T. J.; Craggs, T. D.; Baldwin, A. J. Membraneless Organelles Can Melt Nucleic Acid Duplexes and Act as Biomolecular Filters. *Nature Chem* **2016**, *8* (6), 569–575. https://doi.org/10.1038/nchem.2519.

(24) Ambadipudi, S.; Biernat, J.; Riedel, D.; Mandelkow, E.; Zweckstetter, M. Liquid–Liquid Phase Separation of the Microtubule-Binding Repeats of the Alzheimer-Related Protein Tau. *Nat Commun* **2017**, *8* (1), 1–13. https://doi.org/10.1038/s41467-017-00480-0.

(25) Lin, Y.; Protter, D. S. W.; Rosen, M. K.; Parker, R. Formation and Maturation of Phase-Separated Liquid Droplets by RNA-Binding Proteins. *Molecular Cell* **2015**, *60* (2), 208–219. https://doi.org/10.1016/j.molcel.2015.08.018.

(26) Bierma, J. C.; Roskamp, K. W.; Ledray, A. P.; Kiss, A. J.; Cheng, C.-H. C.; Martin, R. W. Controlling Liquid–Liquid Phase Separation of Cold-Adapted Crystallin Proteins from the Antarctic Toothfish. *Journal of Molecular Biology* **2018**, *430* (24), 5151–5168. https://doi.org/10.1016/j.jmb.2018.10.023.

(27) Wegmann, S.; Eftekharzadeh, B.; Tepper, K.; Zoltowska, K. M.; Bennett, R. E.; Dujardin, S.; Laskowski, P. R.; MacKenzie, D.; Kamath, T.; Commins, C.; Vanderburg, C.; Roe, A. D.; Fan, Z.; Molliex, A. M.; Hernandez-Vega, A.; Muller, D.; Hyman, A. A.; Mandelkow, E.; Taylor, J. P.; Hyman, B. T. Tau Protein Liquid–Liquid Phase Separation Can Initiate Tau Aggregation. *The EMBO Journal* **2018**, *37* (7), e98049. https://doi.org/10.15252/embj.201798049.

(28) Mohammadi, P.; Aranko, A. S.; Lemetti, L.; Cenev, Z.; Zhou, Q.; Virtanen, S.; Landowski, C. P.; Penttilä, M.; Fischer, W. J.; Wagermaier, W.; Linder, M. B. Phase Transitions as Intermediate Steps in the Formation of Molecularly Engineered Protein Fibers. *Commun Biol* **2018**, *1* (1), 1–12. https://doi.org/10.1038/s42003-018-0090-y.

(29) Quellet, C.; Schudel, M.; Ringgenberg, R. *Flavors & Fragrance Delivery Systems*. https://www.ingentaconnect.com/content/scs/chimia/2001/00000055/00000005/art00008 (accessed 2020-02-11).

(30) Voets, I. K.; de Keizer, A.; Cohen Stuart, M. A. Complex Coacervate Core Micelles. *Advances in Colloid and Interface Science* **2009**, *147–148*, 300–318. https://doi.org/10.1016/j.cis.2008.09.012.

(31) Phares, R. E.; Sperandio, G. J. Coating Pharmaceuticals by Coacervation. *Journal of Pharmaceutical Sciences* **1964**, *53* (5), 515–518. https://doi.org/10.1002/jps.2600530511.

(32) Yeo, Y.; Bellas, E.; Firestone, W.; Langer, R.; Kohane, D. S. Complex Coacervates for Thermally Sensitive Controlled Release of Flavor Compounds. *J. Agric. Food Chem.* **2005**, *53* (19), 7518–7525. https://doi.org/10.1021/jf0507947.

(33) Lloyd, D. R.; Kim, S. S.; Kinzer, K. E. Microporous Membrane Formation via Thermally-Induced Phase Separation. II. Liquid—Liquid Phase Separation. *Journal of Membrane Science* **1991**, *64* (1), 1–11. https://doi.org/10.1016/0376-7388(91)80073-F.

(34) Drobot, B.; Iglesias-Artola, J. M.; Vay, K. L.; Mayr, V.; Kar, M.; Kreysing, M.; Mutschler, H.; Tang, T.-Y. D. Compartmentalised RNA Catalysis in Membrane-Free Coacervate Protocells. *Nat Commun* **2018**, *9* (1), 1–9. https://doi.org/10.1038/s41467-018-06072-w.

(35) Mason, A. F.; Yewdall, N. A.; Welzen, P. L. W.; Shao, J.; van Stevendaal, M.; van Hest, J. C. M.; Williams, D. S.; Abdelmohsen, L. K. E. A. Mimicking Cellular Compartmentalization in a Hierarchical Protocell through Spontaneous Spatial Organization. *ACS Cent. Sci.* **2019**, *5* (8), 1360–1365. https://doi.org/10.1021/acscentsci.9b00345.

(36) Lou, J.; Friedowitz, S.; Qin, J.; Xia, Y. Tunable Coacervation of Well-Defined Homologous Polyanions and Polycations by Local Polarity. *ACS Cent. Sci.* **2019**, *5* (3), 549–557. https://doi.org/10.1021/acscentsci.8b00964.

(37) Priftis, D.; Leon, L.; Song, Z.; Perry, S. L.; Margossian, K. O.; Tropnikova, A.; Cheng, J.; Tirrell, M. Self-Assembly of α-Helical Polypeptides Driven by Complex Coacervation. *Angewandte Chemie International Edition* **2015**, *54* (38), 11128–11132. https://doi.org/10.1002/anie.201504861.

(38) Tang, T.-Y. D.; Hak, C. R. C.; Thompson, A. J.; Kuimova, M. K.; Williams, D. S.; Perriman, A. W.; Mann, S. Fatty Acid Membrane Assembly on Coacervate Microdroplets as a Step towards a Hybrid Protocell Model. *Nature Chem* **2014**, *6* (6), 527–533. https://doi.org/10.1038/nchem.1921.

(39) Ong, G. M. C.; Sing, C. E. Mapping the Phase Behavior of Coacervate-Driven Self-Assembly in Diblock Copolyelectrolytes. *Soft Matter* **2019**, *15* (25), 5116–5127. https://doi.org/10.1039/C9SM00741E.

(40) Mai, Y.; Eisenberg, A. Self-Assembly of Block Copolymers. *Chem. Soc. Rev.* **2012**, *41* (18), 5969–5985. https://doi.org/10.1039/C2CS35115C.

(41) Ianiro, A.; Wu, H.; Rijt, M. M. J. van; Vena, M. P.; Keizer, A. D. A.; Esteves, A. C. C.; Tuinier, R.; Friedrich, H.; Sommerdijk, N. A. J. M.; Patterson, J. P. Liquid–Liquid Phase Separation during Amphiphilic Self-Assembly. *Nat. Chem.* **2019**, *11* (4), 320–328. https://doi.org/10.1038/s41557-019-0210-4.

(42) Choucair, A.; Eisenberg, A. Control of Amphiphilic Block Copolymer Morphologies Using Solution Conditions. *Eur. Phys. J. E* **2003**, *10* (1), 37–44. https://doi.org/10.1140/epje/e2003-00002-5.

(43) Lodge, T. P.; Pudil, B.; Hanley, K. J. The Full Phase Behavior for Block Copolymers in Solvents of Varying Selectivity. *Macromolecules* **2002**, *35* (12), 4707–4717. https://doi.org/10.1021/ma0200975.

(44) Kelley, E. G.; Albert, J. N. L.; Sullivan, M. O.; Thomas H. Epps, I. I. I. Stimuli-Responsive Copolymer Solution and Surface Assemblies for Biomedical Applications. *Chem. Soc. Rev.* **2013**, *42* (17), 7057–7071. https://doi.org/10.1039/C3CS35512H.

(45) Zhang, Q.; Lin, J.; Wang, L.; Xu, Z. Theoretical Modeling and Simulations of Self-Assembly of Copolymers in Solution. *Progress in Polymer Science* **2017**, *75*, 1–30. https://doi.org/10.1016/j.progpolymsci.2017.04.003.

(46) Kositza, M. J.; Bohne, C.; Alexandridis, P.; Hatton, T. A.; Holzwarth, J. F. Dynamics of Micro- and Macrophase Separation of Amphiphilic Block-Copolymers in Aqueous Solution. *Macromolecules* **1999**, *32* (17), 5539–5551. https://doi.org/10.1021/ma9904316.

(47) Huang, C.-I.; Hsueh, H.-Y. Phase Behavior and Microstructural Length Scales of a Diblock Copolymer in the Presence of a Selective Solvent. *Polymer* **2006**, *47* (19), 6843–6856. https://doi.org/10.1016/j.polymer.2006.07.028.

(48) Perrier, S.; Takolpuckdee, P.; Westwood, J.; Lewis, D. M. Versatile Chain Transfer Agents for Reversible Addition Fragmentation Chain Transfer (RAFT) Polymerization to Synthesize Functional Polymeric Architectures. *Macromolecules* **2004**, *37* (8), 2709–2717. https://doi.org/10.1021/ma035468b.

(49) Leibler, L. Theory of Microphase Separation in Block Copolymers. *Macromolecules* **1980**, *13* (6), 1602–1617. https://doi.org/10.1021/ma60078a047.

(50) Sato, T.; Takahashi, R. Competition between the Micellization and the Liquid–Liquid Phase Separation in Amphiphilic Block Copolymer Solutions. *Polymer Journal* **2017**, *49* (2), 273–277. https://doi.org/10.1038/pj.2016.110.

(51) *Flory, F. 1953 Principles Of Polymer Chemistry*.

(52) Matsuyama, H.; Rajabzadeh, S.; Karkhanechi, H.; Jeon, S. 1.7 PVDF Hollow Fibers Membranes. In *Comprehensive Membrane Science and Engineering*; Elsevier, 2017; pp 137–189. https://doi.org/10.1016/B978-0-12-409547-2.12244-9.

(53) Smolders, C. A.; Reuvers, A. J.; Boom, R. M.; Wienk, I. M. Microstructures in Phase-Inversion Membranes. Part 1. Formation of Macrovoids. *Journal of Membrane Science* **1992**, *73* (2), 259–275. https://doi.org/10.1016/0376-7388(92)80134-6.

(54) Kamide, K.; Matsuda, S.; Saito, M. Evaluation of Concentration Dependence of χ-Parameter, Flory Temperature and Entropy Parameter for Polymer–Solvent System from Their Critical Solution Temperature and Concentration Data. *Polymer Journal* **1985**, *17* (9), 1013–1027. https://doi.org/10.1295/polymj.17.1013.

(55) Nicolai, T.; Colombani, O.; Chassenieux, C. Dynamic Polymeric Micelles versus Frozen Nanoparticles Formed by Block Copolymers. *Soft Matter* **2010**, *6* (14), 3111–3118. https://doi.org/10.1039/B925666K.

(56) Wright, D. B.; Patterson, J. P.; Gianneschi, N. C.; Chassenieux, C.; Colombani, O.; O'Reilly, R. K. Blending Block Copolymer Micelles in Solution; Obstacles of Blending. *Polym. Chem.* **2016**, *7* (8), 1577–1583. https://doi.org/10.1039/C5PY02006A.

(57) Parent, L. R.; Bakalis, E.; Ramírez-Hernández, A.; Kammeyer, J. K.; Park, C.; de Pablo, J.; Zerbetto, F.; Patterson, J. P.; Gianneschi, N. C. Directly Observing Micelle Fusion and Growth in Solution by Liquid-Cell Transmission Electron Microscopy. *J. Am. Chem. Soc.* **2017**, *139* (47), 17140–17151. https://doi.org/10.1021/jacs.7b09060.

(58) Cui, H.; Hodgdon, T. K.; Kaler, E. W.; Abezgauz, L.; Danino, D.; Lubovsky, M.; Talmon, Y.; Pochan, D. J. Elucidating the Assembled Structure of Amphiphiles in Solution via Cryogenic Transmission Electron Microscopy. *Soft Matter* **2007**, *3* (8), 945–955. https://doi.org/10.1039/B704194B.

(59) Friedrich, H.; Frederik, P. M.; de With, G.; Sommerdijk, N. A. J. M. Imaging of Self-Assembled Structures: Interpretation of TEM and Cryo-TEM Images. *Angewandte Chemie International Edition* **2010**, *49* (43), 7850–7858. https://doi.org/10.1002/anie.201001493.

(60) Lee, T. Y.; Choi, T. M.; Shim, T. S.; Frijns, R. A. M.; Kim, S.-H. Microfluidic Production of Multiple Emulsions and Functional Microcapsules. *Lab Chip* **2016**, *16* (18), 3415–3440. https://doi.org/10.1039/C6LC00809G.

(61) McKenzie, B. E.; Visser, J. F. de; Portale, G.; Hermida-Merino, D.; Friedrich, H.; Bomans, P. H. H.; Bras, W.; Monaghan, O. R.; Holder, S. J.; Sommerdijk, N. a. J. M. The Evolution of Bicontinuous Polymeric Nanospheres in Aqueous Solution. *Soft Matter* **2016**, *12* (18), 4113–4122. https://doi.org/10.1039/C6SM00053C.

(62) McKenzie, B. E.; Nudelman, F.; Bomans, P. H. H.; Holder, S. J.; Sommerdijk, N. A. J. M. Temperature-Responsive Nanospheres with Bicontinuous Internal Structures from a Semicrystalline Amphiphilic Block Copolymer. *J. Am. Chem. Soc.* **2010**, *132* (30), 10256–10259. https://doi.org/10.1021/ja102040u.

(63) McKenzie, B. E.; de Visser, J. F.; Friedrich, H.; Wirix, M. J. M.; Bomans, P. H. H.; de With, G.; Holder, S. J.; Sommerdijk, N. A. J. M. Bicontinuous Nanospheres from Simple

Amorphous Amphiphilic Diblock Copolymers. *Macromolecules* **2013**, *46* (24), 9845–9848. https://doi.org/10.1021/ma4019729.
(64) Meng, X.; Perry, S. L.; Schiffman, J. D. Complex Coacervation: Chemically Stable Fibers Electrospun from Aqueous Polyelectrolyte Solutions. *ACS Macro Lett.* **2017**, *6* (5), 505–511. https://doi.org/10.1021/acsmacrolett.7b00173.
(65) Wong, C. K.; Heidelmann, M.; Dulle, M.; Qiang, X.; Förster, S.; Stenzel, M. H.; Gröschel, A. H. Vesicular Polymer Hexosomes Exhibit Topological Defects. *J. Am. Chem. Soc.* **2020**. https://doi.org/10.1021/jacs.0c02009.
(66) G. Denkova, A.; H. Bomans, P. H.; Coppens, M.-O.; M. Sommerdijk, N. a. J.; Mendes, E. Complex Morphologies of Self-Assembled Block Copolymer Micelles in Binary Solvent Mixtures: The Role of Solvent – Solvent Correlations. *Soft Matter* **2011**, *7* (14), 6622–6628. https://doi.org/10.1039/C1SM05461A.
(67) He, X.; Song, M.; Liang, H.; Pan, C. Self-Assembly of the Symmetric Diblock Copolymer in a Confined State: Monte Carlo Simulation. *J. Chem. Phys.* **2001**, *114* (23), 10510–10513. https://doi.org/10.1063/1.1372189.
(68) Chen, P.; Liang, H.; Shi, A.-C. Microstructures of a Cylinder-Forming Diblock Copolymer under Spherical Confinement. *Macromolecules* **2008**, *41* (22), 8938–8943. https://doi.org/10.1021/ma800443h.

.

Appendix A: Supplementary Information for Chapter 2

A.1 Materials and instruments:

All reagents were purchased from Acros Organics, Fisher Scientific, or Sigma-Aldrich, and used without further purification unless otherwise noted. ^{1}H NMR spectra were collected on a 500 MHz Bruker Avance spectrometer. All samples were taken in $CDCl_3$. Chemical shifts are provided in ppm, calibrated from the residual $CDCl_3$ peak (7.26 ppm). All TEM experiments were performed on a JEOL 2100 equipped with a 200 keV field emission gun and a OneView camera, Irvine Materials Research Institute, University of California, Irvine. CryoTEM Quantifoil Holey Carbon Films were purchased from Electron Microscopy Sciences, grids were glow discharged for 70 s to increase hydrophilicity prior to sample preparation. Liquid Phase imaging was performed with a DENS solutions Ocean holder using 0 nm spacer chips. SEM imaging was performed on a FEI Magellan 400 XHR SEM. Optical and fluorescence imaging were performed using a Keyence Bz-X810 all in one fluorescence microscope. Size exclusion chromatography (SEC) was performed in DMF using an Agilent 1100 chromatograph equipped with RID detector and a PL gel 5 µm 300x7.5 mm mixed column. All samples were calibrated against polystyrene standards (MW= 580, 1300, 5000, 10000, 30000, 70000, 130000 g/mol).

A.2 Experiential Methods

A.2i) **Synthesis:**

Synthesis of CTA 1

To a 250 mL round bottom flask, dodecanethiol (10.1 g, 50 mmol), KOH (3.41, 60 mmol) were added and dissolved in EtOH (40 mL). After 30 min of stirring, CS_2 (3.0 mL, 39 mmol) was added via a syringe. After 4 h of stirring, Tosyl-Cl (4.65 g, 24.4 mmol) in DCM (10 mL) was added dropwise turning the reaction mixture orange. The reaction was stirred overnight. The reaction mixture was washed with brine and the organics were concentrated *in vacuo*. The solid intermediate was further dissolved in EtOAc (40 mL) and 4,4′-azobis(4-cyanovaleric acid) (5.55 g, 0.0198 mol) was added to the reaction mixture. The solution was heated at 80 °C for 12 hours. The solvent was evaporated, and the yellow product was purified using silica gel chromatography 20% ethyl acetate in hexanes. The pure product (3.7g, 20% yield) was dried in high-vac overnight to remove residual solvent. ^{1}H NMR ($CDCl_3$,500 MHz) δ ppm: 0.95 (t, *J* = 6.9 Hz, 3H), 1.32 (m, 18H), 1.76 (m, 1H), 1.95 (s, 3H), 2.46 (m, 2H), 2.75 (t, 2H), 3.39 (t, 2H).

Synthesis of Macro PEO-CTA

To a flame dried 100 mL two-neck round bottom flask under N_2 m-PEG_{45} (1.1 g, 0.5 mmol) was added along with DCC (212 mg, 1 mmol), anhydrous DCM was syringed in to dissolve the solids followed by the addition of **CTA-1** (417 mg, 1 mmol) dissolved in DCM (5 mL). The reaction was covered with foil under N_2 and stopped after 48 h. The dicyclohexyl urea precipitate was filtered out and the organics were evaporated in vacuo, the yellow solids were dissolved in minimal THF and the viscous solution was poured into cold Et_2O while vigorously stirring to precipitate the **PEO-CTA**. The precipitate also contains unfunctionalized m-PEG$_{45}$ as the DCC coupling reaction was not quantitative, the macro CTA was used with the unfunctionalized m-PEG. The concentration of the functionalized PEG was determined using UV-vis analysis (Figure S6). ^{1}H NMR ($CDCl_3$,500 MHz) δ ppm: 0.88 (t, *J* = 6.9 Hz, 3H), 1.25 (m, 18H), 1.70 (m, 1H), 1.87 (s, 3H), 2.46 (m, 2H), 2.66 (, 2H), 3.32 (m, 2H), 3.38 (s, 3H), 3.64 (s, 180H).

Synthesis of PEO$_{45}$-b-PMMA$_{200}$

To a 10 mL Schleck tube MMA (0.62 g, 6.2 mmol), AIBN (0.5 mg, 0.62 mmol), **PEO-CTA** (70 mg, 0.0292 mmol) and toluene (300 μL) were added along with a stir bar. The mixture was vigorously stirred and sparged with N_2 for 20 min. The tube was sealed and heated to 70 °C in an oil bath. The polymerization was monitored via the consumption of MMA using ^{1}H NMR. After 12 hours the polymerization was "gelled", indicating high conversion, in this case 90% conversion. The polymer was precipitated three times into cold methanol and dried in a vacuum oven at 40 ^{o}C. ^{1}H NMR ($CDCl_3$, 500 MHz) δ ppm: 0.86-1.02 (CH_2 polymer back bone), 1.81 (CH_3, PMMA), 3.38 (CH_3O- PEO End Group), 3.60 (-OCH_3, PMMA), 3.64 (-OCH_2CH_2-). All PEO$_{45}$-PMMA block copolymers were synthesized using this procedure, varying the monomer ratios for desired DP)

Synthesis of PDMA$_{70}$

To a 10 mL Schleck tube DDMAT (0.100 g, 0.274 mmol), AIBN (0.45 mg, 0.0274 mmol), DMA (1.9 g, 21.9 mmol) and toluene (300 μL) were added along with a stir bar. The mixture was vigorously stirred and sparged with N_2 for 20 min. The tube was sealed and heated to 70 °C in an oil bath. The polymerization was monitored via the consumption of DMA using ^{1}H NMR. After 6 hours the polymerization was "gelled", indicating high conversion, in this case 85% conversion. The polymer was precipitated three times into cold ether and dried in a vacuum oven at 40 ^oC. ^1H NMR ($CDCl_3$, 500 MHz) δ ppm: 0.88 (t, *J* = 6.9 Hz, 3H), (1.0-1.9) (CH_2, CH polymer back bone), 2.2- 3.2 ($(CH_3)_2N$).

Synthesis of $PDMA_{70}$-*b*-$PMMA_{450}$

To a 10 mL Schleck tube $PDMA_{70}$ (0.200 g, 0.030mmol), AIBN (0.1mg), MMA (1.35 g, 13.5 mmol) and toluene (300 μL) were added along with a stir bar. The mixture was vigorously stirred and sparged with N_2 for 20 min. The tube was sealed and heated to 70 °C in an oil bath. The polymerization was monitored via the consumption of MMA using ^1H NMR. After 4 hours the polymerization was "gelled", indicating high conversion, in this case 99% conversion. The polymer was precipitated three times into cold ether and dried in a vacuum oven at 40 ^oC. ^1H NMR ($CDCl_3$, 500 MHz) δ ppm: 0.82-0.88 (DDMAT), 1.0-1.9 (CH_2, CH polymer back bone), 2.2- 3.2 ($(CH_3)_2N$), (CH_3, PMMA), 3.60 (-OCH_3, PMMA).

A.2 ii) **Preparation of organic-water mixtures for studying the phase behavior of amphiphilic block copolymers:**

The phase behavior of PEO_{45}-*b*-$PMMA_x$ was mapped experimentally. Self-assembly by the solvent switch method was carried out as a function of PMMA chain length (130, 200, 300, 400) and starting polymer concentration (1, 5, 10 mg mL^{-1}). For each sample, a calculated volume of polymer solution was used, and water was subsequently added to achieve the desired φW with 1 mL being the final solution volume. The phase behavior of each sample was determined largely based on a visual inspection of the vial supplemented by optical microscopy and cryoTEM as detailed in Figure 1. Each sample was categorized as following: clear solution (no self-assembly), milky opaque solution (coacervate formation/ LLPS), translucent blue turbid solution (nano particle formation). This procedure was used to perform solvent switch experiments with other block copolymers as well ($PDMA_{70}$-*b*-$PMMA_{450}$, PEO_{45}-*b*-PCL_6) Table S1-S3 presents the details and outcomes of each sample for this study.

A.2 iii) **Experiments to test the pathway dependence on the coacervation of PEO-b-PMMA block copolymers**:

Coacervates of PEO_{45}-$PMMA_{300}$ were formed from different pathways to test if the formation of these droplets was path dependent. As shown earlier, increasing the water content from no water to where phase separation occurs (φW ≈ 0.25) results in the formation of coacervates. However, in (Figure S2 a) we show that if nanoparticles are first formed at higher water content, in this case φW = 0.35, and more dioxane is added to decrease the water content to where the solution is expected to phase separate(φW ≈ 0.25), we see coacervate formation again (Figure S2 b). This suggests the coacervates form under thermodynamic control. Furthermore, addition of solid polymer to a mixture of φW These experiments showcase the path independent behavior of coacervate formation which means this process is under thermodynamic control.

A.2 iv) **Preparation of block copolymer nanoparticles through a coacervate intermediate**

PEO_{45}-*b*-$PMMA_{300}$ nanoparticles were self-assembled by the solvent switch method. Water (500 µL) was added using a micro-pipette within 1 second to the polymer solutions (500 µL) of varying polymer concentrations (1, 5, 10 mg mL^{-1}). The samples were vortexed for 10 seconds. The self-assembled samples turned lightly turbid

.

indicating the formation of nano structures in solution. The dioxane:water solutions were dialyzed (3.5K molecular weight cutoff) extensively against DI water and analyzed by Cryo-TEM.

A.2 v) **Preparation of block copolymer microparticles through a coacervate intermediate**

PEO_{45}-*b*-$PMMA_{300}$ microparticles were self-assembled in two steps. First, water (250 µL) was added quickly within 1 second to the polymer solutions (750 µL, 5 mg mL^{-1}) to induce coacervation ($\varphi W = 0.25$). The coacervate solutions were vortexed for 10 seconds. Subsequently, more water (375 µL) was added to the coacervate solution to self-assemble the micron size coacervates into micro particles. The dioxane:water solutions were dialyzed (3.5K molecular weight cutoff) extensively against DI water and analyzed by SEM.

A.2 vi) **Preparation of block copolymer porous networks through a coacervate intermediate**

PEO_{45}-*b*-$PMMA_{300}$ porous pellets were self-assembled in two steps. First, water (250 µL) was added directly to the polymer solutions (750 µL, 5 mg mL^{-1}) to induce coacervation ($\varphi W = 0.25$). The coacervate solutions were vortexed for 10 seconds and then centrifuged at 10,000 g for 15 minutes to separate the coacervate phase and the dilute phase. The dilute phase was decanted from the Eppendorf tubes and excess water (≈ 1000 µL) was added on top of the coacervate phase to drive the self-assembly of mm size pellets. The solvent was discarded, and the pellet was dried using Kimwipes, the pellet was sliced using a scalpel and analyzed by SEM.

A.2 vii) **Preparation of block copolymer fibers through a coacervate intermediate**

PEO_{45}-*b*-$PMMA_{300}$ fibers were formed in two steps. First, water (250 uL) was added directly to the polymer solutions (750 µL, 5 mg mL^{-1}) to induce coacervation (φW = 0.25). The coacervate solutions were vortexed for 10 seconds and then centrifuged at 10,000 g for 15 minutes to separate the coacervate phase and the dilute phase. The coacervate phase (≈ 10-50 uL) was drawn from the samples and dropped onto a glass slide. Using a metal spatula, fibers were pulled from the coacervate solution on the glass slide (Supplementary Movie 3). The fibers were easily extended to lengths of 20-30 cm, depending on the volume of the coacervate solution. The fibers were dried under atmosphere and further analyzed by SEM.

A.2 viii) **Liquid Phase Electron Microscopy of block copolymer coacervates:**

The onset of coacervation of PEO_{45}-*b*-$PMMA_{300}$ was observed in real time by carrying out the solvent switch experiments inside the cell. All nano-chips used were plasma cleaned (1:1 Ar:O2) for 4 minutes prior to the assembly of the cell. PEO_{45}-*b*-$PMMA_{300}$ solution (5 mg mL^{-1} in dioxane) was drop casted (≈ 0.5 µL) on to the bottom chip and the cell was sealed by placing the top chip. The cell was tested for any leaks prior to inserting it in the microscope. Once in the microscope, using a 500 µL syringe water was flowed into the tip surrounding the cell and creating a diffusion gradient between the two solvents. TEM imaging was performed on a JEOL-2100F TEM using a Schottky type field emission gun operating at 200 kV with an electron dose rate $\approx 10\frac{e}{nm^2s}$and the total dose$\approx 4x10^4\frac{e}{nm^2}$. Images were recorded with an exposure of 1 second having a dead time of ≈3 seconds using the *TEM Recorder* script for DigitalMicrograph and collected using the Gatan Oneview. Image Stacks were manipulated in DigitalMicrograph and ImageJ. Each image was binned 4x in the x and y direction and the movie was created. Snapshots in Figure 3 are of this same processed data.

A.2 ix) **Cryo-electron microscopy of block copolymer assemblies**

CryoTEM Quantifoil Holey Carbon Films were purchased from Electron Microscopy Sciences, grids were glow discharged for 70 s to increase hydrophilicity prior to sample preparation. Vitrification was carried out by an Automatic Plunge Freezer ME GP2 (Leica Microsystems) where sample preparation onto cryoTEM grids was carried out at 95% humidity to prevent evaporation and blotted for (2, 3 or 4) s before autoplunging into liquid propane. Vitrified samples were studied on a JEOL-2100F TEM using a Schottky type field emission gun operating at 200 kV. Size measurements for cryoTEM images were performed using the measurement tool in ImageJ.

A.2 x) **Cryo-electron microscopy of block copolymer nano-coacervates**

3 uL of 5 mg mL^{-1} PEO_{45}-$PMMA_{300}$ solution in dioxane and 15 % water was deposited onto the TEM grid inside the Leica EM GP humidity chamber. The sample was blotted using a filter paper for 3 seconds and plunged into liquid propane to vitrify the sample. The polymer solution crosses the phase boundaries during the sample prep as the water concentration increases inside the humidity chamber as dioxane is a hygroscopic solvent. Figure S5 a-c show bicontinuous structure that were self-assembled during the sample prep. These structures are expected in the self-assembled region for this system as discussed in the main text. However, for these experiments our goal was to

trap the coacervates that form prior to the self-assembled structures. In other parts of the grid we observed distinct structures that have not been seen in samples that were prepared in a vial. Image d shows an overview of low contrast “field” that has a continuous structure throughout it. Image e and f capture the continuous fields at a higher magnification. We suspect the irregular shapes of such fields arise from the coalescence of the coacervate precursor that forms during the self-assembly and the flattening of these fields must be due to the thin layer of solution these structures are assembled in. Ice-layers for Cryo-TEM experiments are typically ~100-200 nm thickness, this forces the liquid precursors of sizes larger than this to either be removed during blotting or to flatten out..

A.2 xi) **Optical microscopy of block copolymer coacervates**

Standard microscope slides along with 1.0 mm coverslips were used to prepare samples for bright-field imaging using the Keyence optical microscope. Coacervate samples were vortexed for 10 s and then 20 µL of coacervate solution was sealed between the glass slide and the coverslips for imaging each sample. Images were collected with 10x and 20x objective lenses. The images were not further modified after collection.

A.2xii) **Scanning Electron Microscopy of Polymer microparticles and fibers**

Microparticle solutions in pure water were deposited (≈ 10 µL) on 1x1 cm glass substrate. The samples were sputter coated with 5nm of iridium (Quorum Q150T). Polymer fibers and porous membrane cross sections were stuck on conductive tape and sputter coated with 5nm of iridium (Quorum Q150T). All samples were imaged by a

FEI Magellan 400 XHR system. Secondary electron images were acquired with accelerating voltages of (5 or 10 keV), using a through lens detector operating in immersion mode. Size measurements for SEM images were performed using the measurement tool in ImageJ.

A.3 Supplementary Discussion

A.3 i) **Discussion on the relationship between block copolymer structure and pore diameter in self-assembled structures:**

The dimensions of block copolymer structures can be related to the total length of the polymer chains (or individual blocks) and the chain stretching factor for the block. Comparing the measured dimensions to the total extended length of a polymer (or individual block) can provide information to rule out or support a morphological assignment.[1] For a bicontinuous structure, the pore diameter should not be more than 2x the hydrophilic polymer chain length and the center to center distance between pores should not be more than 2x the total length of the block copolymer chain. Our model polymer, PEO_{45}-*b*-$PMMA_{300}$, has a fully extended PMMA block length of 300*0.25 nm = 87.5 nm and a fully extended PEO block length of 12.75 nm.

A.3 ii) **Flory-Huggins theory for block copolymers in a solvent mixture.**

The Flory-Huggins (F-H) energy of mixing ($\acute{G}_{mix}^{bcp}$) of a block copolymer in a mixture of solvents (S1 and S2) is derived below. The solvent mixtures is considered as a single solvent S, the composition of which is described by φ_{S1} and φ_{S2}, defined as:

$$\varphi_{S1} = \frac{n_{S1}}{n_S}, \varphi_{S2} = \frac{n_{S2}}{n_S} = 1 - \varphi_{S1}. (1)$$

Here, n_{S1} and n_{S2} are the number of molecules of S1 and S2, respectively, while $n_S = n_{S1} + n_{S2}$ is the total number of solvent molecules. The system is considered to contain n_S molecules of solvent and n_P molecules of AB; each solvent molecule is composed of $N_S = N_{S1} = N_{S2}$ segments while the blocks chain lengths are denoted as N_A and N_B, respectively. The average volume fractions of solvent, A and B segments in the system are than defined as:

$$\phi_S = \frac{n_S N_S}{n_P(N_A + N_B) + n_S N_S}, \phi_A = \frac{n_P N_A}{n_P(N_A + N_B) + n_S N_S}, \phi_B = \frac{n_P N_B}{n_P(N_A + N_B) + n_S N_S}. (2)$$

The total *average* copolymer segment volume fraction in the system ϕ_P is

$$\phi_P = \frac{n_P(N_A + N_B)}{n_P(N_A + N_B) + n_S N_S} (3)$$

Obviously, ϕ_A and ϕ_B are related to ϕ_P by

$$\phi_A = \phi_P \frac{N_A}{N_A + N_B}, \phi_B = \phi_P \frac{N_B}{N_A + N_B} (4)$$

It is assumed that the entropy of mixing block copolymers and the solvent mixture equals that of a homopolymer with total chain length $N = N_A + N_B$ in a solvent S. The block copolymer enthalpy of mixing is modelled as that of a three-component system, where two distinct polymers are mixed in a solvent. Hence, the Gibbs energy of mixing for block copolymers can obtained combining the Flory-Huggins mixing entropy of a two-component system with the mixing enthalpy of a three-component system[2]:

$$\acute{G}_{mix}^{bcp} = \frac{\Delta G_{mix}^{bcp}}{k_B T} = n_S \ln(\phi_S) + n_P \ln(\phi_P) + N_S n_S \phi_A \chi_{AS} + N_S n_S \phi_B \chi_{BS} + N_A n_P \phi_B \chi_{AB}. (5)$$

The termsχ_{AS}, χ_{BS} and χ_{AB} are the F-H interaction parameters, which depend upon the solvent composition:

$$\chi_{AS} = \varphi_{S1}\chi_{AS1} + (1-\varphi_{S1})\chi_{AS2}, \chi_{BS} = \varphi_{S1}\chi_{BS1} + (1-\varphi_{S1})\chi_{BS2}. (6)$$

The parameters χ_{AS1}, χ_{AS2}, χ_{BS1} and χ_{BS2} are the Flory-Huggins interaction parameters[3] describing the interaction of the A and B blocks with S1 and S2 respectively. The term $\chi_{AB}$is the interaction parameter between the blocks.

The derivatives of $\acute{G}_{mix}^{bcp}$ with respect to n_P and n_S are the copolymer and solvent chemical potentials respectively, which using (4), can be written as

$$\frac{\mu_{bcp} - \mu_{bcp}^{0}}{k_B T} = \acute{\mu}_{bcp} = (\frac{\partial \acute{G}_{mix}^{bcp}}{\partial n_P})_{T,P,n_S} =$$

$$\ln(\phi_P) + (1 - \frac{N_A + N_B}{N_S})(1-\phi_P) + (N_A\chi_{AS} + N_B\chi_{BS})(1-\phi_P)^2 + \frac{\chi_{AB}N_A N_B \phi_P}{N_A + N_B}(2-\phi_P), (7)$$

$$\frac{\mu_S - \mu_S^{0}}{k_B T} = \acute{\mu}_S = (\frac{\partial \acute{G}_{mix}^{bcp}}{\partial n_S})_{T,P,n_P} =$$

$$\ln(1-\phi_P) + (1 - \frac{N_S}{N_A + N_B})\phi_P + \frac{N_S}{N_A + N_B}(N_A\chi_{AS} + N_B\chi_{BS} - \frac{\chi_{AB}N_A N_B}{N_A + N_B}){\phi_P}^2. (8)$$

It is easy to show that for $N_P = N_A + N_B$, $\chi_{AB} = 0$and $\chi_{AS} = \chi_{BS}$, the F-H chemical potentials for the homopolymer-solvent case are recovered[ ].

Imposing$\partial\, \acute{\mu}_S / \partial\, \phi_P = 0$ (or $\partial\, \acute{\mu}_{bcp} / \partial\, \phi_P = 0$ yields the critical conditions for phase separation. The critical polymer volume fraction ϕ_P^{crit} follows as

$$\phi_P^{crit} = \frac{\sqrt{N_A N_S + N_B N_S} - N_S}{N_A + N_B - N_S}, (9)$$

and the critical demixing conditions are given by

$$N_A\chi_{AS} + N_B\chi_{BS} - \frac{\chi_{AB}N_AN_B}{N_A + N_B} = \frac{N_A + N_B}{2N_S(1-\phi_P^{crit})^2} \quad (10)$$

Insertion of these results into (5.6) yields the critical solvent mixture composition φ_{S1}^{crit}

$$\varphi_{S1}^{crit} = \frac{\left(\frac{N_A + N_B + N_S + 2\sqrt{(N_A + N_B)N_S}}{2N_S} + \frac{\chi_{AB}N_AN_B}{N_A + N_B} - N_A\chi_{AS2} - N_B\chi_{BS2}\right)}{N_A(\chi_{AS1} - \chi_{AS2}) + N_B(\chi_{BS1} - \chi_{BS2})} \quad (11)$$

A.3 iii) **Calculation of the solvent switch diagrams**

The solvent switch diagrams have been calculated comparing using equation (11) and comparing equation (5) with the free energy of micelle formation from Sato and Takahashi.[4] The values of the interaction parameters used in the calculations are reported in Table S3.

A.4 Supplementary information Tables and Figures:

Table A1: Outcomes of all solvent switch experiments of PEO$_{45}$-*b*-PMMA$_x$ block copolymers for the phase diagrams presented in the main text. Outcomes (NSA = no self-assembly, LLPS = liquid liquid phase separation, NP= Nanoparticle formation).

Polymer conc (mg mL^{-1})	PMMA (Dp)	Dioxane (uL)	Water (uL)	$\boldsymbol{\phi}_{\mathbf{W}}$	Outcome
1	130	900	100	0.1	NSA
1	130	750	250	0.25	NSA
1	130	725	275	0.275	NSA
1	130	700	300	0.3	NP
1	130	675	325	0.325	NP
1	130	650	350	0.35	NP
1	130	550	450	0.45	NP
1	130	500	500	0.5	NP
1	130	300	700	0.7	NP
1	200	900	100	0.1	NSA
1	200	750	250	0.25	NSA
1	200	725	275	0.275	NP
1	200	700	300	0.3	NP
1	200	675	325	0.325	NP
1	200	650	350	0.35	NP
1	200	550	450	0.45	NP
1	200	500	500	0.5	NP
1	200	300	700	0.7	NP

1	300	900	100	0.1	NSA
1	300	750	250	0.25	NSA
1	300	725	275	0.275	LLPS
1	300	700	300	0.3	NP
1	300	675	325	0.325	NP
1	300	650	350	0.35	NP
1	300	550	450	0.45	NP
1	300	500	500	0.5	NP
1	300	300	700	0.7	NP
1	400	900	100	0.1	NSA
1	400	800	200	0.2	NSA
1	400	775	225	0.225	NSA
1	400	750	250	0.25	LLPS
1	400	725	275	0.275	LLPS
1	400	700	300	0.3	LLPS
1	400	675	325	0.325	NP
1	400	650	350	0.35	NP
1	400	550	450	0.45	NP
1	400	500	500	0.5	Np
1	400	300	700	0.7	NP
5	130	900	100	0.1	NSA
5	130	750	250	0.25	NSA
5	130	725	275	0.275	NP
5	130	700	300	0.3	NP
5	130	675	325	0.325	NP
5	130	650	350	0.35	NP
5	130	550	450	0.45	NP
5	130	500	500	0.5	NP
5	130	300	700	0.7	NP
5	200	900	100	0.1	NSA
5	200	750	250	0.25	NSA
5	200	725	275	0.275	LLPS
5	200	700	300	0.3	NP
5	200	675	325	0.325	NP
5	200	650	350	0.35	NP
5	200	550	450	0.45	NP
5	200	500	500	0.5	NP
5	200	300	700	0.7	NP
5	300	900	100	0.1	NSA
5	300	800	200	0.2	NSA
5	300	775	225	0.25	NSA
5	300	750	250	0.25	LLPS
5	300	725	275	.275	LLPS
5	300	700	300	0.3	NP
5	300	675	325	0.325	NP
5	300	650	350	0.35	NP

5	300	550	450	0.45	NP
5	300	500	500	0.5	NP
5	300	300	700	0.7	NP
5	400	900	100	0.1	NSA
5	400	800	200	0.2	NSA
5	400	775	225	0.225	LLPS
5	400	750	250	0.25	LLPS
5	400	725	275	0.275	LLPS
5	400	700	300	0.3	NP
5	400	675	325	0.325	NP
5	400	650	350	0.35	NP
5	400	550	450	0.45	NP
5	400	500	500	0.5	Np
5	400	300	700	0.7	NP
10	130	900	100	0.1	NSA
10	130	750	250	0.25	NSA
10	130	725	275	0.275	NSA
10	130	700	300	0.3	NSA
10	130	675	325	0.325	LLPS
10	130	650	350	0.35	NP
10	130	550	450	0.45	NP
10	130	500	500	0.5	NP
10	130	300	700	0.7	NP
10	200	900	100	0.1	NSA
10	200	800	200	0.2	NSA
10	200	775	225	0.225	NSA
10	200	750	250	0.25	LLPS
10	200	725	275	0.275	LLPS
10	200	700	300	0.3	NP
10	200	675	325	0.325	NP
10	200	650	350	0.35	NP
10	200	550	450	0.45	NP
10	200	500	500	0.5	NP
10	200	300	700	0.7	NP
10	300	900	100	0.1	NSA
10	300	800	200	0.2	NSA
10	300	775	225	0.25	LLPS
10	300	750	250	0.25	LLPS
10	300	725	275	0.275	LLPS
10	300	700	300	0.3	NP
10	300	675	325	0.325	NP
10	300	650	350	0.35	NP
10	300	550	450	0.45	NP
10	300	500	500	0.5	NP
10	300	300	700	0.7	NP
10	400	900	100	0.1	NSA

10	400	800	200	0.2	NSA
10	400	775	225	0.225	LLPS
10	400	750	250	0.25	LLPS
10	400	725	275	0.275	LLPS
10	400	700	300	0.3	NP
10	400	675	325	0.325	NP
10	400	650	350	0.35	NP
10	400	550	450	0.45	NP
10	400	500	500	0 .5	Np
10	400	300	700	0.7	Np

Table A2: Outcomes of solvent switch experiments of PEO_{45}-*b*-$PMMA_{300}$ in THF and DMF. Outcomes (NSA= no self-assembly, NP = nanoparticle formation, PPT = precipitation)

Polymer conc (mg mL^{-1})	Solvent	Solvent (uL)	Water (uL)	$\boldsymbol{\phi}_{W}$	Outcome
5	THF	900	100	0.1	NSA
5	THF	700	300	0.3	NSA
5	THF	500	500	0.5	NP
5	THF	100	900	0.9	NP
5	DMF	900	100	0.1	NSA
5	DMF	700	300	0.3	PPT
5	DMF	500	500	0.5	PPT
5	DMF	100	900	0.9	PPT

Table A3: Outcomes of solvent switch experiments of $PDMA_{70}$-*b*-$PMMA_{450}$ in THF, dioxane, DMF, and acetone. Outcomes (NSA= no self-assembly, NP = nanoparticle formation, PPT = precipitation)

Polymer conc (mg mL^{-1})	Solvent	Solvent (uL)	Water (uL)	$\boldsymbol{\phi}_{W}$	Outcome
5	THF	900	100	0.1	NSA
5	THF	750	250	0.25	NSA
5	THF	500	500	0.5	NP
5	THF	100	900	0.7	NP
5	DMF	300	700	0.1	NSA
5	DMF	750	250	0.25	PPT
5	DMF	500	500	0.5	PPT
5	DMF	300	700	0.7	PPT
5	Acetone	900	100	0.1	NSA
5	Acetone	720	250	0.25	LLPS
5	Acetone	500	500	0.5	NP
5	Acetone	300	700	0.7	NP

Table A4: Interaction parameters used for phase boundaries calculations in Figure 2.

Interaction	χ**value**
χ_{AS1}PEO : water)	0.49
χ_{AS_2}PEO : dioxane)	0.20
χ_{BS1}PMMA : water)	2.8
χ_{BS_2}PMMA : dioxane)	0.1
χ_{AB}PMMA : PEO)	0.005

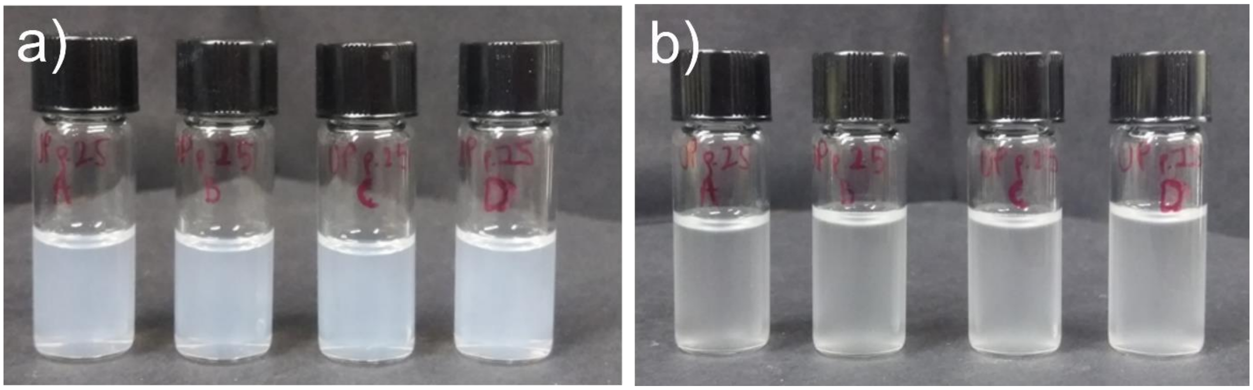

Figure A1: Pathway dependent experiments for the coacervation of PEO45-*b*-PMMA300. Nano particle solutions (φ_W = 0.50) of PEO45-*b*-PMMA300 were used to form coacervates by the addition of dioxane to reduce the water to φ_W = 0.25 (supplementary section 2-iii). a) Nanoparticle solutions (φ_W = 0.50) of PEO45-*b*-PMMA300. b) Coacervate solutions (φ_W = 0.50) of PEO45-*b*-PMMA300.

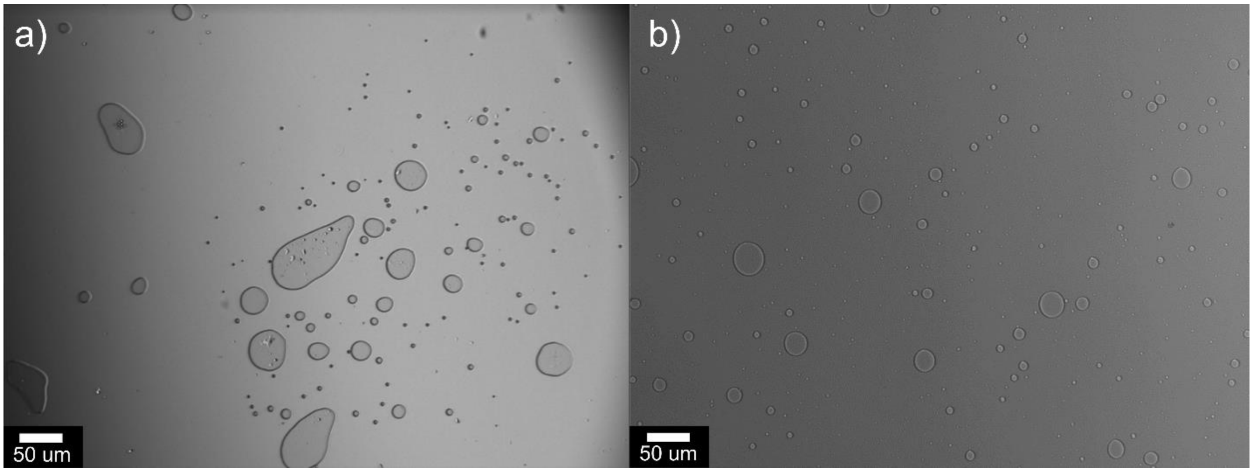

Figure A2: Bright field optical microscopy of block copolymer coacervates. a) PEO_{45}-*b*-PCL_6 coacervates in 34 % water in acetone mixture. b) $PDMA_{70}$-*b*-$PMMA_{450}$ coacervates in 25 % water in THF mixture.

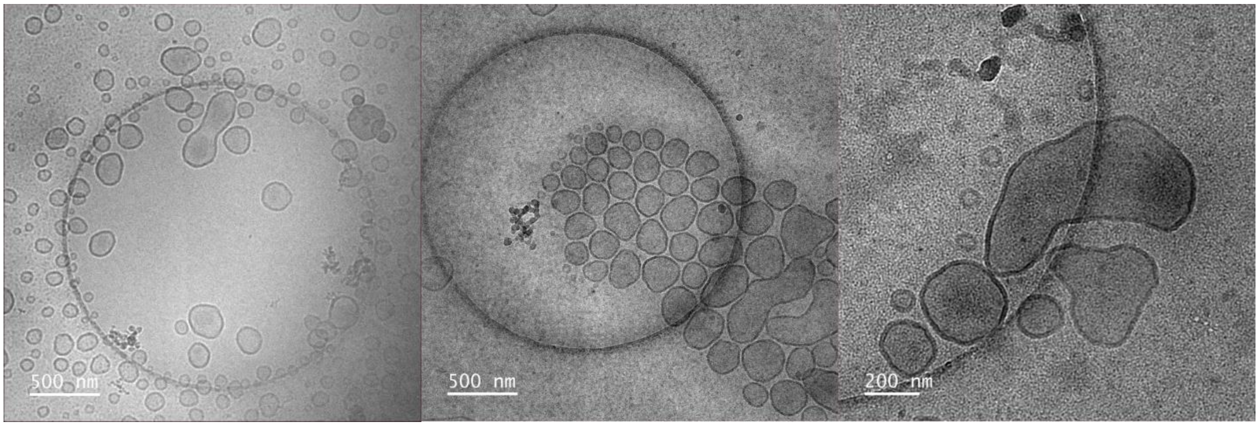

Figure A3: Cryo-TEM images of PEO_{45}-*b*-$PMMA_{300}$ vesicles with irregular anisotropic shapes.

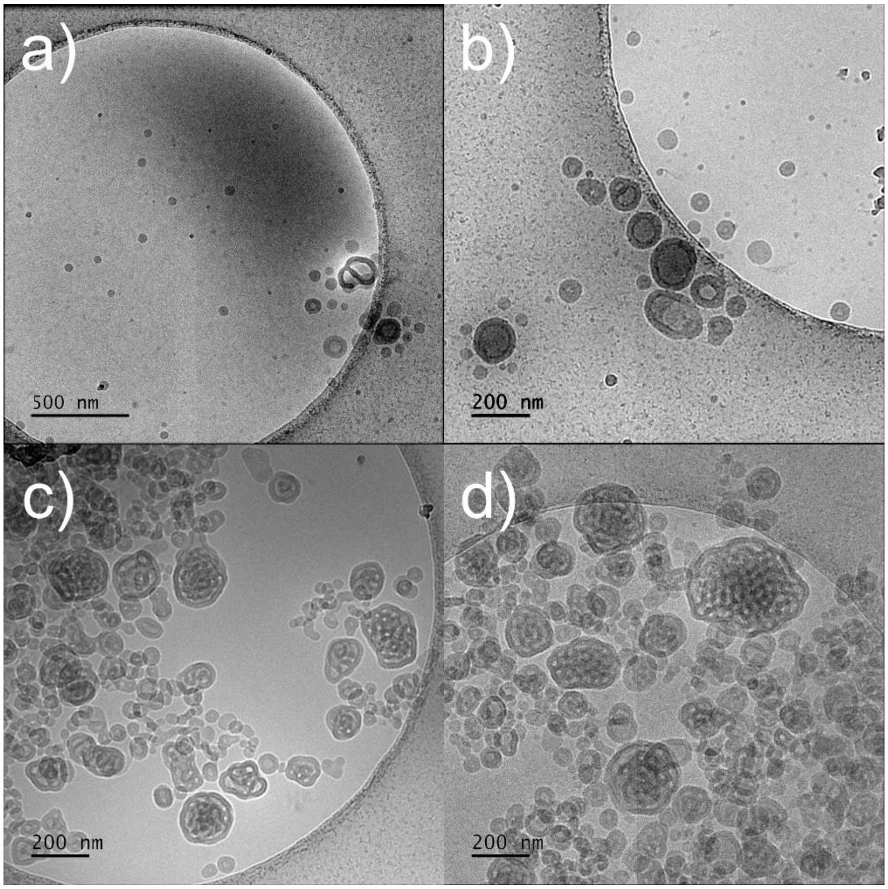

Figure A4: Cryo-TEM images of PEO_{45}-$PMMA_{300}$ assemblies after dialysis in water. a-b) Images of vesicles and spherical micelles in 1 mg mL^{-1} PEO_{45}-*b*-$PMMA_{300}$ solution self-assembled at 50% water in dioxane and further dialyzed against pure water. c-d) Images of bicontinuous spheres and vesicles 5 mg mL^{-1} PEO_{45}-*b*-$PMMA_{300}$ solution self-assembled at 50% water in dioxane and further dialyzed against pure water.

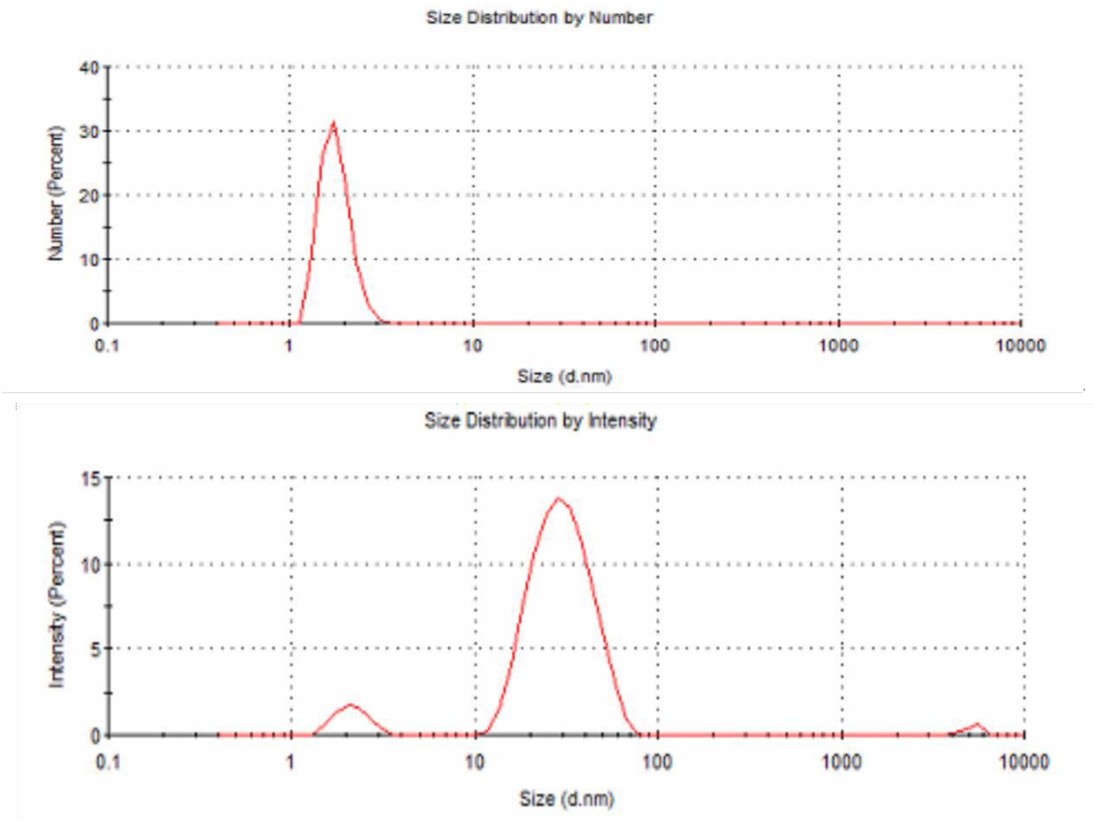

Figure S6: DLS size distribution by number and intensity of PEO45-*b*-PMMA300 homogenous sample $\varphi_W = 0.10$.

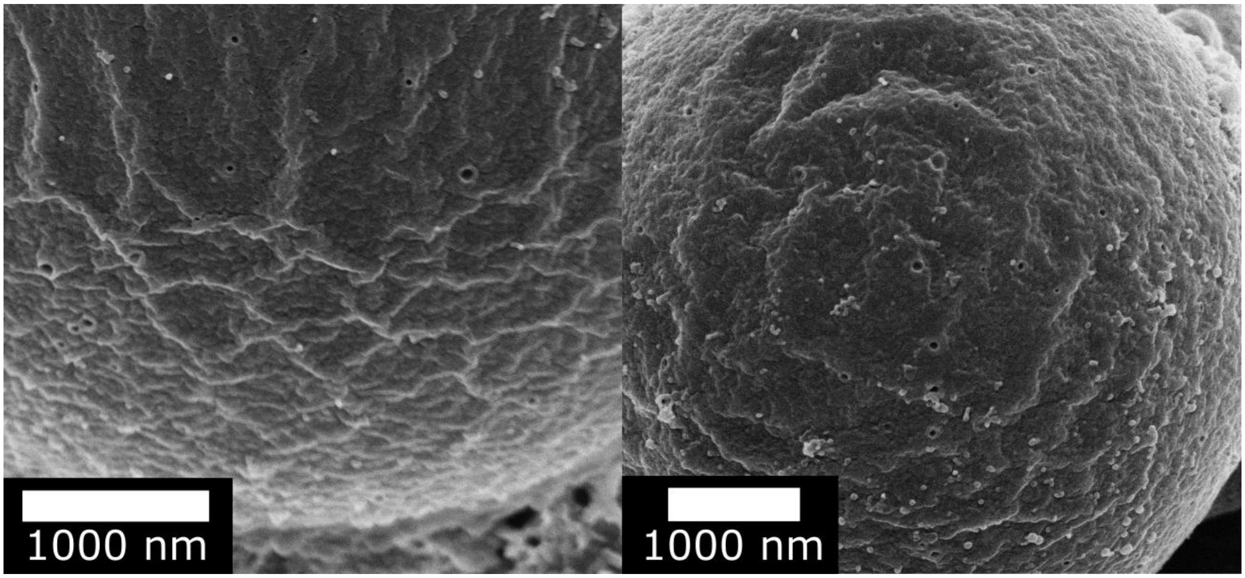

Figure S5: SEM images of PEO_{45}-*b-PMMA*$_{300}$ microparticles with pores.

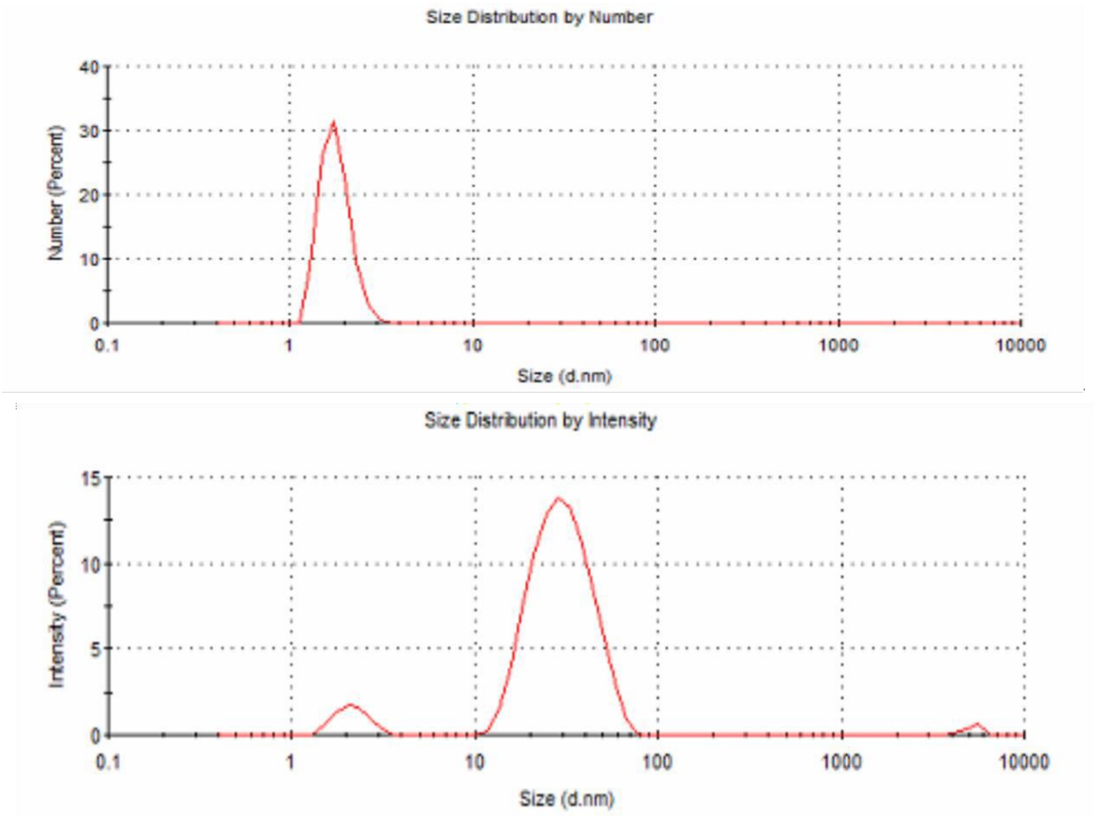

Figure A6: DLS size distribution by number and intensity of PEO45-*b*-PMMA300 homogenous sample $\varphi_W = 0.10$.

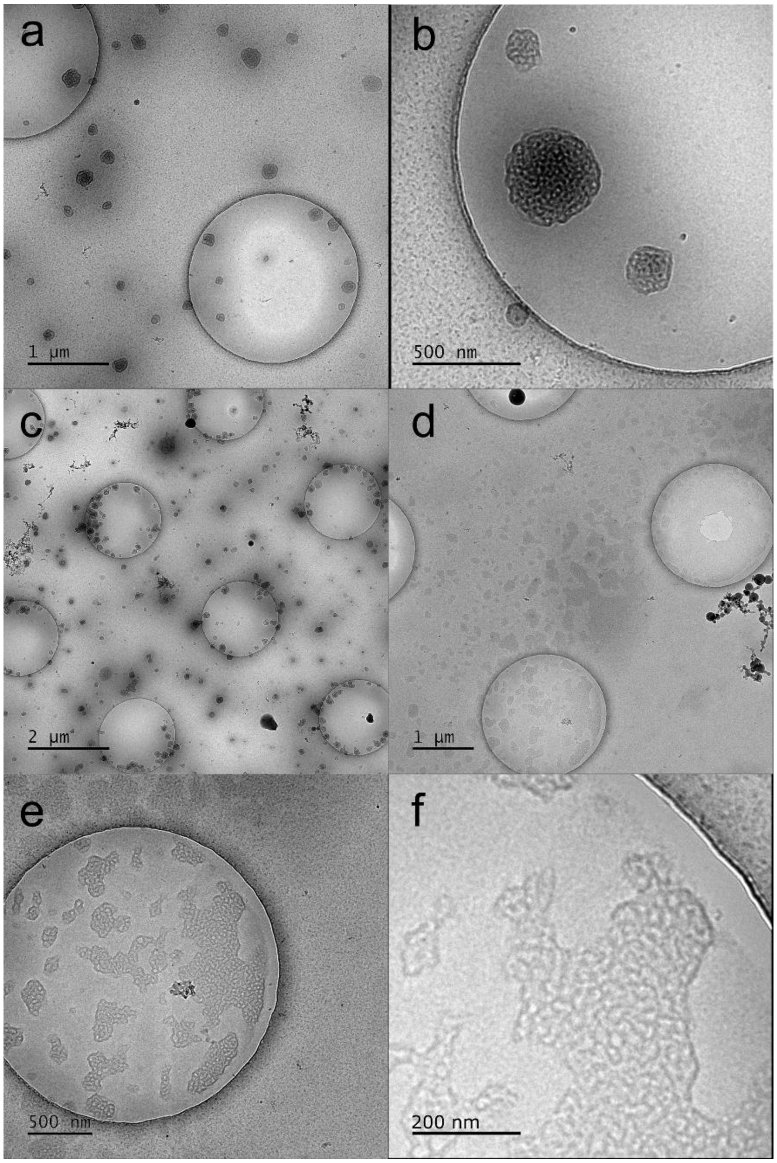

Figure A7: Cryo-TEM images of PEO45-PMMA300 assemblies formed on the TEM grid during sample prep. Initial φ_W= 0.15, final φ_W > 0.30 as we see nanoparticle formation around the TEM grid. (a-c) Bicontinuous nano spheres formed from nano-coacervates. (d-f) Coacervate fields that were flattened out during the sample prep with continuous structure within them.

.

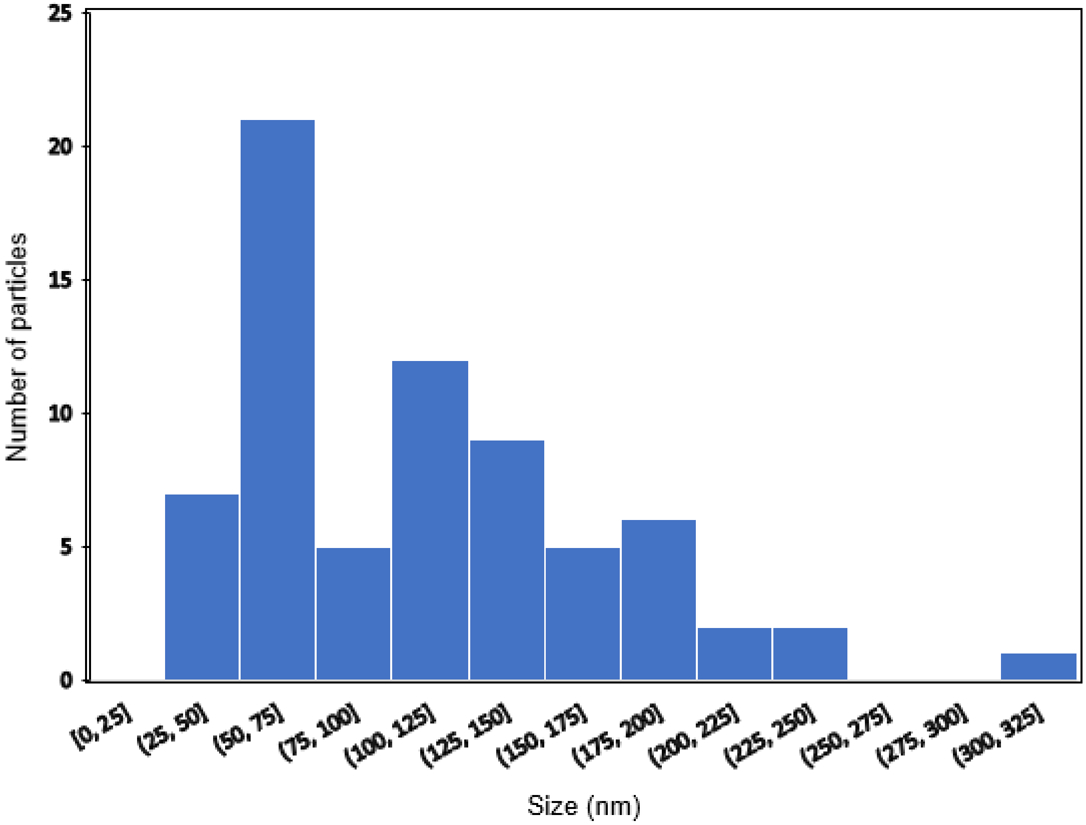

Figure A8: Size distribution histogram of PEO_{45}-*b*-$PMMA_{300}$ bicontinuous structures from the Cryo-TEM experiments (Figure 4f).

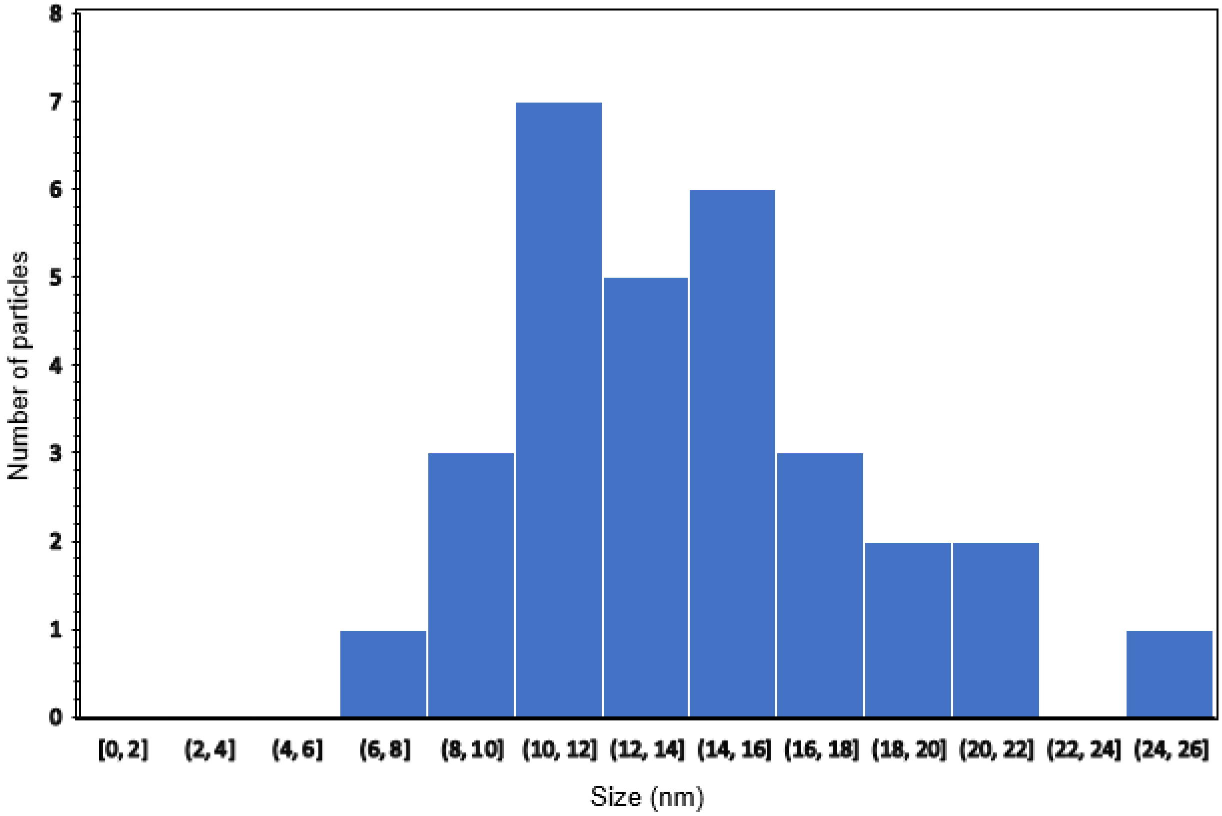

Figure A9: Size distribution histogram of pores on the PEO_{45}-*b*-$PMMA_{300}$ bicontinuous structures from the Cryo-TEM experiments (Figure 4f).

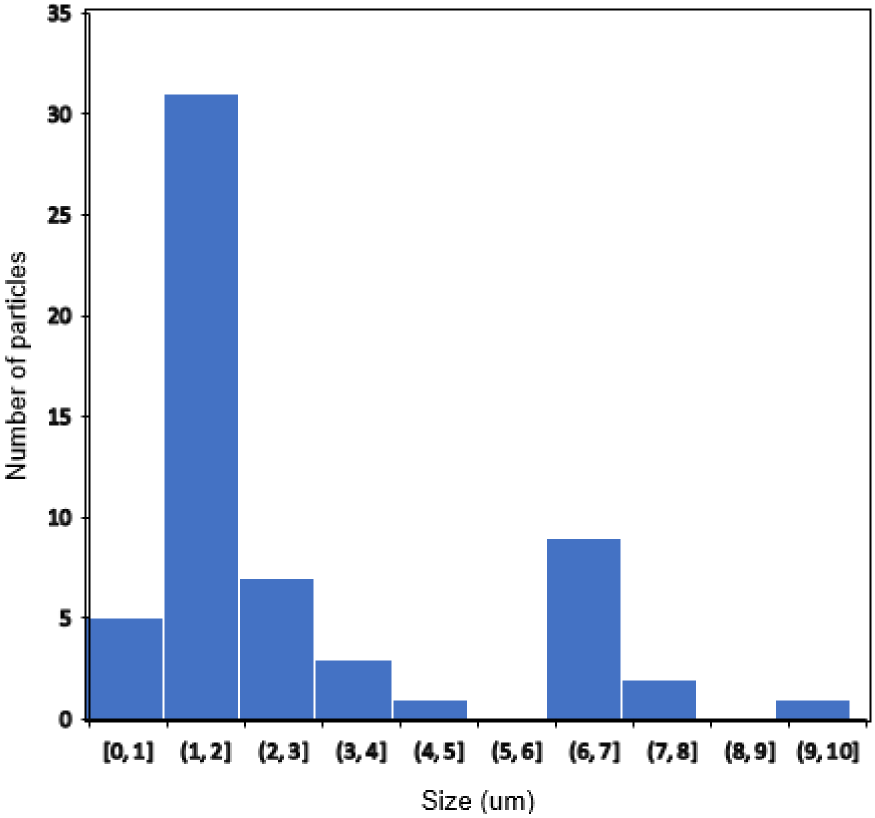

Figure A10: Size distribution histogram of PEO_{45}-*b*-$PMMA_{300}$ microparticles from the SEM experiments (Figure 4d).

.

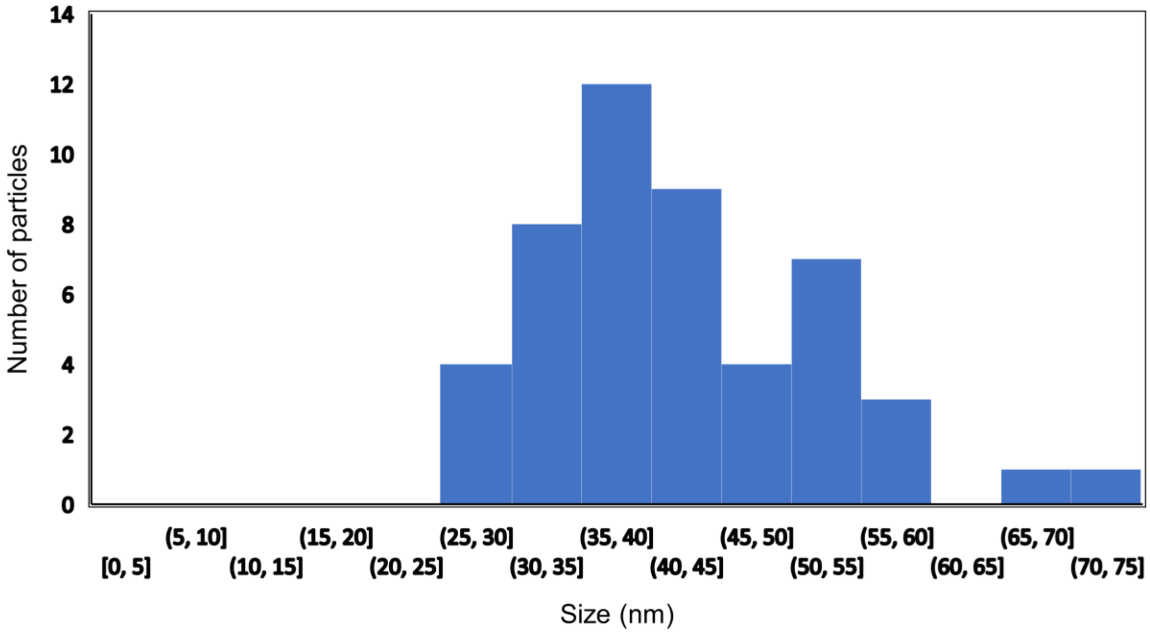

Figure A11: Size distribution histogram of pores on the PEO$_{45}$-*b*-PMMA$_{300}$ microparticles from the SEM experiments (Figure 4d).

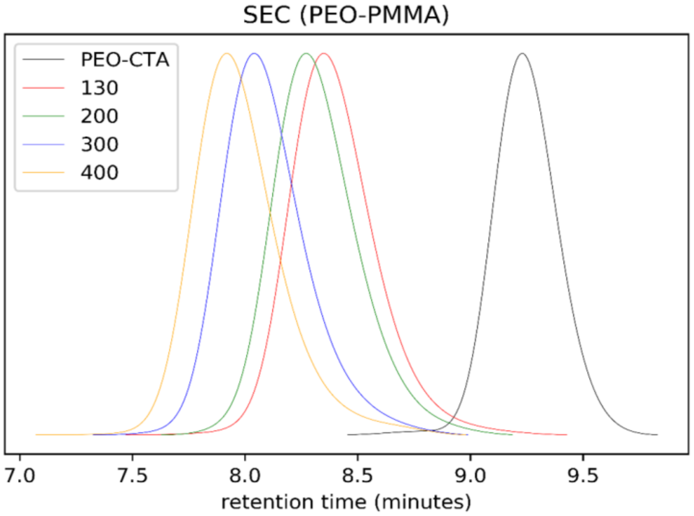

Figure A12: Chromatogram of polyethyeleneoxide MacroCTA and the series of polyethyeleneoxide-*b*-polymethyl methacrylate (PEO-*b*-PMMA) with increasing degree of polymerization for the PMMA block.

.

^{1}H NMR:

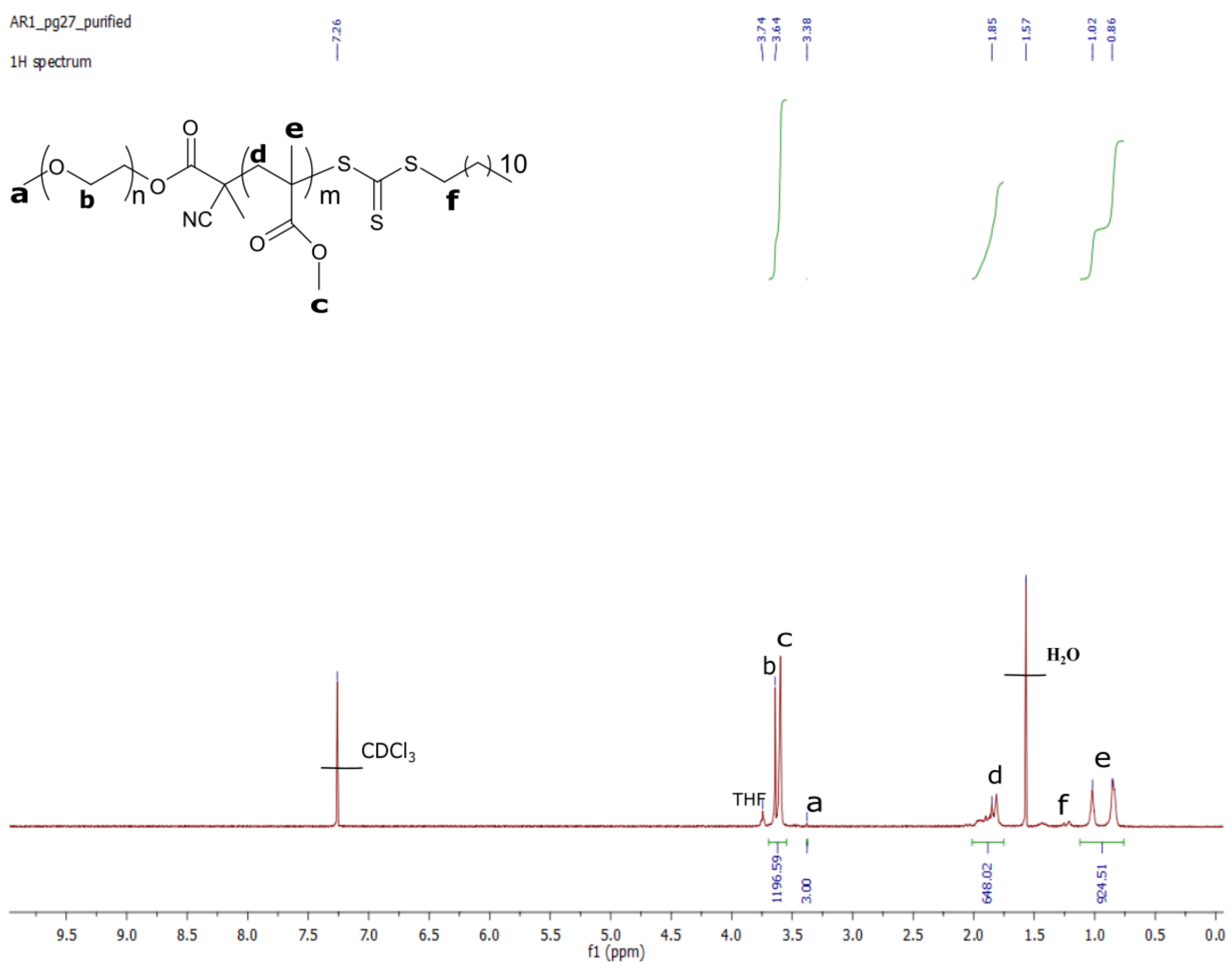

Figure A13: ^{1}H NMR spectrum of PEO$_{45}$-*b*-PMMA$_{300}$ Solvent: CDCl$_3$

.

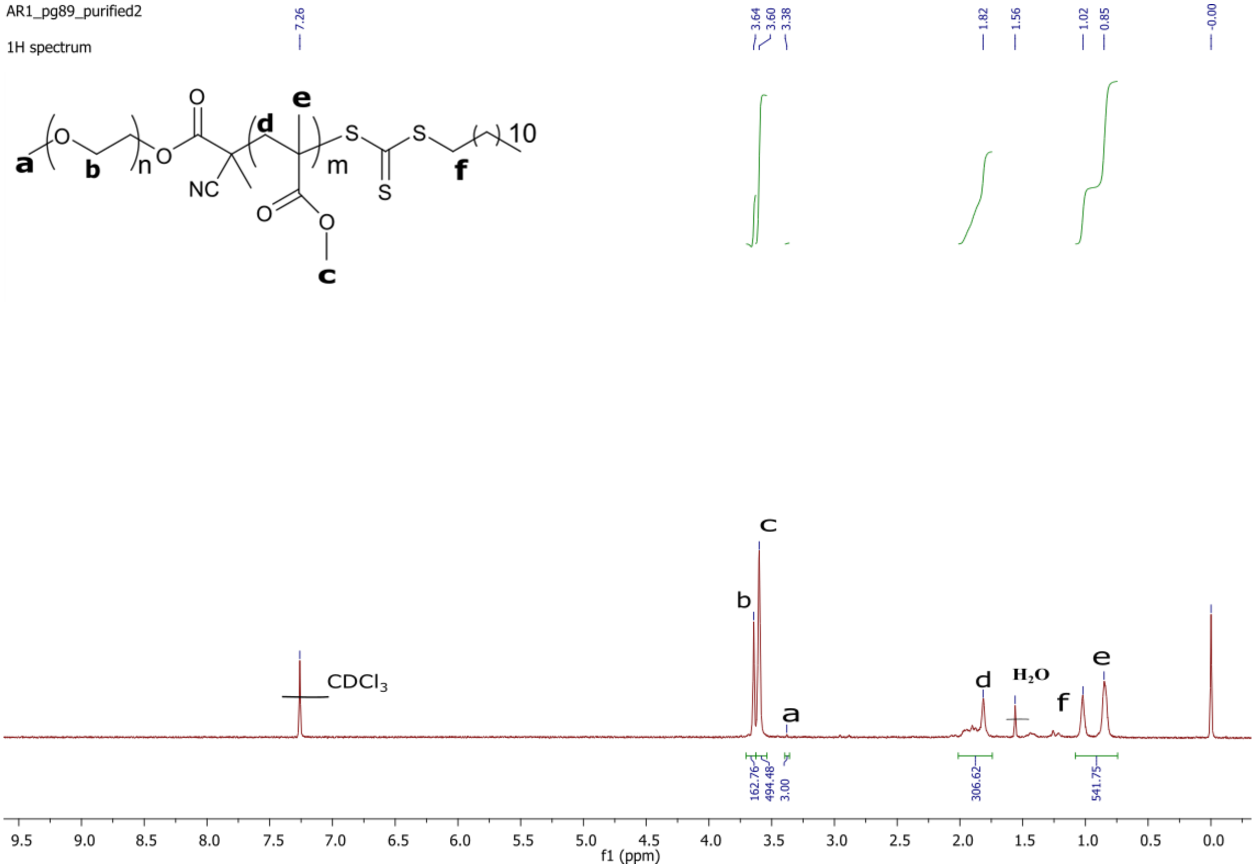

Figure A14: ^{1}H NMR spectrum of PEO$_{45}$-*b*-PMMA$_{130}$ Solvent: CDCl$_3$ (TMS)

.

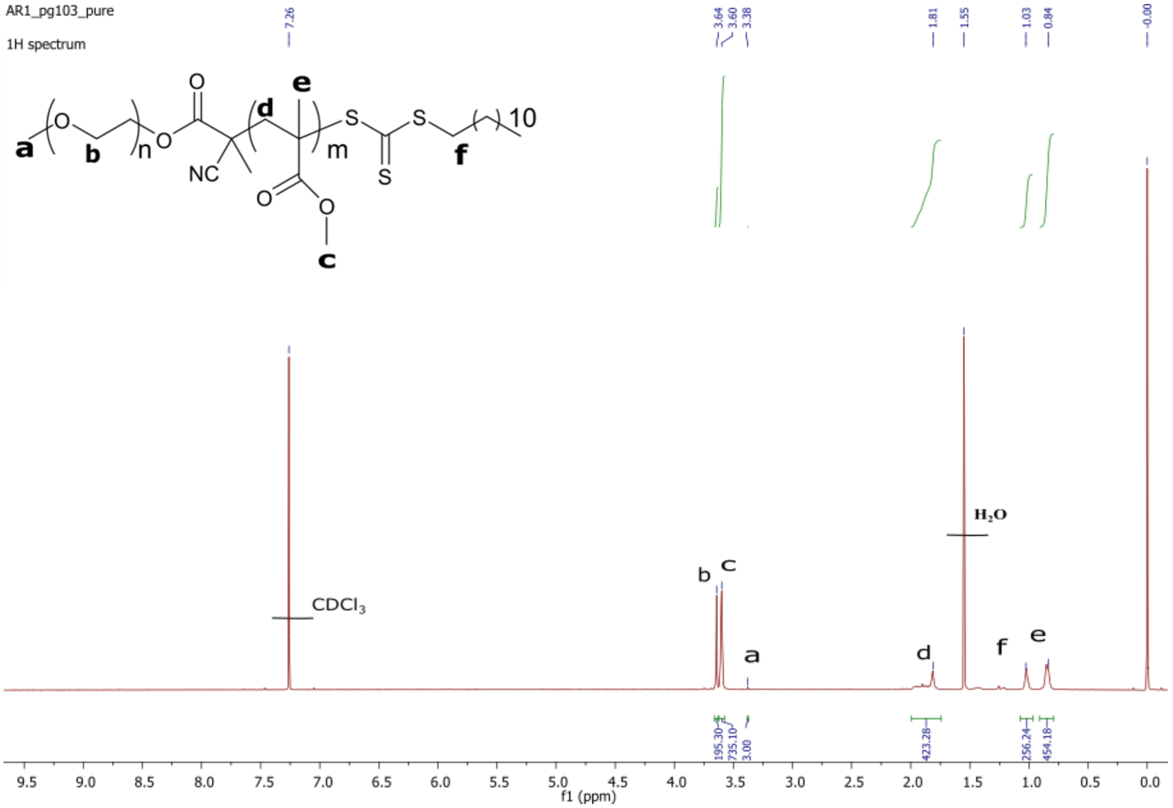

Figure A15 :^{1}H NMR spectrum of PEO$_{45}$-*b*-PMMA$_{200}$ Solvent: CDCl$_3$ (TMS)

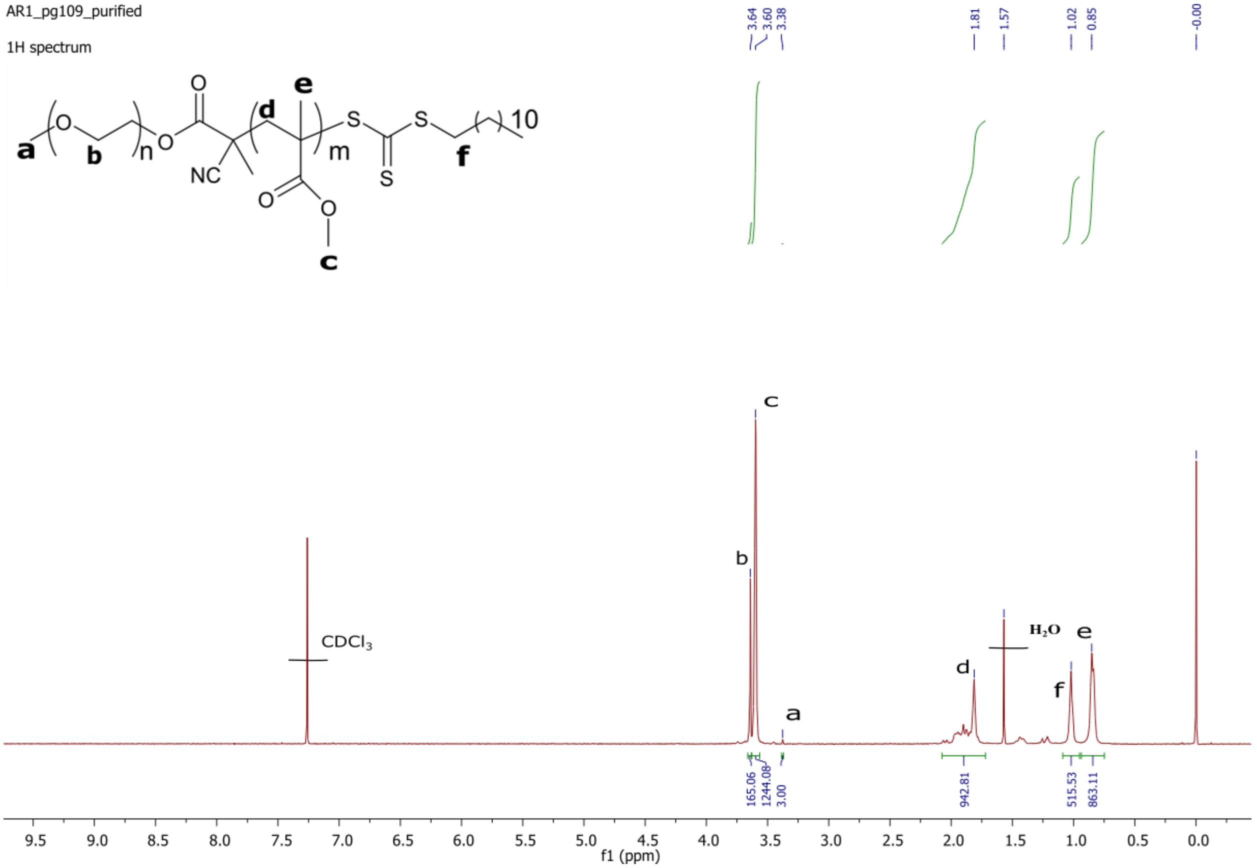

Figure A16: ^{1}H NMR spectrum of PEO$_{45}$-*b*-PMMA$_{400}$ Solvent: CDCl$_3$ (TMS)

.

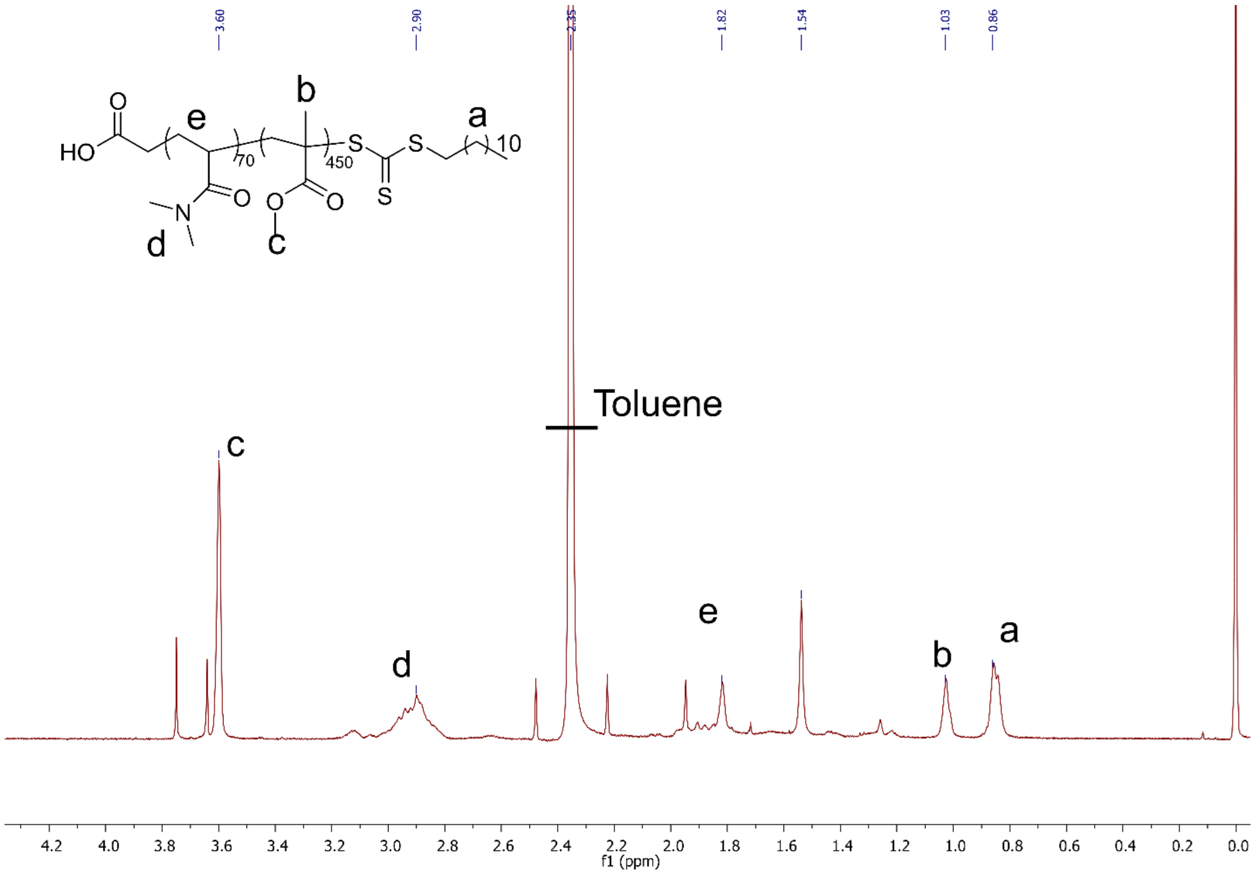

Figure A17: ^{1}H NMR spectrum of PDMA$_{70}$-*b*-PMMA$_{450}$ Solvent: CDCl$_3$ (TMS)

Chapter 3: Liquid-liquid phase separation induced confinement of block copolymers

3.1 Introduction

Self-assembly of block copolymers allows for the synthesis of a wide range of nanoparticle morphologies.[1] Some of the most common morphologies of block copolymer nanoparticles include, spherical micelles, worms, and vesicles. Such morphologies can be accessed using the conventional self-assembly methods like solvent switch self-assembly,[2] or polymerization induced self-assembly.[3] Block copolymers based materials are used in the development of many applications like drug delivery systems,[4] mesoporous membranes,[5] nano-reactors,[6] and lubricants.[7] More recently, block copolymers are being used to develop new “unconventional” morphologies by assembling them in 3D soft-confinement.[8] These morphologies include anisotropic oblate particles,[9] and particles with rich internal morphologies like helical cavities that emerge due the confinement effects.[10] Such morphologies are explored for new applications like particle shape dependent rheology,[11] photonics,[12] and templating.[13]

3D soft-confinement is typically achieved by using oil in water emulsion systems.[14] In short, an emulsion is created by combining an organic phase that has block copolymers and an aqueous phase containing surfactants, which results in the formation of polymer containing oil droplets stabilized by surfactants. The system is then heated to evaporate organic solvent droplets. This causes droplet volume to decrease continuously, and the concentration of block copolymers to increase, leading the block copolymers to form ordered domains due to microphase separation. This procedure has proven robust to generate unique confined morphologies but requires higher temperatures and additional surfactants. Surprisingly, some of the reported confined morphologies have been observed in block copolymer systems where confinement was not used.[15–17] The mechanism for the formation of these structures is unknown when not prepared under 3D soft-confinement. Here we use the conventional solvent switch method to prepare “confined” morphologies and propose a mechanism of their formation during the solvent switch process.

Recently multiple reports have shown that block copolymers undergo liquid-liquid phase separation (LLPS) during the solvent switch process.[18–21] LLPS during the solvent switch self-assembly of block copolymer results in the formation of coacervate droplets that act as precursors to the self-assembled particles.[19] This coacervate precursor was shown to control size and morphologies of the prepared particles. The coacervate droplets form on the nanoscale at a critical concentration of the selective solvent and grow via coalescence to micron sizes and eventually macrophase separate forming two distinct layers.[19] The facile growth is due to the dynamic nature of the droplets and no surfactant layers present at the interface to minimize coalescence. As the solvent switch process is continued, the coacervate droplets turn into self-assembled block copolymer particles. The self-assembly occurs at the interface of the coacervate droplets as the solvent within the coacervates is expelled out.[18] This process resembles a lot like the confinement procedure in which the phase separated emulsion droplets are evaporated. The “confined” morphologies during the solvent switch self-assembly of block copolymers thus occur due to the auto-confinement of the block copolymers within the coacervate droplets as depicted in Figure 1.

3.2 Results & Discussion

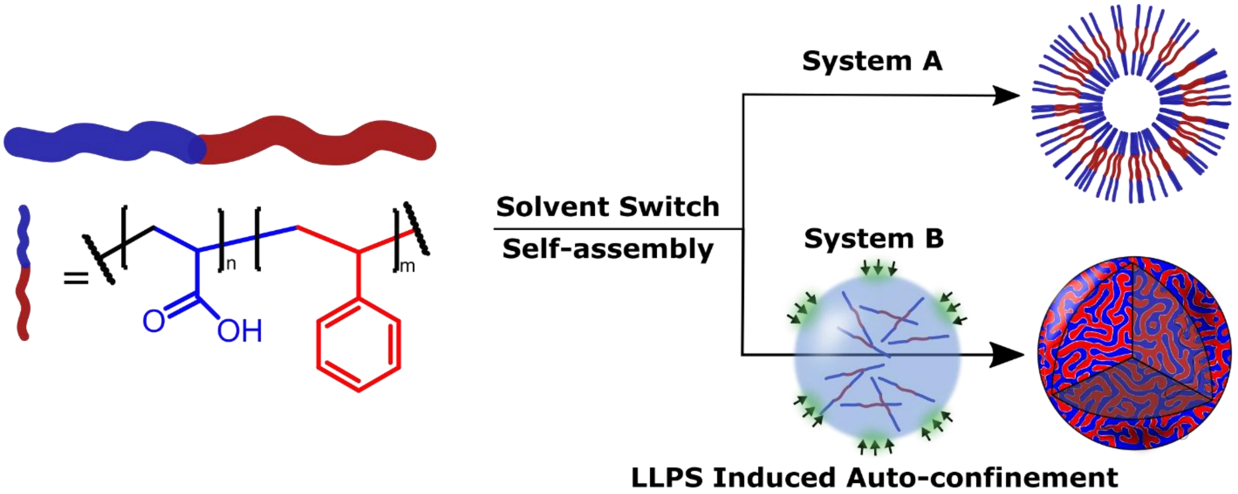

Figure 3.1: Self-assembly overview of polystyrene-*block*-poly acrylic acid with and without LLPS induced confinement. System A proceeds with no confining effects forming vesicles. System B proceeds through stable LLPS intermediates which induce auto-confinement of the block copolymers forming “confined” morphologies.

We use polystyrene-*block*-poly acrylic acid to explore LLPS induced auto-confinement of block copolymers during the solvent switch process. We selected PS-*b*-PAA for our studies as it is one of the most widely studied block copolymer for solution phase self-assembly. [22–24] PS$_{200}$-*b*-PAA$_{35}$ was synthesized using reversible addition-fragmentation transfer (RAFT) polymerization, and the phase behavior of PS$_{200}$-*b*-PAA$_{35}$ was explored as shown in Figure 2. The “good” solvents for this polymer were explored based on previous literature, [22–24] the “selective” solvent in all experiments was water and the starting polymer concentration was 10 mgmL^{-1}. More details on the experimental set up are provided in Appendix 3. As seen in Figure 2a, PS$_{200}$-*b*-PAA$_{35}$ had the highest propensity for LLPS when 1:4 THF:Dioxane was used as the good solvent. In the case of pure dioxane, no LLPS was observed as seen in Figure 2c. With these two systems at hand, we further explore the phase trajectories to determine the phase boundaries at which LLPS and self-assembly occurs during the solvent switch.

As seen in Figure 3a, PS_{200}-*b*-PAA_{35} in 1:4 THF:Dioxane undergoes LLPS at the critical concentration of ≈10% water by volume (v/v). The samples at different water percentages were centrifuged to determine which ones had coacervate droplets as they easily settle down as shown in Figure 2a. The droplets can be resuspended by vortexing the sample and imaged using optical microscopy as shown in Figure 2b-e. Furthermore, PS_{200}-*b*-PAA_{35} in pure dioxane did not form any stable coacervate droplets as shown in Figure 2b, and it self-assembled at ≈15% water v/v as seen by its phase trajectory shown in Figure 3a. This indicates that PS_{200}-*b*-PAA_{35} will not have stable caocervates as precursor to the final self-assembled structures. With the knowledge of where each system forms self-assembled particles, we further characterize the morphologies made in each system to compare the effects of no confinement (System A) to LLPS induced auto-confinement (System b) on the self-assembly outcome of PS_{200}-*b*-PAA_{35}.

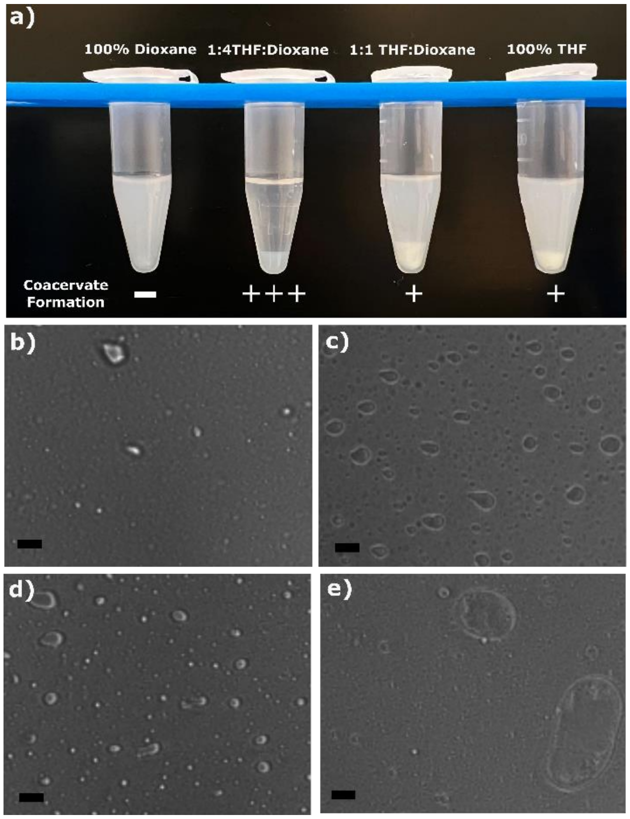

Figure 3.2: Phase behavior of PS_{200}-*b*-PAA_{35} in a series of "good" solvents. a) Photograph of PS_{200}-*b*-PAA_{35} in "good" solvents, titled above each sample, in critical concentrations of water. a) Optical microscopy of PS_{200}-*b*-PAA_{35} in dioxane showing no droplets. b) Optical microscopy of PS_{200}-*b*-PAA_{35} in 1:4 THF:dioxane showing most droplets. c) Optical microscopy of PS_{200}-*b*-PAA_{35} in 1:1 THF:dioxane showing droplets and microparticles. d) Optical microscopy of PS_{200}-*b*-PAA_{35} in THF showing some droplets. Scale bars = 10 µm.

To compare self-assembled morphologies for each system **A** and **B**, we carried out the solvent switch process until the water concentration reached 50% v/v. (See Appendix for more details). Being at 50% v/v water ensures that both systems were well into the self-assembled regime and no reorganization of the nanoparticle morphologies would occur (Figure 3a). Following the solvent switch, the particles were further dialyzed against water for the complete removal of the organic solvents to prepare samples for cryo-transmission electron microscopy (cryo-TEM) as shown in Figure 3b,c. In system A, PS_{200}-*b*-PAA_{35} self-assembled into vesicles with no internal morphology as shown in Figure 3b. We anticipated this result as system A does not form stable LLPS droplets during the solvent switch process which would favor more complex “confined” morphologies. In system B, PS_{200}-*b*-PAA_{35} forms complex morphologies with helical internal cavities as shown in Figure 3c. The formation of this type of morphology is only explained by spherical confinement of the block copolymers in the present literature.[10,25] Chi et.al carried out Monte Carlo simulations of block copolymers in poor solvents with applied spherical confinement.[25] Their simulations predicted a series of unique structures including spheres with internal helical cavities identical to the ones shown in Figure 3c.

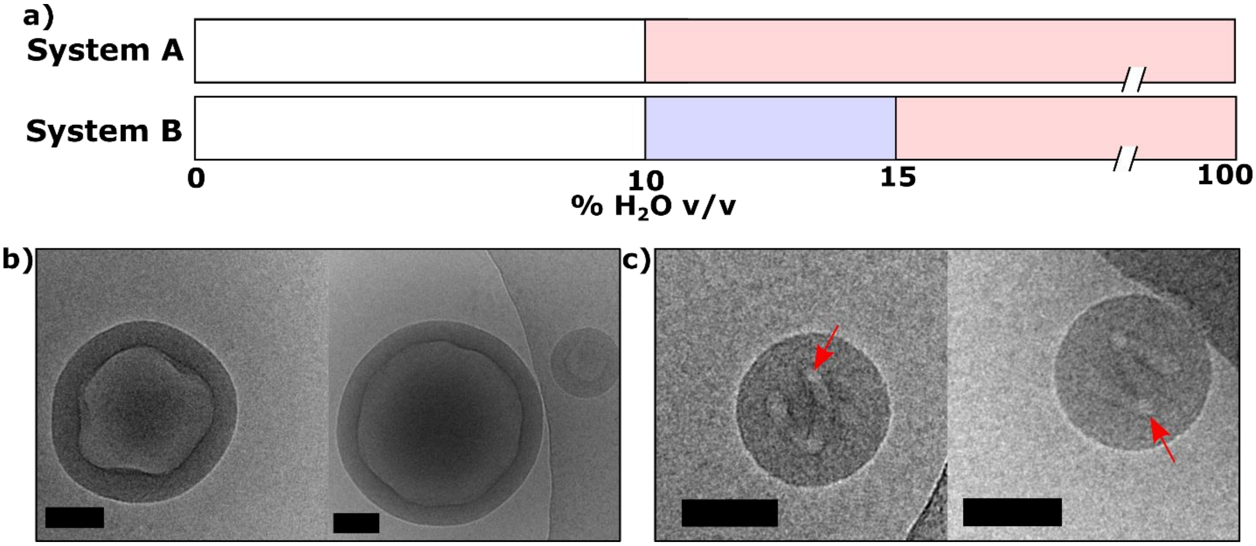

Figure 3.3: Self-assembly of PS_{200}-*b*-PAA_{35}. a) Experimentally mapped phase trajectories of PS_{200}-*b*-PAA_{35} in dioxane (system A) and 1:4 THF:dioxane (system B), white indicates dissolved polymer, blue indicates coacervate formation, and red indicates self-assembled structures. c) Cryo-TEM images of PS_{200}-*b*-PAA_{35} vesicles assembled in system A. d) Cryo-TEM images of PS_{200}-*b*-PAA_{35} nanoparticle assembled in system B showcasing a “confined” morphology of a sphere with a helical cavity as indicated by the red arrows.

The self-assembly outcomes in system A and B support our proposed mechanism in which block copolymers can undergo LLPS induced auto confinement during the solvent switch procedure when system can form stable intermediate droplets, like system B. It is important to note that, despite the formation of vesicles, it is possible that system A undergoes LLPS which is only transient as previously observed.[18] We imagine in such a case where LLPS is transient, the droplets do not reach equilibrium concentration of polymers within them. With a lower concentration within the droplets, block copolymers do not undergo confinement. More experiments using in-situ techniques will be needed to further understand this process.

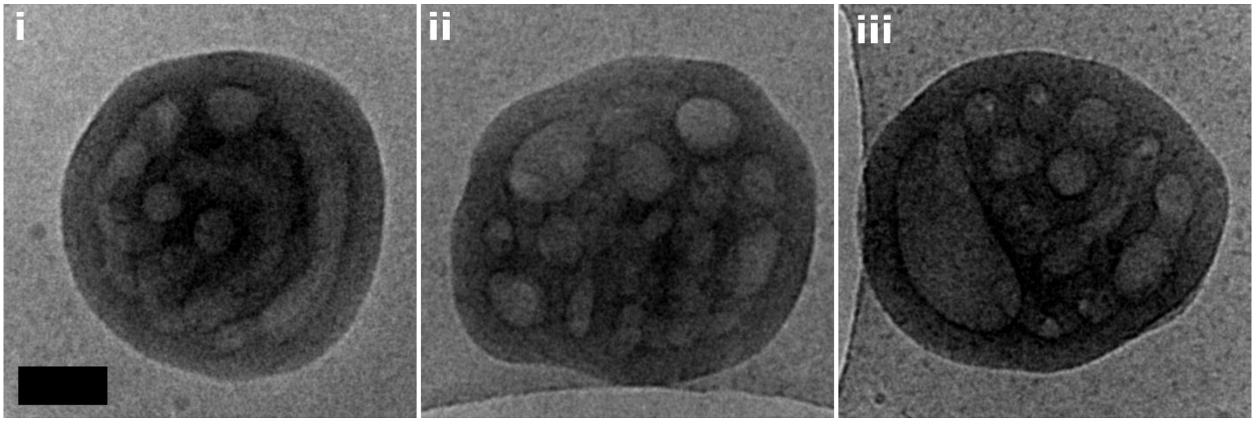

Figure 3.4: Variety of self-assembled morphologies from system B. i-ii) Cryo-TEM images of additional confined morphologies made by LLPS induced auto confinement. Such morphologies can be found in simulation predictions of block copolymer assembly in soft-confinement as described in ref (25).

In system B, where LLPS induced auto confinement occurs, we observe a diverse set of morphologies (Figure 4) as compared to system A in which we only observed vesicles (Figure 3a). The dispersity of the self-assembled particles could arise from varying rates of solvent expulsion from the intermediate droplets, and coalescence of the intermediate droplets as no surfactant layer is present at the droplet interface in our systems. It is known for emulsion based confining systems that the rate of evaporation has a direct influence on the self-assembled morphologies.[9] As the droplets form and evolve during the solvent switch process in our system, it is reasonable to imagine that some droplets coalesce together resulting in varying rates of diffusion of the organic solvent out of the droplets. The different morphologies shown in Figure 4 i-iii closely resemble those predicted using simulations of block copolymers under spherical confinements.[25] As they are unique structures not discussed in the literature much, we have labeled them numerically here. Furthermore, the structure of I, II, and III resemble many of the mesoporous block copolymer particles made using emulsion based confinement.[26] We aim to gain more control and mechanistic understanding of such unique morphologies in future works.

3.3 Conclusion

In conclusion, we have used a classic block copolymer PS-*b*-PAA to demonstrate that PS_{200}-*b*-PAA_{35} can assemble into "confined" morphologies just by using the traditional solvent switch process. These morphologies emerge due to the LLPS induced auto-confinement of block copolymers in systems that can form stable coacervate droplets. While not explored explicitly, such a mechanism has been speculated at different instances.[15,21] Furthermore, we showed that the same block copolymer, PS_{200}-*b*-PAA_{35}, does not assemble into "confined" structures when the "good" solvent does not favor stable coacervates to form. We used optical microscopy and cryo-TEM to characterize coacervate intermediates and the self-assembled structures respectively. Multiple "confined" morphologies were observed in system B which matched the ones predicted by simulations in literature. More work will be required to understand the effect of different parameters on the LLPS induced auto-confinement like, "selective" solvent addition rates, block copolymer molecular weight, and concentration. We predict the use of traditional solvent switch method to access “confined” morphologies will be attractive for industrial uses as it does not require heating the system or additional surfactants.

3.4 References

(1) Mai, Y.; Eisenberg, A. Self-Assembly of Block Copolymers. *Chem. Soc. Rev.* **2012**, *41* (18), 5969–5985. https://doi.org/10.1039/C2CS35115C.

(2) G. Denkova, A.; H. Bomans, P. H.; Coppens, M.-O.; M. Sommerdijk, N. a. J.; Mendes, E. Complex Morphologies of Self-Assembled Block Copolymer Micelles in Binary Solvent Mixtures: The Role of Solvent – Solvent Correlations. *Soft Matter* **2011**, *7* (14), 6622–6628. https://doi.org/10.1039/C1SM05461A.

(3) Penfold, N. J. W.; Yeow, J.; Boyer, C.; Armes, S. P. Emerging Trends in Polymerization-Induced Self-Assembly. *ACS Macro Lett.* **2019**, *8* (8), 1029–1054. https://doi.org/10.1021/acsmacrolett.9b00464.

(4) Rösler, A.; Vandermeulen, G. W. M.; Klok, H.-A. Advanced Drug Delivery Devices via Self-Assembly of Amphiphilic Block Copolymers. *Advanced Drug Delivery Reviews* **2012**, *64*, 270–279. https://doi.org/10.1016/j.addr.2012.09.026.

(5) Park, C.; La, Y.; An, T. H.; Jeong, H. Y.; Kang, S.; Joo, S. H.; Ahn, H.; Shin, T. J.; Kim, K. T. Mesoporous Monoliths of Inverse Bicontinuous Cubic Phases of Block Copolymer Bilayers. *Nature Communications* **2015**, *6* (1), 6392. https://doi.org/10.1038/ncomms7392.

(6) Kim, K. T.; Meeuwissen, S. A.; Nolte, R. J. M.; Hest, J. C. M. van. Smart Nanocontainers and Nanoreactors. *Nanoscale* **2010**, *2* (6), 844–858. https://doi.org/10.1039/B9NR00409B.

(7) Derry, M. J.; Smith, T.; O’Hora, P. S.; Armes, S. P. Block Copolymer Nanoparticles Prepared via Polymerization-Induced Self-Assembly Provide Excellent Boundary Lubrication Performance for Next-Generation Ultralow-Viscosity Automotive Engine Oils. *ACS Appl. Mater. Interfaces* **2019**, *11* (36), 33364–33369. https://doi.org/10.1021/acsami.9b12472.

(8) Shin, J. J.; Kim, E. J.; Ku, K. H.; Lee, Y. J.; Hawker, C. J.; Kim, B. J. 100th Anniversary of Macromolecular Science Viewpoint: Block Copolymer Particles: Tuning Shape, Interfaces, and Morphology. *ACS Macro Lett.* **2020**, *9* (3), 306–317. https://doi.org/10.1021/acsmacrolett.0c00020.

(9) Ku, K. H.; Lee, Y. J.; Kim, Y.; Kim, B. J. Shape-Anisotropic Diblock Copolymer Particles from Evaporative Emulsions: Experiment and Theory. *Macromolecules* **2019**, *52* (3), 1150–1157. https://doi.org/10.1021/acs.macromol.8b02465.

(10) Zhao, F.; Xu, Z.; Li, W. Self-Assembly of Asymmetric Diblock Copolymers under the Spherical Confinement. *Macromolecules* **2021**, *54* (24), 11351–11359. https://doi.org/10.1021/acs.macromol.1c02250.

(11) Shin, J. M.; Kim, Y.; Ku, K. H.; Lee, Y. J.; Kim, E. J.; Yi, G.-R.; Kim, B. J. Aspect Ratio-Controlled Synthesis of Uniform Colloidal Block Copolymer Ellipsoids from Evaporative Emulsions. *Chem. Mater.* **2018**, *30* (18), 6277–6288. https://doi.org/10.1021/acs.chemmater.8b01821.

(12) Song, D.-P.; Zhao, T. H.; Guidetti, G.; Vignolini, S.; Parker, R. M. Hierarchical Photonic Pigments via the Confined Self-Assembly of Bottlebrush Block

Copolymers. *ACS Nano* **2019**, *13* (2), 1764–1771. https://doi.org/10.1021/acsnano.8b07845.

(13) Hwang, J.; Kim, S.; Wiesner, U.; Lee, J. Generalized Access to Mesoporous Inorganic Particles and Hollow Spheres from Multicomponent Polymer Blends. *Advanced Materials* **2018**, *30* (27), 1801127. https://doi.org/10.1002/adma.201801127.

(14) Staff, R. H.; Schaeffel, D.; Turshatov, A.; Donadio, D.; Butt, H.-J.; Landfester, K.; Koynov, K.; Crespy, D. Particle Formation in the Emulsion-Solvent Evaporation Process. *Small* **2013**, *9* (20), 3514–3522. https://doi.org/10.1002/smll.201300372.

(15) Parry, A. L.; Bomans, P. H. H.; Holder, S. J.; Sommerdijk, N. A. J. M.; Biagini, S. C. G. Cryo Electron Tomography Reveals Confined Complex Morphologies of Tripeptide-Containing Amphiphilic Double-Comb Diblock Copolymers. *Angewandte Chemie International Edition* **2008**, *47* (46), 8859–8862. https://doi.org/10.1002/anie.200802834.

(16) Yu, H.; Qiu, X.; Nunes, S. P.; Peinemann, K.-V. Biomimetic Block Copolymer Particles with Gated Nanopores and Ultrahigh Protein Sorption Capacity. *Nat Commun* **2014**, *5* (1), 4110. https://doi.org/10.1038/ncomms5110.

(17) Cameron, N. S.; Corbierre, M. K.; Eisenberg, A. 1998 E.W.R. Steacie Award Lecture Asymmetric Amphiphilic Block Copolymers in Solution: A Morphological Wonderland. **1999**, *77*, 16.

(18) Ianiro, A.; Wu, H.; Rijt, M. M. J. van; Vena, M. P.; Keizer, A. D. A.; Esteves, A. C. C.; Tuinier, R.; Friedrich, H.; Sommerdijk, N. A. J. M.; Patterson, J. P. Liquid–Liquid Phase Separation during Amphiphilic Self-Assembly. *Nat. Chem.* **2019**, *11* (4), 320–328. https://doi.org/10.1038/s41557-019-0210-4.

(19) Rizvi, A.; Patel, U.; Ianiro, A.; Hurst, P. J.; Merham, J. G.; Patterson, J. P. Nonionic Block Copolymer Coacervates. *Macromolecules* **2020**, *53* (14), 6078–6086. https://doi.org/10.1021/acs.macromol.0c00979.

(20) Rizvi, A.; Mulvey, J. T.; Patterson, J. P. Observation of Liquid–Liquid-Phase Separation and Vesicle Spreading during Supported Bilayer Formation via Liquid-Phase Transmission Electron Microscopy. *Nano Lett.* **2021**, *21* (24), 10325–10332. https://doi.org/10.1021/acs.nanolett.1c03556.

(21) Wong, C. K.; Heidelmann, M.; Dulle, M.; Qiang, X.; Förster, S.; Stenzel, M. H.; Gröschel, A. H. Vesicular Polymer Hexosomes Exhibit Topological Defects. *J. Am. Chem. Soc.* **2020**. https://doi.org/10.1021/jacs.0c02009.

(22) Discher, D. E.; Eisenberg, A. Polymer Vesicles. *Science* **2002**, *297* (5583), 967–973. https://doi.org/10.1126/science.1074972.

(23) Choucair, A.; Eisenberg, A. Control of Amphiphilic Block Copolymer Morphologies Using Solution Conditions. *Eur Phys J E Soft Matter* **2003**, *10* (1), 37–44. https://doi.org/10.1140/epje/e2003-00002-5.

(24) Chen, L.; Shen, H.; Eisenberg, A. Kinetics and Mechanism of the Rod-to-Vesicle Transition of Block Copolymer Aggregates in Dilute Solution. *J. Phys. Chem. B* **1999**, *103* (44), 9488–9497. https://doi.org/10.1021/jp9913665.

(25) Chi, P.; Wang, Z.; Li, B.; Shi, A.-C. Soft Confinement-Induced Morphologies of Diblock Copolymers. *Langmuir* **2011**, *27* (18), 11683–11689. https://doi.org/10.1021/la202448c.

(26) Xu, J.-P.; Zhu, J.-T. Block Copolymer Colloidal Particles with Unique Structures through Three-Dimensional Confined Assembly and Disassembly. *Chin J Polym Sci* **2019**, *37* (8), 744–759. https://doi.org/10.1007/s10118-019-2294-0.

Appendix B: Supplementary Information for Chapter 3

B.1 Materials and Instruments:

All reagents were purchased from Acros Organics, Fisher Scientific, or Sigma-Aldrich, and used without further purification unless otherwise noted. ^{1}H NMR spectra were collected on a 500 MHz Bruker Avance spectrometer. All samples were taken in $CDCl_3$. Chemical shifts are provided in ppm, calibrated from the residual $CDCl_3$ peak (7.26 ppm). All TEM experiments were performed on a JEOL 2100 equipped with a 200 keV field emission gun and a OneView camera, Irvine Materials Research Institute, University of California, Irvine. Optical imaging were performed using a Keyence Bz-X810 all in one microscope. Size exclusion chromatography (SEC) was performed in DMF using an Agilent 1100 chromatograph equipped with RID detector and a PL gel 5 µm 300x7.5 mm mixed column. All samples were calibrated against polystyrene standards (MW= 580, 1300, 5000, 10000, 30000, 70000, 130000 g/mol).

C.2 Experimental Methods

C.2.1 Synthesis of $PtBuA_{30}$

To a schlenck tube, [S-dodecyl-S'-(α',α'-dimethyl-α''-acetic acid)] (DDMAT, 0.18 g, 0.5 mmol), tert-butylacrylate (4.0 g, 31.2 mmol), AIBN (8.2 mg, 0.05) were added and dissolved in dioxane (5 mL). The solution was stirred and purged for 30 min with N_2 to deoxygenate the solution. The solution was heated to 65 ^oC for 70 min to initiate the polymerization. The polymerization was stopped by cooling the solution down to 0 ^oC. The viscous solution was dissolved in minimum amount of THF and poured into a mixture (by volume of 7:1 cold $MeOH:H_2O$. The $MeOH:H_2O$ solution was decanted, and the polymer was dissolved in THF and the solution was dried over $MgSO_4$. The solution was filtered, and the solvent was removed *in vacuo* yielding a yellow foam, PtBuA. M_n

(^{1}H NMR) = 4200 g mol^{-1}, M_w/M_n (SEC) = 1.17. ^{1}H NMR ($CDCl_3$): δ (ppm) 3.33 (t, J = 7.4 Hz, 2H, SCSC*H2*), 1.20-1.50 (br, C(CH3)3 polymer backbone), 1.30-2.30 (br, CH and CH2 polymer backbone) 0.88 (t, J 6.8 Hz, 3H, (CH2)11C*H*3).

Chain Extension of P*t*BuA with Styrene to give P*t*BuA$_{30}$-b-PS$_{200}$

To a schlenck tube, **P^{t}BuA$_{30}$** (2.7 g, 0.42 mmol), Styrene (18.3 g, 175.4 mmol) were added and the solution was purged with N_2 while stirring to deoxygenate the solution. The solution was then heated to 110 ^oC overnight and cooled to 0 ^oC to stop the polymerization. The reaction mixture had “gelled” due to high styrene concentration, which restricted the conversion calculation. The gelled solution was dissolved in THF with sonication for several hours. The dissolved polymer solution was precipitated into cold MeOH three times. The Polymer was filtered and dried *in vacuo* (16 g). M_n (^{1}H NMR)= 25,000 g mol^{-1}. M_w/M_n (SEC) = 1.21. ^{1}H NMR (CDCl3): δ (ppm) 6.25-7.25 (br, Ar-H polymer backbone), 3.33 (br, 2H, SCSC*H2*), 1.20-1.50 (br, C(CH3)3 polymer backbone), 1.30-2.30 (br, CH and CH2 polymer backbone) 0.88 (br, 3H, (CH2)11C*H*3).

Conversion of P*t*BuA$_{30}$-b-PS$_{200}$ to PAA$_{30}$-b-PS$_{200}$

P*t*BuA$_{30}$-b-PS$_{200}$ (2.0 g, 0.09 mmol) was charged into a 250 mL round bottom flask with a stir bar. The polymer was dissolved in DCM (80 mL) and cooled to 0 ^oC in an ice bath. After the solution was cooled, TFA (40 mL) was slowly added to the reaction mixture, the reaction was stirred overnight. The cloudy solution was dried in air and the solids were dissolved in THF, the undissolved precipitate was filtered, and the polymer solution was precipitated twice into cold MeOH. The polymer was filtered and dried *in vacuo* (1.1 g). FT-IR was used to confirm the deprotection of the tertbutyl group (Figure S9).

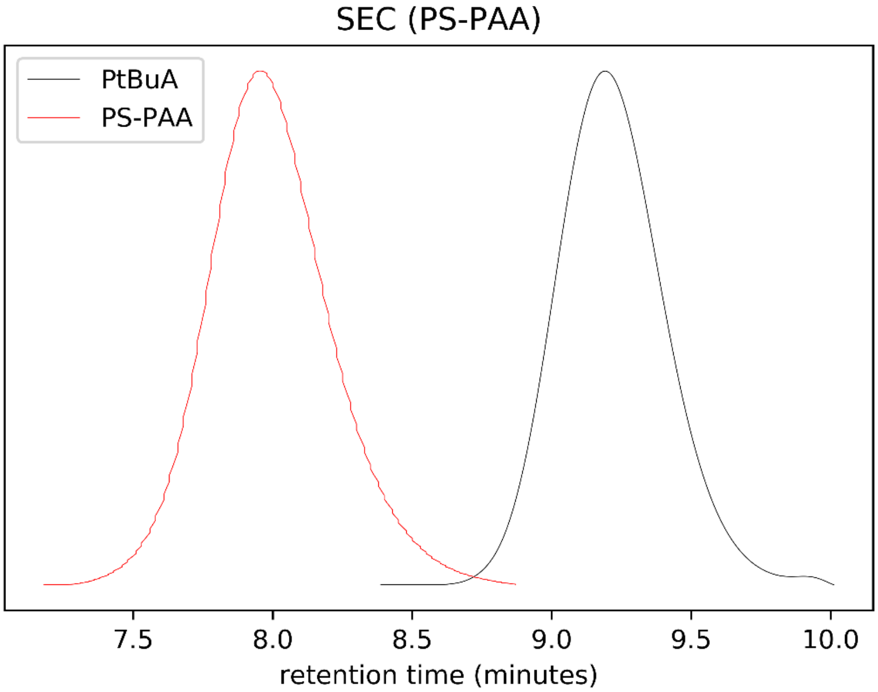

Figure C1: Chromatogram of PolytertButyl acrylate and Poly(styrene)$_{200}$-*b*-polyacrylic acid$_{30}$.

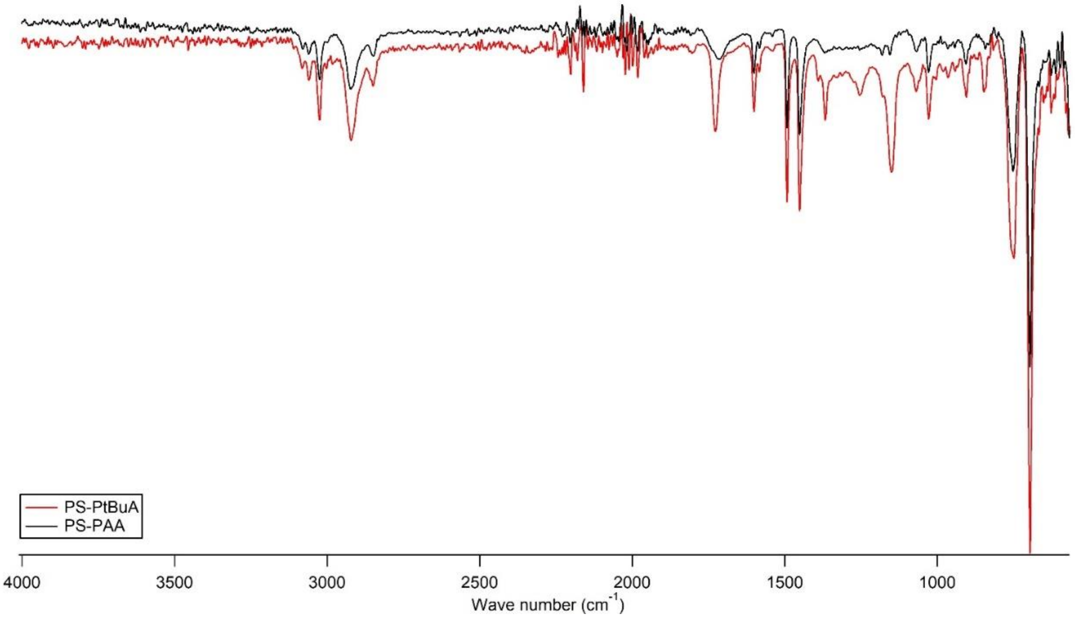

Figure C2: FTIR spectra of PS_{200}-$PtBuA_{30}$ and PS_{200}-PAA_{30} overlayed. The blue box highlights the conversion of the sharp ester carbonyl peak to the broader carboxylic acid carbonyl peak.

B.2.3 Size exclusion chromatography

A solution of 1 mg ml^{-1} is made in DMF and filtered using a 0.2 µm syringe filter. A GPC vial is charged with the filtered solution and sealed with slit containing cap. The vial is placed in the autosampler, and the standard GPC method is used to collect the chromatogram. The results are then evaluated using the most recent polystyrene standards. The SEC results are mainly used to measure the poly dispersity pf the block copolymers as the MW of block copolymers cannot be estimated with confidence using homopolymer standards.

B.2.4 Solvent switch self-assembly

1 mL solution of 10 mg mL^{-1} of PS_{200}-*b*-PAA_{30} was added to a vial with a stir bar and sealed with a septum cap. A syringe was used to dispense water to reach the desired water concentration v/v. The syringe was loaded on to a syringe pump and the water was dispensed at a rate of 20 µL min^{-1}. The solution was constantly stirred and monitored to note any turbidity changes as the water concentration was increased.

B.2.5 Optical Microscopy

Standard microscope slides along with 1.0 mm coverslips were used to prepare samples for bright-field imaging using the Keyence optical microscope. Coacervate samples were vortexed for 10 s and then 20 µL of coacervate solution was sealed between the glass slide and the coverslips for imaging each sample. Images were collected with 10x and 20x objective lenses. The images were not further modified after collection.

B.2.6 Cryo-electron microscopy of block copolymer assemblies

CryoTEM Quantifoil Holey Carbon Films were purchased from Electron Microscopy Sciences, grids were glow discharged for 70 s to increase hydrophilicity prior to sample preparation. Vitrification was carried out by an Automatic Plunge Freezer ME GP2 (Leica Microsystems) where sample preparation onto cryoTEM grids was carried out at 95% humidity to prevent evaporation and blotted for (2, 3 or 4) s before autoplunging into liquid propane. Vitrified samples were studied on a JEOL-2100F TEM using a Schottky type field emission gun operating at 200 kV. Cryo-TEM images were analyzed using the ImageJ.

Chapter 4: Polymerization Induced Condensation (PICON)

4.1 Introduction

Liquid-liquid phase separation (LLPS) is a ubiquitous process observed in synthetic macromolecular and biological systems.[1,2] In synthetic systems, LLPS is used to develop microporous membranes,[3] protocells,[4] adhesives,[5] and gene delivery systems.[6] In biological systems, LLPS of proteins and other biomolecules is responsible for various processes such as DNA repair,[7] RNA synthesis,[8] and chromatin organization.[9] In some biological systems, the LLPS of macromolecules occurs by an active ongoing reaction, often a polymerization of a biomacromolecule like RNA.[8] The influence of an ongoing polymerization on the phase separating system is not yet understood in biology and synthetic systems. Furthermore, not many synthetic model systems exist in which LLPS occurs due to ongoing polymerization. Recent advances have been made in the field of "active droplets," in which phase separation occurs due to a chemical reaction, usually a small molecule dimerization or a functional group modification on an already existing polymer.[10,11] Thus, it is of high interest to develop systems that undergo LLPS upon active polymerization as model systems.

Polymerization-induced self-assembly (PISA) is a vast field in which block copolymers are synthesized and assembled into nano- or microscale structures.[12] A series of polymerization methods have been used to prepare PISA systems. One common method used is referred to as photo-PISA, which allows for the polymerization to proceed when irradiated with light, often at room temperature. Commonly, a reversible addition-fragmentation transfer (RAFT) photoiniferter is used for photo-initiated polymerizations,[13] which are referred to as photo-RAFT polymerizations. Photo-RAFT PISA systems have been developed to prepare self-assemblies of acrylamide, acrylates, and methacrylate-based block copolymers.[14,15] Most RAFT-PISA systems yield a suspension of synthesized polymer particles, or a supramolecular gel due to the entanglement of anisotropic morphologies.[16] Despite multiple reports noting LLPS as an intermediate during the PISA process,[17,18] droplet morphologies have not been isolated and studied in any reported system. Here, we developed a photo-RAFT system using the chain extension of poly(phenyl acrylate) (PPA) onto a polyethylene oxide macro-CTA (PEO-CTA) in ethanol using blue light. As the polymer reaches a critical degree of polymerization (DP), stable coacervates form due to LLPS and further turn into gel-like particles at higher molecular weights. We also analyze the effects of phase transitions on polymerization kinetics and characterize the different phases using microscopy methods. This process is unique as it condenses the polymers into stable coacervate droplets as the polymerization is carried out, therefore we established this as the first polymerization-induced condensation (PICON) system.

4.2 Results & Discussion

To develop a PICON system we selected a photo-RAFT polymerization of phenyl acrylate with polyethylene oxide macro-CTA as shown in Figure 1a. RAFT polymerization is a versatile method to synthesize block copolymers with good molecular weight control and dispersity.[19] Photo-RAFT uses the commonly used chain transfer agent, DDMAT, as a photoiniferter has been used to prepare a variety of self-assembled materials.[20] Armes and coworkers have developed phenyl acrylate-based block copolymers for PISA systems and map out their phase behaviors.[21] These PPA-based copolymers were synthesized with a thermal initiator such as AIBN. In our studies all PICON reactions were performed at room temperature, with the same solvent (ethanol), the same solid weight percentage (30wt%), and the same irradiation intensity (64 Watts) (see Appenix X).

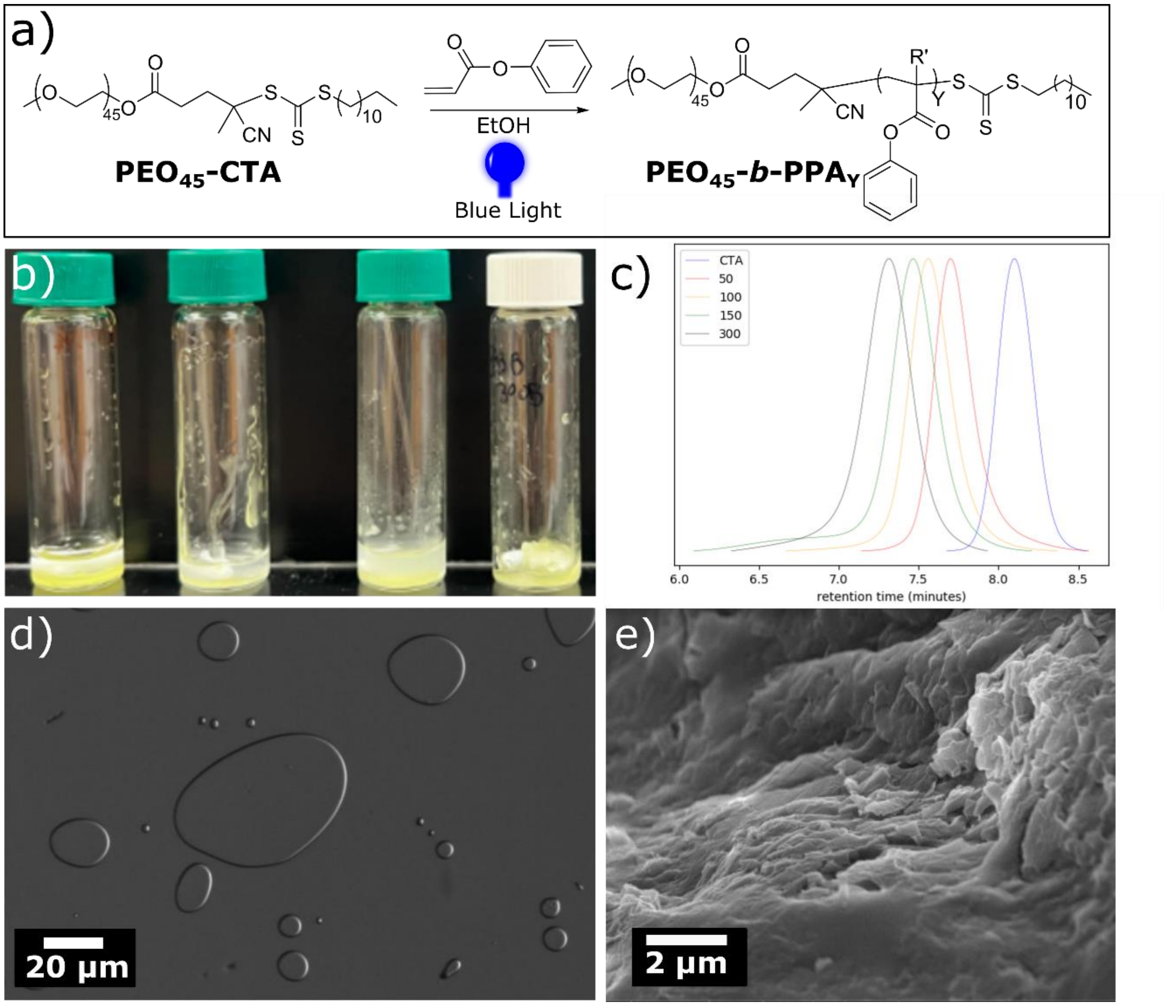

Figure 4.1: Polymerization scheme and characterizations. a) Blue light-mediated RAFT polymerization of polyethylene glycol-*block*-poly(phenyl acrylate) (PEO_{45}-*b*-PPA_y) in ethanol. b) Photograph of the final products of the polymerization in ethanol with varying target degrees of polymerizations DP 50, 100, 150, and 300. c) Size exclusion chromatography of the respective polymers and the macro-CTA. d) Bright field optical microscopy image of PEO_{45}-*b*-PPA_{20} condensates. e) Scanning electron micrograph of PEO_{45}-*b*-PPA_{300} gel showcasing textured gel surface.

In recent studies, we have established the criteria for block copolymers to form stable condensates,[22,23] in which one of the main criteria is the weak amphiphilicity of block copolymers in a given solution. Previously we modulated the amphiphilicity by adjusting the solvent composition. This was done by adding a selective solvent (water) into the dissolved polymer solution, at a critical water concentration the block copolymer enters weak amphiphilicity and undergoes LLPS to form stable condensates.[23] With this in mind we imagined a system in which the amphiphilicity of the polymer slowly evolves as the polymerization proceeds. Polymerization of PEO-*b*-PPA shows exactly this behavior as highlighted in Figure 4.1. Each polymerization was set up in a separate vial with varying target DP (Figure 4.1b). The outcome of each reaction was evaluated first visually, to detect droplet or gel formation. The monomer conversion was determined using ^{1}H NMR by comparing the vinylic protons of the monomer to the aromatic protons in the polymer for each reaction. We observed high monomer conversion >85% and low molecular weight dispersity (Đ <1.26, Figure 4.1c) for all target DPs and reached PPA chain lengths of up to 300 units.

In our system, the onset of LLPS (Figure 4.1d) is observed as the degree of polymerization approaches as low as 10 units forming PEO_{45}-PPA_{10}. Furthermore, as the PPA block grows, the droplets turn into gel-like particles. The onset of gelation is observed as the PPA block approaches a chain length of roughly 25 units. At DP >50 the gels become stiff and stick to the reaction vial. Scanning electron microscopy showed textured surfaces of the gel formed as seen in Figure1e.

The gels being formed in this system are different compared to the gels reported in other PISA systems.[21,24] Typically in PISA, as the block copolymers are polymerized they start to assemble into nanoscale structures, like spheres, vesicles, and worms.[24] Most PISA based gels appear when worm morphologies are formed during the PISA process. The long anisotropic worm structures are known to entangle and form supramolecular crosslinks creating gels.[25] In our system, as the polymerization proceeds the block copolymers first undergo condensation to form dense polymer rich droplets which further convert into gel-like solids as the polymerization continues. We suspect the gels here form due to entanglement and non-covalent crosslinks of block copolymers within the droplet phase, which increases as the polymers get longer. The nanoscale structure of the gel was characterized by TEM, and it revealed microphase separated domains as shown in Appendix C. Due to this unique mechanism, and the nanoscale structure the gels formed during PICON can be compared to the bulk block copolymer solids that show similar nanoscale features.[26,27]

Moving forward, we asked the question if the polymer droplets can encapsulate non-participating molecules in solution during the PICON process. To test this, we prepared samples by keeping the synthetic conditions the same and introducing a BODIPY based hydrophobic dye at 10 µM concentration into our system (Appendix C). The PICON synthesis was carried out with the PPA target DP of 100, and multiple reactions were set up for varying amounts of time (30, 60, and 90 minutes) to probe the evolution of partitioning. We tracked the partitioning of the fluorescent probe within the condensates using fluorescence microscopy as shown in Figure 2. The partition coefficients (K_p) which is the ratio of the dye concentration inside the condensate compared to the concentration in bulk solution was estimated by comparing the intensity of our fluorescent dye in the two phases following a previously reported protocol.[28] We observed that the K_p increases from 2.5 at 30 minutes when droplets are present (Figure 2a) to 7.3 at 90 minutes when the polymerization is completed resulting in gel-like solid particles (Figure 2c).

This observation can be explained by considering the hydrophobic interactions between the solvent, polymer, and the dye as the polymerization proceeds. At the beginning of the reaction, when no block copolymer is present, everything is dissolved. At this stage, the hydrophobic components in the system are dissolved monomer and the fluorophore. As the polymerization proceeds, the monomers react to produce the block copolymer, forming dense phase-separated droplets. At this stage, at least 75% of the initial monomer content remains unreacted. The droplets will be swollen by unreacted monomer, but we anticipate most of the monomer to be in the bulk solution at earlier stages, depleting more and more as the polymerization proceeds. As the monomer gets depleted in the bulk solution, most of the hydrophobic interactions will be present only within the condensates driving the uptake of the fluorophore within them. This is a proof of concept showcasing that simple hydrophobic interactions between the different components can be used to design PICON systems that can sequester small molecules. Further development of such systems will require detail on how the polymerization kinetics and the size of the molecules may affect encapsulation.

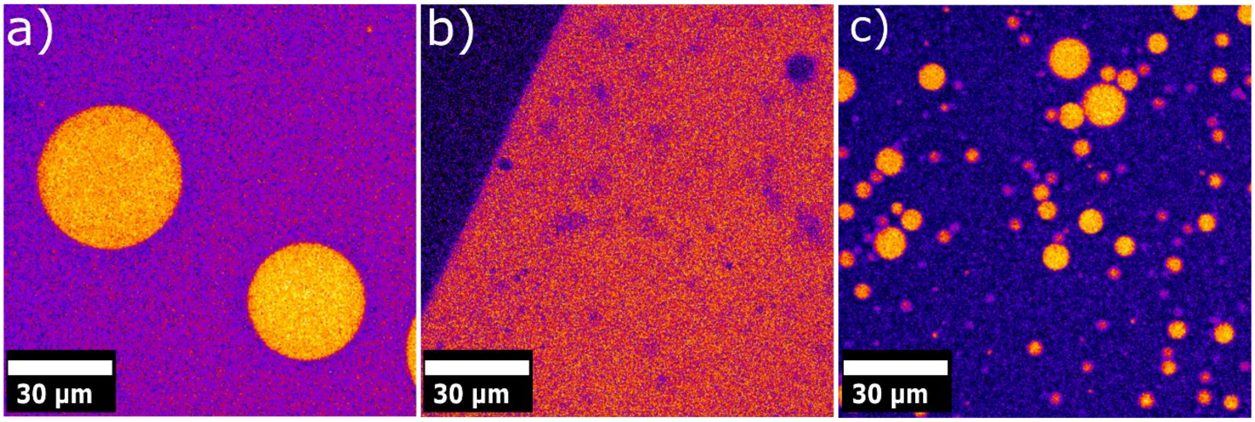

Figure 4.2: Partitioning of BODIPY-based fluorescent imaging agent during the PICON process. False-colored fluorescence microscopy images of samples at varying polymerization times a) 30 minutes, b) 60 minutes, and c) 90 minutes. These images

were used to calculate K_p at each timepoint which were 2.5, 6.0, and 7.3 min respectively. The polymerizations were prepared for a target PPA DP of 100.

Previous studies have shown that the onset of self-assembly usually results in a rate enhancement in PISA systems due to the increased local concentration of the growing polymer chains and the monomer. To explore our system further we first asked if the onset of condensate formation localizes the polymerization within them exclusively. As these droplets are in thermodynamic equilibrium with their surroundings it is possible that the reaction precursors, monomer, and macro-CTA are present in both phases at earlier stages of the polymerization, which can result in two distinct polymerization outcomes.[29] To test this, we set up a polymerization with a target PPA DP of 100. The polymerization was stopped after about 30 minutes when the solution became turbid, indicating droplet formation. The sample was transferred to an Eppendorf tube and centrifugation was used to separate out the two phases as shown

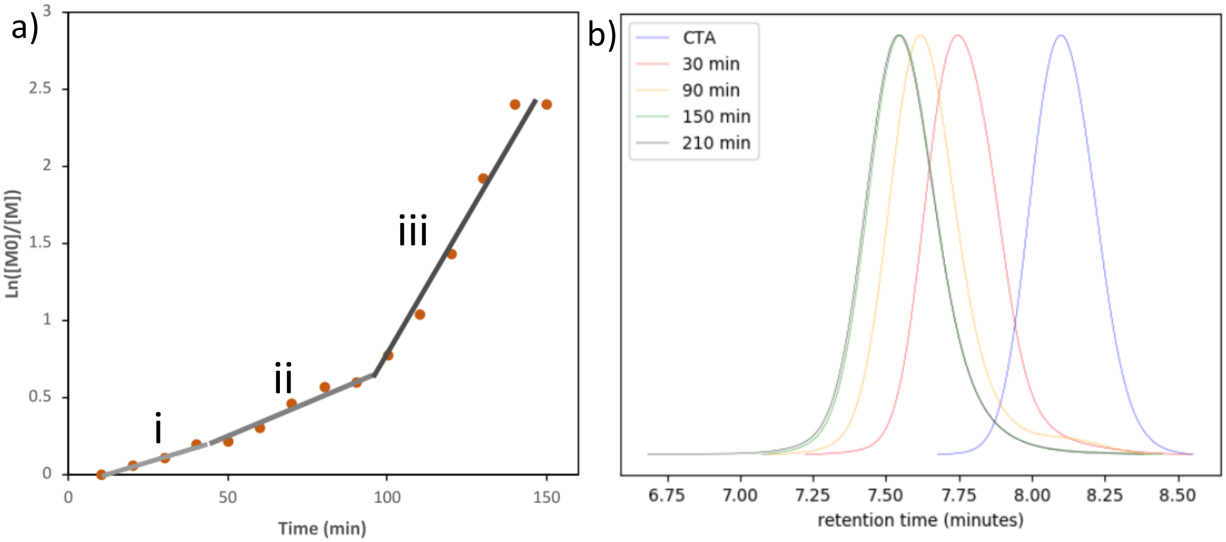

Figure 4.3: Polymerization kinetics of the PEO$_{45}$-b-PPA$_{100}$ at 30 wt%. a) Kinetics of monomer consumption plotted as a pseudo-first-order reaction kinetics. Region “I” represents the time in which no self-assembly or phase separation is observed. In region “ii” the apparent rate constant increases immediately after the solution has become turbid indicating the formation of coacervates. In region “iii” the apparent rate constant increases again after the condensates become more gel-like. b) Time-resolved SEC of the PEO$_{45}$-*b*-PPA$_{100.}$

in Appendix C. The contents of the two phases were characterized using ^{1}H NMR. The NMR spectra revealed that the CTA is only present in the dense condensate phase. These data provide evidence that polymerization only occurs within the condensates after their formation, as the RAFT macro-CTA is required for the polymerization to proceed. Having established this, we explored how the rate of polymerization was influenced by the phase behavior of our system. A polymerization with the target PPA DP of 100 was prepared and the monomer conversion was tracked in 10-minute intervals using ^{1}H NMR. The resulting data were used to model the polymerization kinetics to a pseudo-first-order reaction, based on previous reports.[30] We observed two increases in the apparent rate constant of propagation (k_{app}) as shown in Figure 3a. The k_{app} in region **i** was 7.5x10^{-5} s^{-1}, in region **ii** was 1.5x10^{-4} s^{-1}, and in region **iii** was 6.9x10^{-4} s^{-1}. The first increase in k_{app} occurred around 30-40 minutes (region i -> ii) and the second k_{app} increase happened around 90-100 minutes (region ii -> iii), the two changes in k_{app} signify the condensate formation and gel formation respectively. Only 2x increase in k_{app} (7.5x10^{-5} s^{-1} to 1.5x10^{-4} s^{-1}) is observed upon droplet formation, while the k_{app} increases almost 5 fold (1.5x10^{-4} s^{-1} to 6.9x10^{-4} s^{-1}) upon gel formation. The increase in the polymerization kinetics as condensates is due to the increased local monomer concentration. However, at this stage the droplets are highly solvated so the change in k_{app} is minimal. As the droplets turn more gel-like we see a much more significant increase in $k_{\text{app.}}$ This is likely because the gels start to behave like bulk polymer and the reaction kinetics rapidly increase due to the large jump in local monomer concentration. Furthermore, as the polymerization proceeds through the multiple phase changes, we observe good molecular weight control indicated by Đ<1.2 for all time points shown in Figure 3b.

4.3 Conclusion

In conclusion, we have developed a new way to access synthetic condensates in a way that mimics biological condensate formation. The inspiration and methodology were adapted from the decades of work in the field of polymerization-induced self-assembly. Condensate formation is not only important for model biomimetic systems but also for the synthesis of ordered materials, as many recent reports have shown condensates to be precursors to hierarchical self-assembled materials.[22,31] Our developed PICON system uses blue-light-initiated RAFT polymerization to prepare block copolymers that undergo LLPS to form condensates and subsequent gelation, which is fundamentally different from gelation of other PISA systems. Furthermore, we demonstrated that this process can also be used to sequester small molecules within the condensate based on intramolecular interactions. Lastly, we studied the reaction kinetics of polymerization noticing a slight increase in k_{app} upon condensation and a significant increase upon gelation. As PICON garners more interest, we anticipate these findings will help better understand polymerizing systems which undergo LLPS to form condensates.

4.4 References

(1) Hyman, A. A.; Weber, C. A.; Jülicher, F. Liquid-Liquid Phase Separation in Biology. *Annual Review of Cell and Developmental Biology* **2014**, *30* (1), 39–58. https://doi.org/10.1146/annurev-cellbio-100913-013325.

(2) *Flory, F. 1953 Principles Of Polymer Chemistry*.

(3) Lloyd, D. R.; Kim, S. S.; Kinzer, K. E. Microporous Membrane Formation via Thermally-Induced Phase Separation. II. Liquid—Liquid Phase Separation. *Journal of Membrane Science* **1991**, *64* (1), 1–11. https://doi.org/10.1016/0376-7388(91)80073-F.

(4) Abbas, M.; Lipiński, W. P.; Wang, J.; Spruijt, E. Peptide-Based Coacervates as Biomimetic Protocells. *Chem. Soc. Rev.* **2021**, *50* (6), 3690–3705. https://doi.org/10.1039/D0CS00307G.

(5) Cui, M.; Wang, X.; An, B.; Zhang, C.; Gui, X.; Li, K.; Li, Y.; Ge, P.; Zhang, J.; Liu, C.; Zhong, C. Exploiting Mammalian Low-Complexity Domains for Liquid-Liquid Phase Separation–Driven Underwater Adhesive Coatings. *Science Advances* **2019**, *5* (8), eaax3155. https://doi.org/10.1126/sciadv.aax3155.

(6) Marras, A. E.; Vieregg, J. R.; Ting, J. M.; Rubien, J. D.; Tirrell, M. V. Polyelectrolyte Complexation of Oligonucleotides by Charged Hydrophobic—Neutral Hydrophilic Block Copolymers. *Polymers* **2019**, *11* (1), 83. https://doi.org/10.3390/polym11010083.

(7) Lu, J.; Qian, J.; Xu, Z.; Yin, S.; Zhou, L.; Zheng, S.; Zhang, W. Emerging Roles of Liquid–Liquid Phase Separation in Cancer: From Protein Aggregation to Immune-Associated Signaling. *Frontiers in Cell and Developmental Biology* **2021**, *9*.

(8) Zhu, L.; Richardson, T. M.; Wacheul, L.; Wei, M.-T.; Feric, M.; Whitney, G.; Lafontaine, D. L. J.; Brangwynne, C. P. Controlling the Material Properties and RRNA Processing Function of the Nucleolus Using Light. *Proceedings of the National Academy of Sciences* **2019**, *116* (35), 17330–17335. https://doi.org/10.1073/pnas.1903870116.

(9) Sanulli, S.; Trnka, M. J.; Dharmarajan, V.; Tibble, R. W.; Pascal, B. D.; Burlingame, A. L.; Griffin, P. R.; Gross, J. D.; Narlikar, G. J. HP1 Reshapes Nucleosome Core to Promote Phase Separation of Heterochromatin. *Nature* **2019**, *575* (7782), 390–394. https://doi.org/10.1038/s41586-019-1669-2.

(10) Deng, J.; Walther, A. Programmable ATP-Fueled DNA Coacervates by Transient Liquid-Liquid Phase Separation. *Chem* **2020**, *6* (12), 3329–3343. https://doi.org/10.1016/j.chempr.2020.09.022.

(11) Donau, C.; Späth, F.; Sosson, M.; Kriebisch, B.; Schnitter, F.; Tena-Solsona, M.; Kang, H.-S.; Salibi, E.; Sattler, M.; Mutschler, H.; Boekhoven, J. *Active Coacervate Droplets as a Model for Membraneless Organelles and a Platform Towards Synthetic Life*; preprint; 2020. https://doi.org/10.26434/chemrxiv.11648598.v1.

(12) Penfold, N. J. W.; Yeow, J.; Boyer, C.; Armes, S. P. Emerging Trends in Polymerization-Induced Self-Assembly. *ACS Macro Lett.* **2019**, *8* (8), 1029–1054. https://doi.org/10.1021/acsmacrolett.9b00464.

(13) Yeow, J.; Boyer, C. Photoinitiated Polymerization-Induced Self-Assembly (Photo-PISA): New Insights and Opportunities. *Advanced Science* **2017**, *4* (7), 1700137. https://doi.org/10.1002/advs.201700137.
(14) Jiang, Y.; Xu, N.; Han, J.; Yu, Q.; Guo, L.; Gao, P.; Lu, X.; Cai, Y. The Direct Synthesis of Interface-Decorated Reactive Block Copolymer Nanoparticles via Polymerisation-Induced Self-Assembly. *Polym. Chem.* **2015**, *6* (27), 4955–4965. https://doi.org/10.1039/C5PY00656B.
(15) Tan, J.; Huang, C.; Liu, D.; Zhang, X.; Bai, Y.; Zhang, L. Alcoholic Photoinitiated Polymerization-Induced Self-Assembly (Photo-PISA): A Fast Route toward Poly(Isobornyl Acrylate)-Based Diblock Copolymer Nano-Objects. *ACS Macro Lett.* **2016**, *5* (8), 894–899. https://doi.org/10.1021/acsmacrolett.6b00439.
(16) Canning, S. L.; Smith, G. N.; Armes, S. P. A Critical Appraisal of RAFT-Mediated Polymerization-Induced Self-Assembly. *Macromolecules* **2016**, *49* (6), 1985–2001. https://doi.org/10.1021/acs.macromol.5b02602.
(17) Ma, L.; Xiong, W.; Yu, K.; Wang, X.; Cao, Y.; Lu, X.; Cai, Y. Liquid-Phase Condensation via Macromolecular Crowding in Polymerization-Induced Electrostatic Self-Assembly. *ACS Macro Lett.* **2021**, *10* (11), 1410–1415. https://doi.org/10.1021/acsmacrolett.1c00557.
(18) Wang, Y.; Li, C.; Ma, L.; Wang, X.; Wang, K.; Lu, X.; Cai, Y. Interfacial Liquid–Liquid Phase Separation-Driven Polymerization-Induced Electrostatic Self-Assembly. *Macromolecules* **2021**, *54* (12), 5577–5585. https://doi.org/10.1021/acs.macromol.1c00756.
(19) Keddie, D. J. A Guide to the Synthesis of Block Copolymers Using Reversible-Addition Fragmentation Chain Transfer (RAFT) Polymerization. *Chem. Soc. Rev.* **2013**, *43* (2), 496–505. https://doi.org/10.1039/C3CS60290G.
(20) Wan, J.; Fan, B.; H. Thang, S. RAFT-Mediated Polymerization-Induced Self-Assembly (RAFT-PISA): Current Status and Future Directions. *Chemical Science* **2022**, *13* (15), 4192–4224. https://doi.org/10.1039/D2SC00762B.
(21) L. Canning, S.; J. Cunningham, V.; D. Ratcliffe, L. P.; P. Armes, S. Phenyl Acrylate Is a Versatile Monomer for the Synthesis of Acrylic Diblock Copolymer Nano-Objects via Polymerization-Induced Self-Assembly. *Polymer Chemistry* **2017**, *8* (33), 4811–4821. https://doi.org/10.1039/C7PY01161J.
(22) Ianiro, A.; Wu, H.; Rijt, M. M. J. van; Vena, M. P.; Keizer, A. D. A.; Esteves, A. C. C.; Tuinier, R.; Friedrich, H.; Sommerdijk, N. A. J. M.; Patterson, J. P. Liquid–Liquid Phase Separation during Amphiphilic Self-Assembly. *Nat. Chem.* **2019**, *11* (4), 320–328. https://doi.org/10.1038/s41557-019-0210-4.
(23) Rizvi, A.; Patel, U.; Ianiro, A.; Hurst, P. J.; Merham, J. G.; Patterson, J. P. Nonionic Block Copolymer Coacervates. *Macromolecules* **2020**, *53* (14), 6078–6086. https://doi.org/10.1021/acs.macromol.0c00979.
(24) Blanazs, A.; Verber, R.; Mykhaylyk, O. O.; Ryan, A. J.; Heath, J. Z.; Douglas, C. W. I.; Armes, S. P. Sterilizable Gels from Thermoresponsive Block Copolymer Worms. *J. Am. Chem. Soc.* **2012**, *134* (23), 9741–9748. https://doi.org/10.1021/ja3024059.

(25) Won, Y.-Y.; Davis, H. T.; Bates, F. S. Giant Wormlike Rubber Micelles. *Science* **1999**, *283* (5404), 960–963. https://doi.org/10.1126/science.283.5404.960.
(26) Battaglia, G.; Ryan, A. J. The Evolution of Vesicles from Bulk Lamellar Gels. *Nature Mater* **2005**, *4* (11), 869–876. https://doi.org/10.1038/nmat1501.
(27) Schacher, F. H.; Rupar, P. A.; Manners, I. Functional Block Copolymers: Nanostructured Materials with Emerging Applications. *Angewandte Chemie International Edition* **2012**, *51* (32), 7898–7921. https://doi.org/10.1002/anie.201200310.
(28) Nguyen, D. T.; Jeon, B.; Abraham, G. R.; Saleh, O. A. Length-Dependence and Spatial Structure of DNA Partitioning into a DNA Liquid. *Langmuir* **2019**, *35* (46), 14849–14854. https://doi.org/10.1021/acs.langmuir.9b02098.
(29) Tan, J.; Dai, X.; Zhang, Y.; Yu, L.; Sun, H.; Zhang, L. Photoinitiated Polymerization-Induced Self-Assembly via Visible Light-Induced RAFT-Mediated Emulsion Polymerization. *ACS Macro Lett.* **2019**, *8* (2), 205–212. https://doi.org/10.1021/acsmacrolett.9b00007.
(30) Blackman, L. D.; Doncom, K. E. B.; Gibson, M. I.; O'Reilly, R. K. Comparison of Photo- and Thermally Initiated Polymerization-Induced Self-Assembly: A Lack of End Group Fidelity Drives the Formation of Higher Order Morphologies. *Polym. Chem.* **2017**, *8* (18), 2860–2871. https://doi.org/10.1039/C7PY00407A.
(31) Yuan, C.; Levin, A.; Chen, W.; Xing, R.; Zou, Q.; Herling, T. W.; Challa, P. K.; Knowles, T. P. J.; Yan, X. Nucleation and Growth of Amino Acid and Peptide Supramolecular Polymers through Liquid–Liquid Phase Separation. *Angewandte Chemie International Edition* **2019**, *58* (50), 18116–18123. https://doi.org/10.1002/anie.201911782.

Appendix C: Supplementary information for Chapter 4

C.1 Materials and instruments:

All reagents were purchased from Acros Organics, Fisher Scientific, or Sigma-Aldrich, and used without further purification unless otherwise noted. ^{1}H NMR spectra were collected on a 500 MHz Bruker Avance spectrometer. All samples were taken in CD_2Cl_2. All TEM experiments were performed on a JEOL 2100 equipped with a 200 keV field emission gun and a OneView camera, Irvine Materials Research Institute, University of California, Irvine. CryoTEM Quantifoil Holey Carbon Films were purchased from Electron Microscopy Sciences, grids were glow discharged for 70 s to increase hydrophilicity prior to sample preparation. Fluorescence imaging was performed with a MicroTime 200 (PicoQuant, Germany), an IX83 inverted microscope (Olympus Corp.), and a 100×, 1.45 NA oil-immersion objective UPLSAPO Plan Apochromat (Olympus Corp.). Size exclusion chromatography (SEC) was performed in THF using an Agilent 1100 chromatograph equipped with RID detector and a PL gel 5 μm 300x7.5 mm mixed column. All samples were calibrated against polystyrene standards (MW= 580, 1300, 5000, 10000, 30000, 70000, 130000 g/mol).

C.2 Experimental Methods

Synthesis of polyethylene glycol-*block*-poly phenyl acrylate.

In a vial with a septum cap, PEO-CTA was measured out along with the phenyl acrylate monomer. The ratios were determined based on the desired target degree of polymerization (Table D1). This was followed by the addition of EtOH which was determined by the desired wt% (Monomer+CTA/(Monomer+CTA+Solvent). For this study, each reaction was carried out at 30 wt% solids unless otherwise specified. Once the reaction mixture was completely dissolved, N_2 was purged for 15 minutes to eliminate any dissolved O_2. The reaction was then initiated by placing it in our reaction set up as shown in figure D.1. The reactions were stopped by turning of the lamps after 5h our irradiation unless otherwise specified. The monomer conversion was determined by comparing the vinyl peaks or doing end group analysis using the CTA end group (0.88 ppm) Figure D.2. Size exclusion chromatography was performed with THF as the eluent.

Table D1. Quantities of reagents used for different PICON experiments.

PPA target DP	CTA (mg)	PPA (mg)	EtOH (mL)
20	40	63	0.25
50	40	125	0.5
100	40	250	0.9
300	40	750	2.6

Reaction kinetics of the PICON process.

The reaction was carried out as mentioned above. To monitor monomer conversion, the sample was irradiated at different time intervals, aliquotting samples in between for ^{1}H NMR analysis. The consumption of monomer was estimated by following the chain extension via end group analysis. This was done instead of comparing monomer peaks to avoid any error due to the distinct ratios of monomer present in the dense phase compared to the dilute phase. Since polymerization only occurs in the dense phase, we can be confident of the conversion based on the chain-growth. The resulting data was plotted as pseudo-first-order reaction kinetics.

C.3 Supplementary Figures

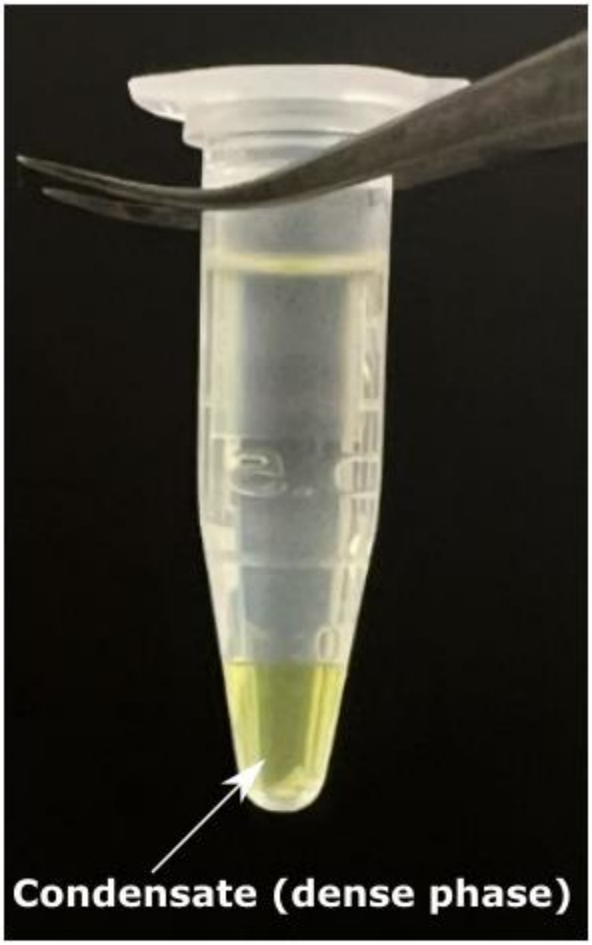

Figure D.1: Photograph of a macrophase separated PICON reaction. The arrow points to the dense condensate phase in which the polymerization proceeds.

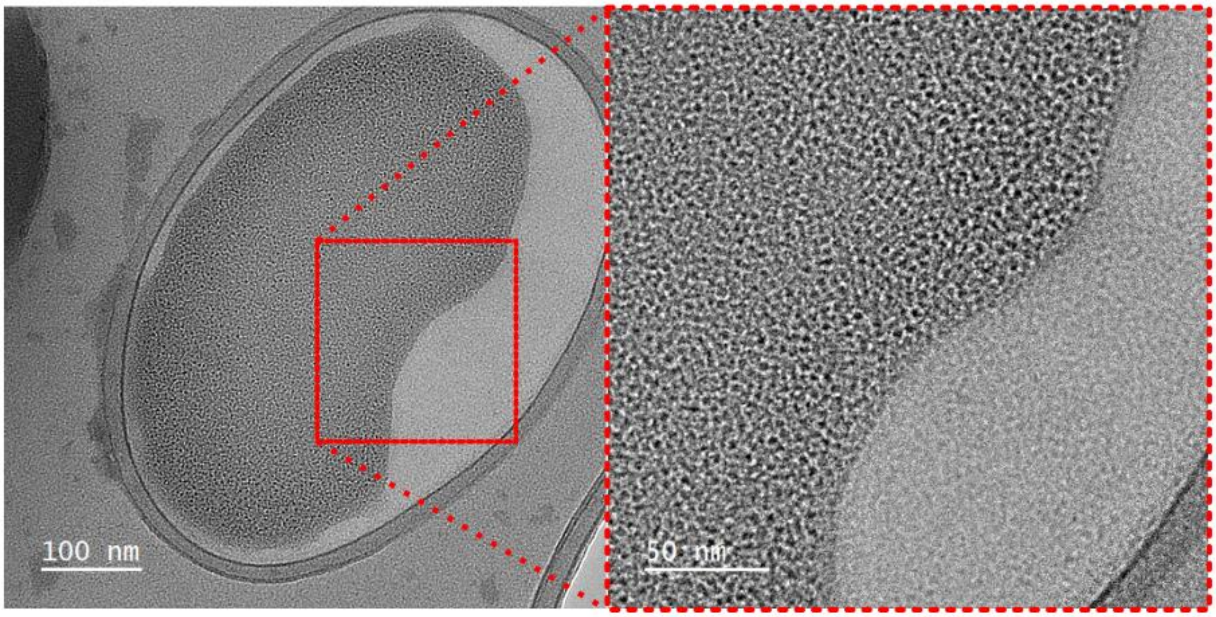

Figure D.2: TEM image of exfoliated PEO$_{45}$-*b*-PPA$_{300}$ gel. Close up of the image clearly shows a microphase separated morphology similar to the ones found in bulk block copolymer systems.

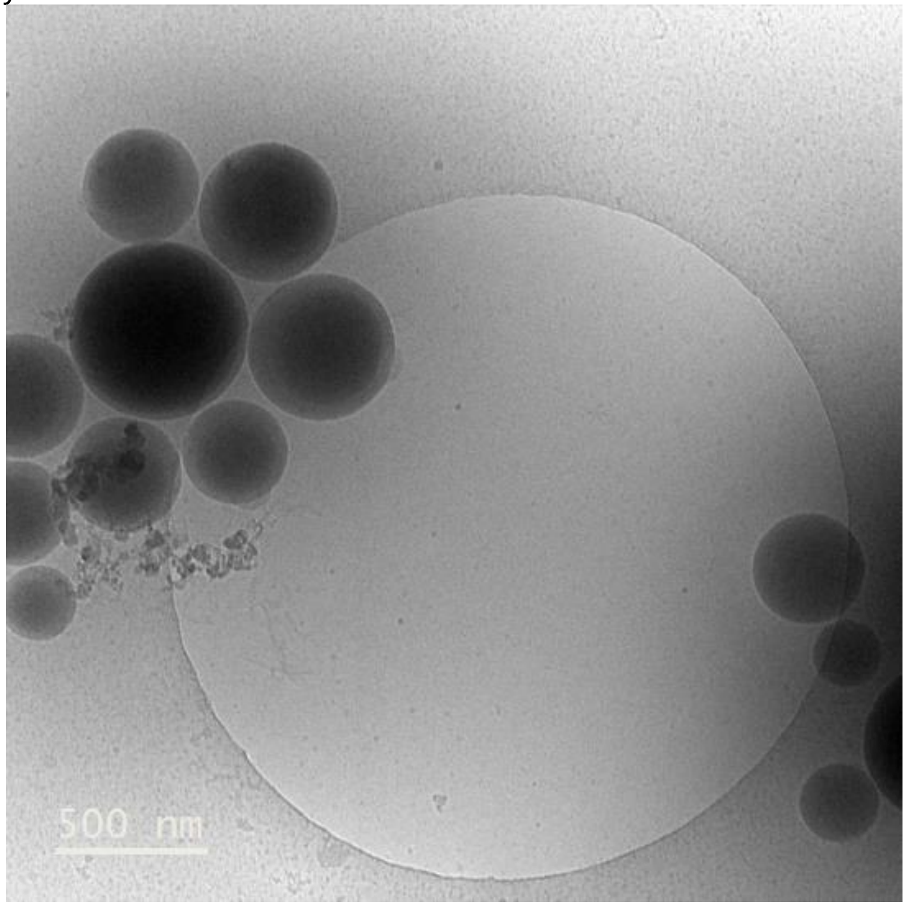

Figure D.3: Cryo-TEM image of spherical particles formed of PEO$_{45}$-*b*-PPA$_{100}$.

Chapter 5: Observation of liquid-liquid phase separation and vesicle spreading during supported bilayer formation via liquid phase transmission electron microscopy.

This Chapter was adapted from a published article (**Aoon Rizvi**, Justin Mulvey, Joseph P Patterson. “Observation of Liquid–Liquid-Phase Separation and Vesicle Spreading during Supported Bilayer Formation via Liquid-Phase Transmission Electron Microscopy.” *Nano Lett. 2021, 21, 24, 10325–10332*)

5.1 INTRODUCTION:

Liquid phase transmission electron microscopy (LP-TEM) has transformed the analysis of nanomaterials by enabling the direct real-time visualization of material formation and transformation in solution with nanometer spatial resolution.[1–9] Over the last decade, the use of LP-TEM has enabled the discovery of new formation mechanisms for inorganic nanomaterials,[10] soft-matter,[3] and biological assemblies[4]. For example, loop intermediates during DNA double helix formation,[11] the interfacial driven coupling of nucleation and particle attachment,[12] the fusion and fission of block copolymer micelles,[13,14] and the phenomena of liquid-liquid phase separation during amphiphilic self-assembly.[15] These breakthroughs highlight the power of LP-TEM to discover new phenomenon in material formation, even in systems that have been studied for decades.[16] LP-TEM is most commonly performed in silicon nitride or graphene liquid cells,[16] which provides an ideal opportunity to study the interactions between matter and solid substrates.

Supported bilayers (SB) are materials made of amphiphilic molecules such as lipids and block copolymers, held together by non-covalent interactions with a substrate.[17–22] SB display diverse physical and chemical properties and have been used to study membrane properties such as ligand-receptor interactions,[23,24] viral attacks,[25] and cellular signaling.[26] Furthermore, SB enable surface sensitive measurements, such as acoustic,[27] optical,[28] plasmonic, and chemical sensing.[29] Block copolymers have proven to be an interesting alternative to lipids as they are more mechanically robust, chemically diverse, stable to dehydration/rehydration,[21] and show more flexible chain dynamics.[30,31] Generally, SB are prepared by either vesicle spreading,[32–37] or the more recent solvent assisted bilayer formation method pioneered by Nam-Joon Cho and coworkers.[38–41] Using this method they have shown that supported bilayers can be formed with surfaces and morphologies which are typically inaccessible using the vesicle spreading method.[40,41] In the vesicle spreading method, a solution of preformed vesicles is exposed to a solid support. The vesicles adhere, rupture, and spread over the surface to form supported bilayers.[42] In the solvent assisted method, the amphiphiles are initially dissolved in a good solvent and a selective solvent is introduced to initiate the self-assembly of the amphiphiles into supported bilayers.[43] The mechanism of this process is unclear, however, it is thought that the amphiphiles first form micelles/vesicles which adhere to the surface and spread to form the bilayers. This formation method is unexplored regarding block copolymer SB fabrication.

The visualization of bilayer formation is challenging due to the difficulty of imaging nanoscale dynamics in a liquid environment. Previously, Richter et al. used a combination of quartz crystal microbalance and atomic force microscopy to study SB formation with charged lipids.[44] They discovered that during bilayer formation the vesicles adhere onto the substrate and rupture in a wave fashion due to the "active edge" effect. They also determined that fusion between vesicle did not take place and bilayer formation was mainly due to the rupture of vesicles.[44] In a later study, Israelachvili and co-workers also observed the "active edge" effect when studying SB formation using fluorescence microscopy.[45] Furthermore, Andrecka et al. studied SB formation using interferometric scattering microscopy,[46] where they introduced 100 nm vesicles on to a glass surface and the bilayer formation was imaged using 25 frames per second. The vesicles appeared as diffraction-limited spots which covered the viewing area and slowly transformed into bright patches, indicating vesicle rupture and SB formation. However, the spatial resolution was insufficient to visualize the membrane structure while the vesicles transitioned to a supported bilayer. Here, we demonstrate LP-TEM as a high resolution, in-situ method for studying SB formation. The benefit of LP-TEM is that the high-resolution projection images enable membrane dynamics to be studied during SB formation.

5.2 RESULTS AND DISCUSSION

LP-TEM was performed with a liquid flow holder and silicon nitride chips with 50 μm X 200 μm electron transparent windows (see SI for more details, Figure S1). Polystyrene-block-poly acrylic (PS-*b*-PAA) was chosen for this study because it has been studied intensively using multiple TEM methods,[47–49] is a model system for amphiphilic block copolymers,[50,51] and PAA can bind to the free amine groups on the silicon nitride through electrostatic interactions.[52] Block copolymers are commonly self-assembled using solvent exchange methods in which the polymer is first dissolved in a solvent where both blocks are soluble (good solvent), and then a second solvent is added where only one of the blocks is soluble (selective solvent).[47] This is analogues to the solvent assisted method used to prepare supported bilayers.[53] The drop cast method was used to pre-load the liquid cell with a dissolved solution of PS-*b*-PAA in a mixture of THF:Dioxane, the good solvent (Figure S2, S3).[48] To initiate the bilayer formation a solvent exchange was performed during imaging by flowing in water, the selective solvent, into the silicon nitride cell using a syringe (See SI for more details). This method is beneficial as it enables slow exchange of the solvent, however it is limited in that the exact composition of the solvent in the imaging areas is unknown.[15,54]

One of the most important considerations for LP-TEM experiments is the influence of the electron beam during imaging.[3,55] All LP-TEM experiments were performed at dose rates within 11-15 $e^{-}/nm^{2}\cdot s$. Control experiments were performed where PS-*b*-PAA vesicles were prepared ex-situ, loaded into the liquid cell, and imaged for ≈700 seconds at a dose rate of 11 $e^{-}/nm^{2}\cdot s$, without performing the solvent exchange (i.e. water was not flown into the cell with a syringe). The purpose of the control experiments is to determine the effect of the electron beam on the polymer assemblies. Electron beam effects have been well studied in LP-TEM experiments and the dominant mechanisms are thought to be solvent radiolysis and charging.[16,56,57] It has been demonstrated the presence of organic solvents in water can reduce radiolysis.[56,58] Therefore, we performed control experiments with vesicles in a 1:1 organic solvent: water mixture and in pure water. The control experiments show that the electron beam does not cause the rupture, spreading, or fusion of vesicles as observed in the SB formation experiments. Interestingly, samples imaged in organic-water mixtures produced images with better feature resolution (see Figures S4, S5, S6, and SI for further discussion).

During the SB formation experiments we observed two formation pathways. In pathway 1 (Figure 5.1a) we observed SB formation via vesicle growth and spreading during the solvent exchange. No fusion events were observed indicating vesicle growth was due to unimer addition, which was followed by rupture and spreading to form bilayers. In pathway 2 (Figure 5.1b), we observed the solution undergo liquid-liquid phase separation to form liquid droplets. The droplets coalesce together and spread to form bilayers. As discussed later, we believe the two pathways occur as a result of different solvent environments where the droplet spreading mechanism is favored at lower water content.

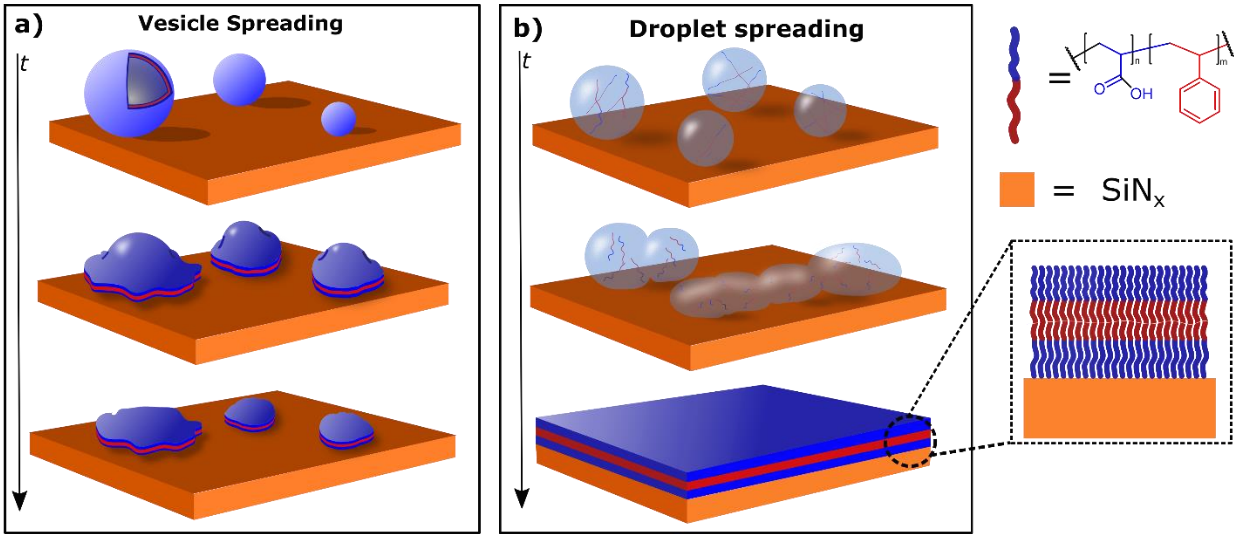

Figure 5.1: Schematic of the two pathways observed during bilayer formation. a) Vesicle spreading, the block copolymers were observed to form vesicles which grew, ruptured, and spread to form supported bilayers. b) Droplet spreading, the block copolymers were observed to undergo liquid-liquid phase separation to form droplets that spread over the surface to form supported bilayers.

Vesicle rupture and spreading

Vesicle rupture is the most accepted mechanism for SB formation.[32] The driving force for vesicle rupture is proposed to be the high curvature of the vesicles at the substrate-vesicle interface.[59] Additionally, it has been reported previously that rupture and spreading occurs through the widening of a pore and attachment of the outer membrane surface to the substrate.[59] The exposed edge is known to catalyze other vesicles to rupture due to the high energy conformation of lipids at the edge of a bilayer. This thermodynamically favors larger supported bilayers and makes smaller bilayers (diameter ≈ 300 nm) unstable.[59] Our LPTEM data (Figure 5.2 a, SI MOVIE 1), shows individual vesicles undergoing spreading and rupture. In this experiment we obtained a partially dry cell, which can be seen from the contrast gradient in the top left of the image series (Figure 2a).[60,61] The area and membrane contrast of 4 individual vesicles within the wet areas of the cell were quantified using image analysis (Figure 2 b, c, d). An in-house MATLAB script was developed to segment the vesicles across each frame in the dataset for quantitative analysis (See Figures S7, S8, S9 and SI for further discussion). The data shows that the larger vesicles (V1 and V2) grow much faster than the smaller vesicles (V3 and V4) (Figure 2 c). We have previously shown that for a vesicle growth mechanism, the ratio between the membrane contrast and the equivalent membrane diameter (C/D) in the TEM images should increase as the membrane diameter increases.[15] This is mainly due to the increase in polymer volume fraction within the membrane as the solvent exchange proceeds. However, despite the large area increase for V1 and V2, V1 shows a decrease in C/D, and V2 shows virtually no change in C/D. This indicates that the vesicles are undergoing spreading rather than growth. Consequently, we can quantify the vesicle spread rate as the change in area vs. time (Figure 5.2e). The data shows there is a decrease in the spread rate of V1 and V2 over the course of the experiment indicating the polymers are becoming kinetically trapped. V3 and V4 are much smaller and show an increase in C/D with increasing diameters indicating they are likely undergoing growth and spreading during data collection. All block copolymer bilayers (Figure 5.2a) were < 500 nm in equivalent diameter which is interesting because it has previously been shown that lipid bilayers and not stable in this size range.[62]

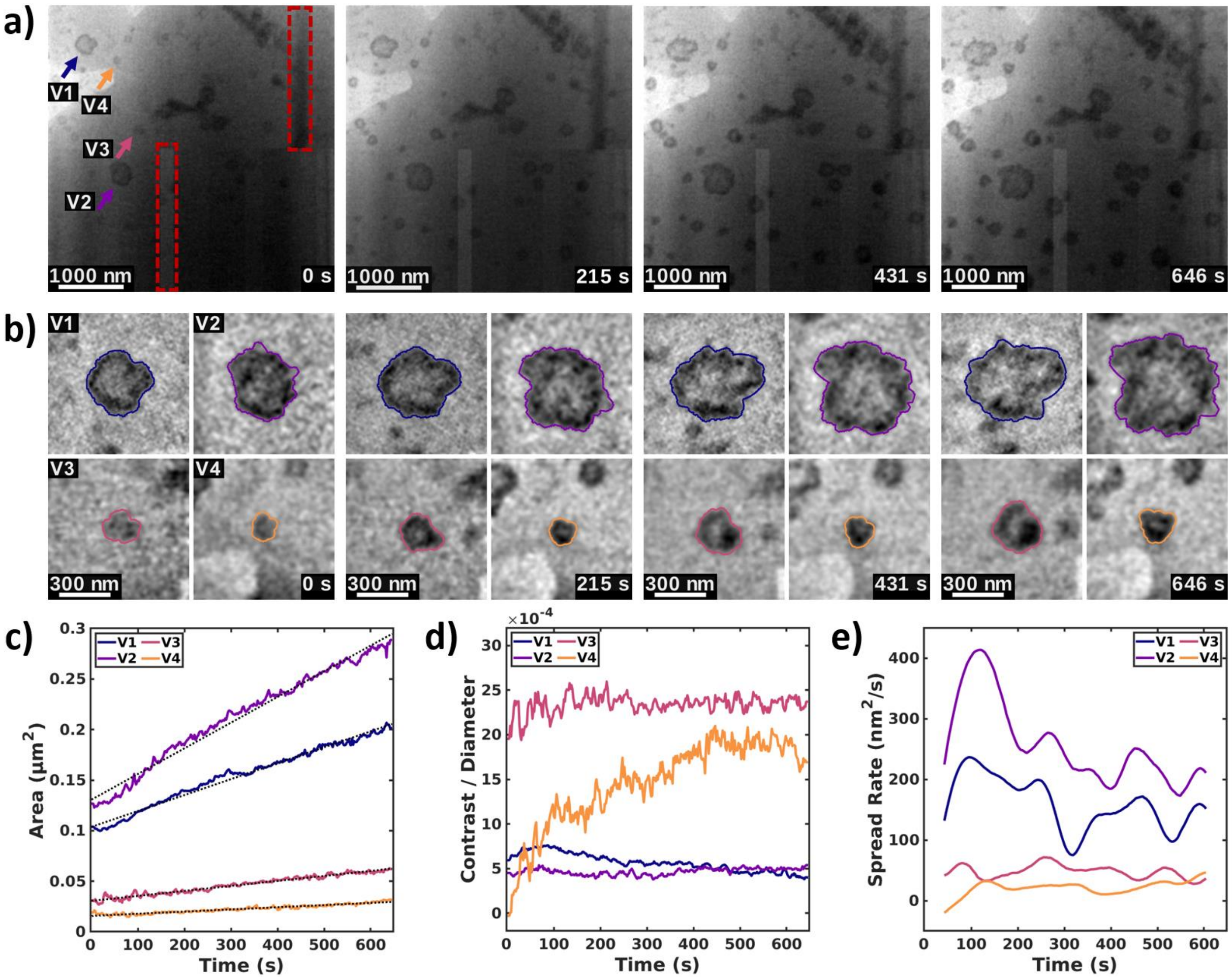

Figure 5.2: Vesicle spreading during bilayer formation. a) Time series of SI MOVIE 1, the colored arrows indicate each vesicle that was analyzed further, the red dashed box highlight detector artefacts. b) Time series of individual vesicles in SI MOVIE 1 (15 $e^-/nm^2 \cdot s$), colored outlines correspond to the arrows. c) The area evolution of each vesicle shown above. Dashed line indicates a linear fit. d) Ratio of average membrane contrast to membrane diameter (details in SI). e) The evolution of the spread rate for each vesicle shown above.

To interpret the membrane dynamics during rupture and spreading, a MATLAB script was developed to produce a time-resolved angular intensity map of the segmented membrane for V1 (Figure 5.3, Figure S10). The data shows the vesicle spreading anisotropically, and that multiple localized regions in the membrane begin to thin before eventually rupturing between 400 and 500 seconds (Figure 5.3b, c). Other regions appear to be more fixed to the substrate, and do not significantly change over time (Figure 3c). It has previously been shown that the surface chemistry and binding affinity dictates whether vesicles undergo intact adsorption or SB formation.[37,63] We believe our LP-TEM data is a direct visualization of why substrate attachment is required for vesicle spreading. When the solvent exchange process is performed in a vial (i.e. when the vesicles are not adhered to a surface), the size of the vesicles increases with increasing amount of water addition, as determined by dynamic light scattering (Figure S11).[48] However when the solvent exchange is performed and a vesicle is adhered to a surface at multiple locations, the size increase in these regions is hindered. This results in the formation of a supported bilayer through anisotropic swelling, rupture, and spreading. This mechanism has been previously discussed but not directly obsvered.[46,64]

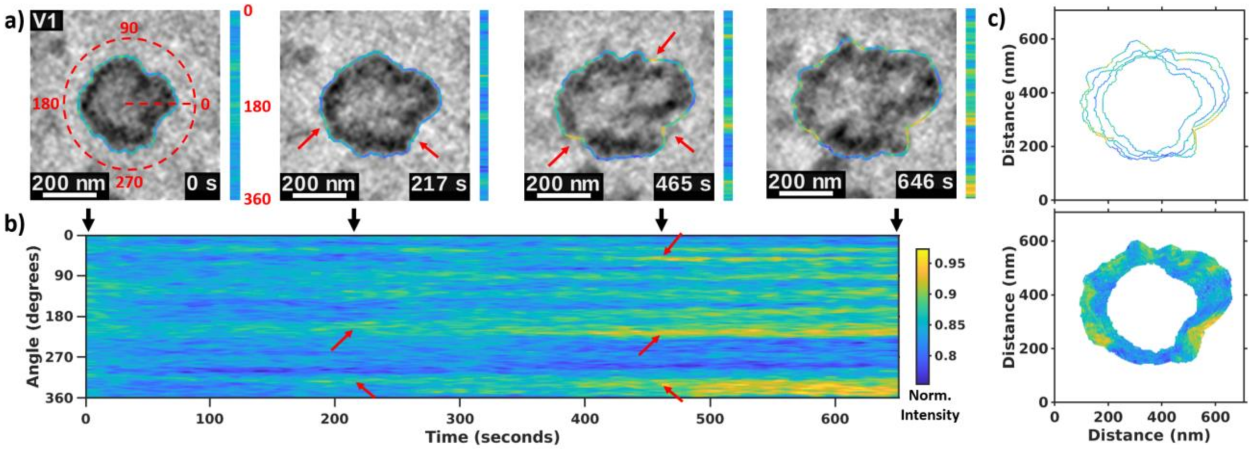

Figure 5.3: Membrane analysis of vesicle (V1). (a) Snapshots of the LP-TEM movie (SI MOVIE 1) during the solvent exchange process. The outline intensity shows the integrity of the membrane; high intensity of detected electron means the membrane has been ruptured in that area. b) Angular intensity map of the vesicle pictured above (more details in SI). The red arrows correspond to the individual areas in the vesicle membrane where the rupture was observed. c) Overlayed particle outlines for selected frame (top) and all frames (bottom).

Droplet formation and spreading

In pathway 2 (Figure 4a, SI MOVIE 2) we observe the liquid-liquid phase separation (also known as coacervation) and the formation of droplets that diffuse across the surface, coalesce, and then spread to cover the surface. The resulting SB shows 99.8% surface coverage (Figure S13) and shows minimal nanoscale defects. We interpret the early-stage structures as liquid droplets based upon their dynamic motion during fusion. Coacervate droplets are typically thought to be membraneless and their spreading and fusion dynamics have been less studied compared to vesicles.[65] In this dataset, droplets fuse together within a few seconds, which is much quicker than what is expected for block copolymer nanoparticles.[13,66] Based on control experiments we believe that liquid-liquid phase separation occurs at ~10% water content (Figure S12). Previously reported, we have shown nonionic BCP can form coacervates (stable droplets) in organic water mixtures, slight variations in the water composition may shift the favored phase into the self-assembled phase.[54] The droplet formation in the LP-TEM experiment suggests that the solvent exchange rate was slow enough that the polymers are not kinetically arrested in the early stages of SB formation. Due to the fact that the liquid-liquid phase separation does not favor stable nanodroplets we were unable to perform the same electron dose control experiment. However, as the organic solvent content is higher for droplets than for vesicles, we believe that the vesicle control is valid as a guide for the droplet experiments (see supporting for more info).

The data shows that droplet fusion and spreading can either lead to homogenous bilayers (Figure 4 a, b, blue region) or regions with defects (Figure 4a, c, red region). To better visualize the droplet fusion dynamics and defect formation, cross-sectional time series plots were created for both the red and blue regions (Figure 4b and c). The analysis of the blue region shows that fusion between the two droplets had already started before the droplets appeared in the viewing area of the cell ($t < 1576$ seconds). The higher contrast at the droplet interface indicates a higher polymer concentration and different polymer organization at the interface. In our previous studies we have performed SCF simulation studies on similar di-block copolymer systems which show a direct relationship between polymer concentration and contrast.[15] Over time, the polymer density at the interface decreases, and the resulting supported bilayer region becomes homogeneous ($t > 2000$ seconds). The analysis of the red region shows droplet fusion occurs later in the dataset ($t > 1800$ seconds) and produces a dense region at the interface, which we interpret as a defect in the bilayer. This is likely due to the kinetically limited reorganization of polymers at droplet interface, which we have previously observed during the formation of block copolymer vesicles.[15] However, the observations here indicate that premature organization at the droplet interface leads to defect formation in the final SB structure (Figure 4c).

These observed differences are likely due to local differences in solution composition or polymer organization during the early stages of droplet formation. We have shown previously that slight variations in the selective solvent (water in this case) can alter the preferred phase of block copolymers, in our recent study we demonstrated that as low as 2 wt% water difference can shift the polymer solution from a coacervate phase (droplet phase) to a solid self-assembled phase.[54] Once these boundaries are known for a given polymer it is possible to design the solvent exchange experiments to stabilize the droplets and use them to control both the size and morphology of the self-assembled polymers.[54] In a previous study Tabaei et al. reported that during the solvent assisted method the identity of the organic solvent can have a large effect on the quality of supported bilayers formed.[38] Although not mentioned in their studies we suspect a similar droplet mechanism at play in which one of the solvent compositions favors droplet formation resulting in pristine supported bilayers. Furthermore, an interesting feature of the droplet spreading mechanism is that the "active edge effect" is not required to from pristine bilayers and bilayer formation (micro phase separation between the blocks) can occur after the droplets have spread. Our observations make it clear that liquid-precursors are important to form defect free supported bilayers when using the solvent assisted method and more work is required to further understand and utilize liquid precursors during bilayer formation.

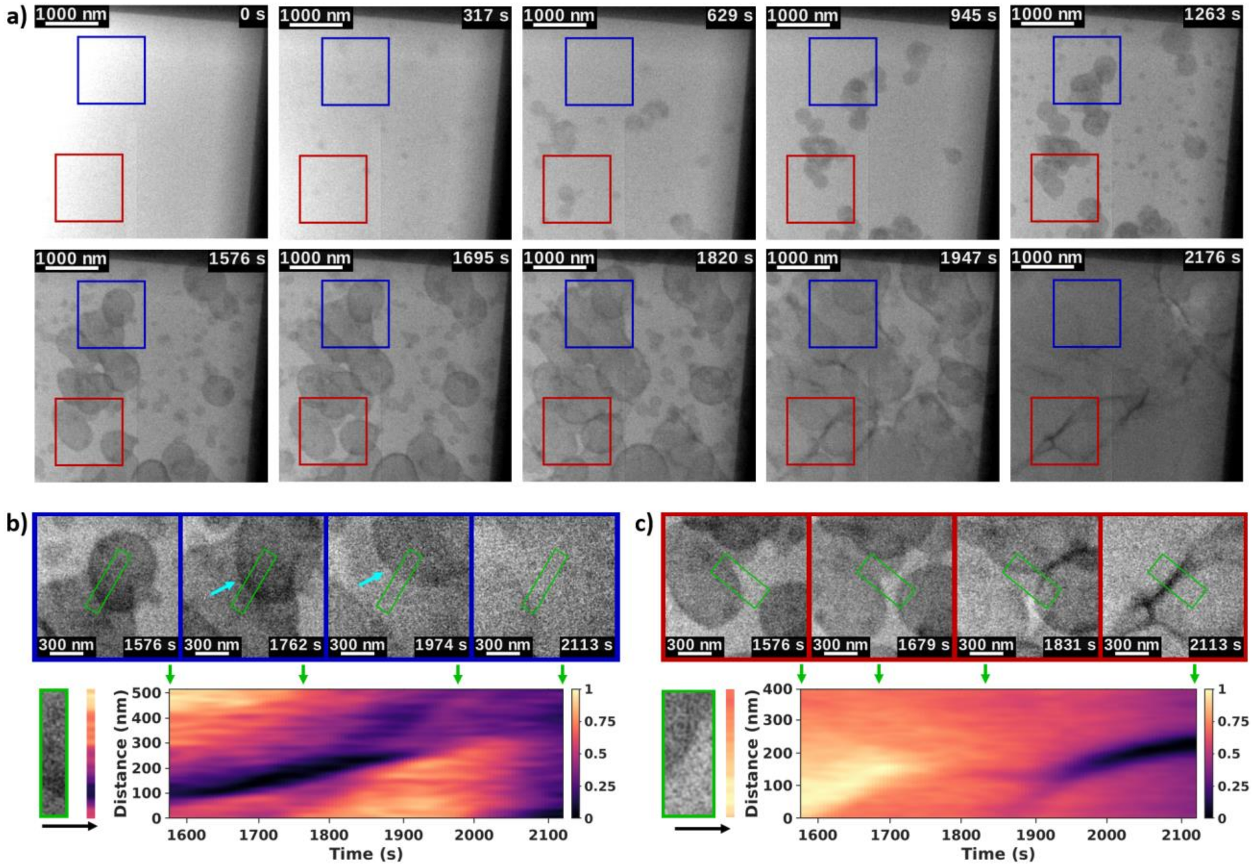

Figure 5.4: LP-TEM analysis of droplet spreading during bilayer formation. (a) Snapshots of the LP-TEM movie (SI MOVIE 2, 11 e^{-} /$nm^{2}\cdot s$) during the solvent exchange process. The blue and red boxes highlight examples of pristine bilayer formation and defect formation, respectively. b) Close view of two droplets completely fusing together to form homogenous bilayer along with cross-sectional time series of the highlighted green box to show a homogenous bilayer area. c) Close view of two droplet droplets merging to form a bilayer boundary along with cross-sectional time series of the highlighted green box to visualize boundary formation.

5.3 CONCLUSION

We have demonstrated that LP-TEM can be used to observe and quantify the formation of supported polymer bilayers with nanoscale resolution in real time. We observed two pathways of bilayer formation derived from vesicle spreading and droplet spreading. For the vesicle spreading mechanism we were able to quantify individual vesicle spread rates and track the formation of membrane rupture points. This method could be extended to image lipid bilayer spreading, although lipids can be much more difficult to image.[67,68] We observed that bilayers formed via the droplet spreading mechanism result in less defects as compared to the vesicle spreading mechanism. Controlling these intermediate pathways could be the key to pristine SB's via the solvent assisted method. The pathways can be controlled by the solvent composition and mixing procedure.[54] Further investigation of supported bilayers using LP-TEM will help guide the design of functional materials. Furthermore, we believe that LP-TEM studies of SBs could be used to image membrane interactions with nanoparticles and proteins. Polymer membranes with tunable lateral diffusion would allow slow enough dynamics to image these interactions using LP-TEM.[69]

5.4 ACKNOWLEDGMENTS

Thanks to Justin Mulvey for carrying out the image analysis for this chapter.

5.5 REFERENCES

(1) de Jonge, N.; Ross, F. M. Electron Microscopy of Specimens in Liquid. *Nat. Nanotechnol.* **2011**, *6* (11), 695–704. https://doi.org/10.1038/nnano.2011.161.

(2) Mirsaidov, U.; Patterson, J. P.; Zheng, H. Liquid Phase Transmission Electron Microscopy for Imaging of Nanoscale Processes in Solution. *MRS Bull.* **2020**, *45* (9), 704–712. https://doi.org/10.1557/mrs.2020.222.

(3) Wu, H.; Friedrich, H.; Patterson, J. P.; Sommerdijk, N. A. J. M.; Jonge, N. de. Liquid-Phase Electron Microscopy for Soft Matter Science and Biology. *Adv. Mater.* **2020**, *32* (25), 2001582. https://doi.org/10.1002/adma.202001582.

(4) Smith, J. W.; Chen, Q. Liquid-Phase Electron Microscopy Imaging of Cellular and Biomolecular Systems. *J. Mater. Chem. B* **2020**, *8* (37), 8490–8506. https://doi.org/10.1039/D0TB01300E.

(5) Liao, H.-G.; Zheng, H. Liquid Cell Transmission Electron Microscopy. *Annu. Rev. Phys. Chem.* **2016**, *67* (1), 719–747. https://doi.org/10.1146/annurev-physchem-040215-112501.

(6) Ou, Z.; Wang, Z.; Luo, B.; Luijten, E.; Chen, Q. Kinetic Pathways of Crystallization at the Nanoscale. *Nat. Mater.* **2020**, *19* (4), 450–455. https://doi.org/10.1038/s41563-019-0514-1.

(7) Kim, J.; Ou, Z.; Jones, M. R.; Song, X.; Chen, Q. Imaging the Polymerization of Multivalent Nanoparticles in Solution. *Nat. Commun.* **2017**, *8* (1), 761. https://doi.org/10.1038/s41467-017-00857-1.

(8) Wang, M.; Dissanayake, T. U.; Park, C.; Gaskell, K.; Woehl, T. J. Nanoscale Mapping of Nonuniform Heterogeneous Nucleation Kinetics Mediated by Surface Chemistry. *J. Am. Chem. Soc.* **2019**, *141* (34), 13516–13524. https://doi.org/10.1021/jacs.9b05225.

(9) Cookman, J.; Hamilton, V.; S. Price, L.; R. Hall, S.; Bangert, U. Visualising Early-Stage Liquid Phase Organic Crystal Growth via Liquid Cell Electron Microscopy. *Nanoscale* **2020**, *12* (7), 4636–4644. https://doi.org/10.1039/C9NR08126G.

(10) Woehl, T. J.; Evans, J. E.; Arslan, I.; Ristenpart, W. D.; Browning, N. D. Direct in Situ Determination of the Mechanisms Controlling Nanoparticle Nucleation and Growth. *ACS Nano* **2012**, *6* (10), 8599–8610. https://doi.org/10.1021/nn303371y.

(11) Wang, H.; Li, B.; Kim, Y.-J.; Kwon, O.-H.; Granick, S. Intermediate States of Molecular Self-Assembly from Liquid-Cell Electron Microscopy. *Proc. Natl. Acad. Sci.* **2020**, *117* (3), 1283–1292. https://doi.org/10.1073/pnas.1916065117.

(12) Zhu, G.; Sushko, M. L.; Loring, J. S.; Legg, B. A.; Song, M.; Soltis, J. A.; Huang, X.; Rosso, K. M.; De Yoreo, J. J. Self-Similar Mesocrystals Form via Interface-Driven Nucleation and Assembly. *Nature* **2021**, *590* (7846), 416–422. https://doi.org/10.1038/s41586-021-03300-0.

(13) Parent, L. R.; Bakalis, E.; Ramírez-Hernández, A.; Kammeyer, J. K.; Park, C.; de Pablo, J.; Zerbetto, F.; Patterson, J. P.; Gianneschi, N. C. Directly Observing Micelle Fusion and Growth in Solution by Liquid-Cell Transmission Electron Microscopy. *J. Am. Chem. Soc.* **2017**, *139* (47), 17140–17151. https://doi.org/10.1021/jacs.7b09060.

(14) Early, J. T.; Yager, K. G.; Lodge, T. P. Direct Observation of Micelle Fragmentation via In Situ Liquid-Phase Transmission Electron Microscopy. *ACS Macro Lett.* **2020**, *9* (5), 756–761. https://doi.org/10.1021/acsmacrolett.0c00273.

(15) Ianiro, A.; Wu, H.; Rijt, M. M. J. van; Vena, M. P.; Keizer, A. D. A.; Esteves, A. C. C.; Tuinier, R.; Friedrich, H.; Sommerdijk, N. A. J. M.; Patterson, J. P. Liquid–Liquid Phase Separation during Amphiphilic Self-Assembly. *Nat. Chem.* **2019**, *11* (4), 320–328. https://doi.org/10.1038/s41557-019-0210-4.

(16) Rizvi, A.; Mulvey, J. T.; Carpenter, B. P.; Talosig, R.; Patterson, J. P. A Close Look at Molecular Self-Assembly with the Transmission Electron Microscope. *Chem. Rev.* **2021**. https://doi.org/10.1021/acs.chemrev.1c00189.

(17) Sackmann, E. Supported Membranes: Scientific and Practical Applications. *Science* **1996**, *271* (5245), 43–48. https://doi.org/10.1126/science.271.5245.43.

(18) Groves, J. T.; Ulman, N.; Boxer, S. G. Micropatterning Fluid Lipid Bilayers on Solid Supports. *Science* **1997**, *275* (5300), 651–653. https://doi.org/10.1126/science.275.5300.651.

(19) Tamm, L. K.; McConnell, H. M. Supported Phospholipid Bilayers. *Biophys. J.* **1985**, *47* (1), 105–113. https://doi.org/10.1016/S0006-3495(85)83882-0.

(20) Richter, R. P.; Bérat, R.; Brisson, A. R. Formation of Solid-Supported Lipid Bilayers: An Integrated View. *Langmuir* **2006**, *22* (8), 3497–3505. https://doi.org/10.1021/la052687c.

(21) Belegrinou, S.; Dorn, J.; Kreiter, M.; Kita-Tokarczyk, K.; Sinner, E.-K.; Meier, W. Biomimetic Supported Membranes from Amphiphilic Block Copolymers. *Soft Matter* **2009**, *6* (1), 179–186. https://doi.org/10.1039/B917318H.

(22) Rakhmatullina, E.; Meier, W. Solid-Supported Block Copolymer Membranes through Interfacial Adsorption of Charged Block Copolymer Vesicles. *Langmuir* **2008**, *24* (12), 6254–6261. https://doi.org/10.1021/la8003068.

(23) Jung, H.; Robison, A. D.; Cremer, P. S. Multivalent Ligand–Receptor Binding on Supported Lipid Bilayers. *J. Struct. Biol.* **2009**, *168* (1), 90–94. https://doi.org/10.1016/j.jsb.2009.05.010.

(24) Liu, C.; Huang, D.; Yang, T.; Cremer, P. S. Simultaneous Detection of Multiple Proteins That Bind to the Identical Ligand in Supported Lipid Bilayers. *Anal. Chem.* **2015**, *87* (14), 7163–7170. https://doi.org/10.1021/acs.analchem.5b00999.

(25) Godefroy, C.; Dahmane, S.; Dosset, P.; Adam, O.; Nicolai, M.-C.; Ronzon, F.; Milhiet, P.-E. Mimicking Influenza Virus Fusion Using Supported Lipid Bilayers. *Langmuir* **2014**, *30* (38), 11394–11400. https://doi.org/10.1021/la502591a.

(26) Dustin, M. L. Supported Bilayers at the Vanguard of Immune Cell Activation Studies. *J. Struct. Biol.* **2009**, *168* (1), 152–160. https://doi.org/10.1016/j.jsb.2009.05.007.

(27) Hennig, M.; Neumann, J.; Wixforth, A.; Rädler, J. O.; Schneider, M. F. Dynamic Patterns in a Supported Lipid Bilayer Driven by Standing Surface Acoustic Waves. *Lab. Chip* **2009**, *9* (21), 3050–3053. https://doi.org/10.1039/B907157A.

(28) Seu, K. J.; Cambrea, L. R.; Everly, R. M.; Hovis, J. S. Influence of Lipid Chemistry on Membrane Fluidity: Tail and Headgroup Interactions. *Biophys. J.* **2006**, *91* (10), 3727–3735. https://doi.org/10.1529/biophysj.106.084590.

(29) Jung, H.; Robison, A. D.; Cremer, P. S. Detecting Protein−Ligand Binding on Supported Bilayers by Local PH Modulation. *J. Am. Chem. Soc.* **2009**, *131* (3), 1006–1014. https://doi.org/10.1021/ja804542p.

(30) Kita-Tokarczyk, K.; Itel, F.; Grzelakowski, M.; Egli, S.; Rossbach, P.; Meier, W. Monolayer Interactions between Lipids and Amphiphilic Block Copolymers. *Langmuir* **2009**, *25* (17), 9847–9856. https://doi.org/10.1021/la900948a.

(31) Haefele, T.; Kita-Tokarczyk, K.; Meier, W. Phase Behavior of Mixed Langmuir Monolayers from Amphiphilic Block Copolymers and an Antimicrobial Peptide. *Langmuir* **2006**, *22* (3), 1164–1172. https://doi.org/10.1021/la0524216.

(32) Keller, C. A.; Glasmästar, K.; Zhdanov, V. P.; Kasemo, B. Formation of Supported Membranes from Vesicles. *Phys. Rev. Lett.* **2000**, *84* (23), 5443–5446. https://doi.org/10.1103/PhysRevLett.84.5443.

(33) Cremer, P. S.; Boxer, S. G. Formation and Spreading of Lipid Bilayers on Planar Glass Supports. *J. Phys. Chem. B* **1999**, *103* (13), 2554–2559. https://doi.org/10.1021/jp983996x.

(34) Reviakine, I.; Brisson, A. Formation of Supported Phospholipid Bilayers from Unilamellar Vesicles Investigated by Atomic Force Microscopy. *Langmuir* **2000**, *16* (4), 1806–1815. https://doi.org/10.1021/la9903043.

(35) Lind, T. K.; Cárdenas, M. Understanding the Formation of Supported Lipid Bilayers via Vesicle Fusion—A Case That Exemplifies the Need for the Complementary Method Approach (Review). *Biointerphases* **2016**, *11* (2), 020801. https://doi.org/10.1116/1.4944830.

(36) Pawłowski, J.; Juhaniewicz, J.; Güzeloğlu, A.; Sęk, S. Mechanism of Lipid Vesicles Spreading and Bilayer Formation on a Au(111) Surface. *Langmuir* **2015**, *31* (40), 11012–11019. https://doi.org/10.1021/acs.langmuir.5b01331.

(37) Reimhult, E.; Höök, F.; Kasemo, B. Intact Vesicle Adsorption and Supported Biomembrane Formation from Vesicles in Solution: Influence of Surface Chemistry, Vesicle Size, Temperature, and Osmotic Pressure. *Langmuir* **2003**, *19* (5), 1681–1691. https://doi.org/10.1021/la0263920.

(38) Tabaei, S. R.; Jackman, J. A.; Kim, S.-O.; Zhdanov, V. P.; Cho, N.-J. Solvent-Assisted Lipid Self-Assembly at Hydrophilic Surfaces: Factors Influencing the Formation of Supported Membranes. *Langmuir* **2015**, *31* (10), 3125–3134. https://doi.org/10.1021/la5048497.

(39) Tabaei, S. R.; Choi, J.-H.; Haw Zan, G.; Zhdanov, V. P.; Cho, N.-J. Solvent-Assisted Lipid Bilayer Formation on Silicon Dioxide and Gold. *Langmuir* **2014**, *30* (34), 10363–10373. https://doi.org/10.1021/la501534f.

(40) Tabaei, S. R.; Jackman, J. A.; Liedberg, B.; Parikh, A. N.; Cho, N.-J. Observation of Stripe Superstructure in the β-Two-Phase Coexistence Region of Cholesterol–Phospholipid Mixtures in Supported Membranes. *J. Am. Chem. Soc.* **2014**, *136* (49), 16962–16965. https://doi.org/10.1021/ja5082537.

(41) Jackman, J. A.; Tabaei, S. R.; Zhao, Z.; Yorulmaz, S.; Cho, N.-J. Self-Assembly Formation of Lipid Bilayer Coatings on Bare Aluminum Oxide: Overcoming the Force of Interfacial Water. *ACS Appl. Mater. Interfaces* **2015**, *7* (1), 959–968. https://doi.org/10.1021/am507651h.

(42) Jackman, J. A.; Cho, N.-J. Supported Lipid Bilayer Formation: Beyond Vesicle Fusion. *Langmuir* **2020**, *36* (6), 1387–1400. https://doi.org/10.1021/acs.langmuir.9b03706.

(43) Ferhan, A. R.; Yoon, B. K.; Park, S.; Sut, T. N.; Chin, H.; Park, J. H.; Jackman, J. A.; Cho, N.-J. Solvent-Assisted Preparation of Supported Lipid Bilayers. *Nat. Protoc.* **2019**, *14* (7), 2091–2118. https://doi.org/10.1038/s41596-019-0174-2.

(44) Richter, R.; Mukhopadhyay, A.; Brisson, A. Pathways of Lipid Vesicle Deposition on Solid Surfaces: A Combined QCM-D and AFM Study. *Biophys. J.* **2003**, *85* (5), 3035–3047. https://doi.org/10.1016/S0006-3495(03)74722-5.

(45) Weirich, K. L.; Israelachvili, J. N.; Fygenson, D. K. Bilayer Edges Catalyze Supported Lipid Bilayer Formation. *Biophys. J.* **2010**, *98* (1), 85–92. https://doi.org/10.1016/j.bpj.2009.09.050.

(46) Andrecka, J.; Spillane, K. M.; Ortega-Arroyo, J.; Kukura, P. Direct Observation and Control of Supported Lipid Bilayer Formation with Interferometric Scattering Microscopy. *ACS Nano* **2013**, *7* (12), 10662–10670. https://doi.org/10.1021/nn403367c.

(47) Mai, Y.; Eisenberg, A. Self-Assembly of Block Copolymers. *Chem. Soc. Rev.* **2012**, *41* (18), 5969–5985. https://doi.org/10.1039/C2CS35115C.

(48) Luo, L.; Eisenberg, A. Thermodynamic Size Control of Block Copolymer Vesicles in Solution. *Langmuir* **2001**, *17* (22), 6804–6811. https://doi.org/10.1021/la0104370.

(49) Patterson, J. P.; Sanchez, A. M.; Petzetakis, N.; Smart, T. P.; Epps, III, T. H.; Portman, I.; Wilson, N. R.; O'Reilly, R. K. A Simple Approach to Characterizing Block Copolymer Assemblies: Graphene Oxide Supports for High Contrast Multi-Technique Imaging. *Soft Matter* **2012**, *8* (12), 3322. https://doi.org/10.1039/c2sm07040e.

(50) Discher, D. E.; Eisenberg, A. Polymer Vesicles. *Science* **2002**, *297* (5583), 967–973. https://doi.org/10.1126/science.1074972.

(51) Zhang, L.; Eisenberg, A. Multiple Morphologies of "Crew-Cut" Aggregates of Polystyrene-b-Poly(Acrylic Acid) Block Copolymers. *Science* **1995**, *268* (5218), 1728–1731. https://doi.org/10.1126/science.268.5218.1728.

(52) Hackley, V. A. Colloidal Processing of Silicon Nitride with Poly(Acrylic Acid): I, Adsorption and Electrostatic Interactions. *J. Am. Ceram. Soc.* **1997**, *80* (9), 2315–2325. https://doi.org/10.1111/j.1151-2916.1997.tb03122.x.

(53) Ferhan, A. R.; Yoon, B. K.; Park, S.; Sut, T. N.; Chin, H.; Park, J. H.; Jackman, J. A.; Cho, N.-J. Solvent-Assisted Preparation of Supported Lipid Bilayers. *Nat. Protoc.* **2019**, *14* (7), 2091–2118. https://doi.org/10.1038/s41596-019-0174-2.

(54) Rizvi, A.; Patel, U.; Ianiro, A.; Hurst, P. J.; Merham, J. G.; Patterson, J. P. Nonionic Block Copolymer Coacervates. *Macromolecules* **2020**, *53* (14), 6078–6086. https://doi.org/10.1021/acs.macromol.0c00979.

(55) Wang, M.; Park, C.; Woehl, T. J. Quantifying the Nucleation and Growth Kinetics of Electron Beam Nanochemistry with Liquid Cell Scanning Transmission Electron Microscopy. *Chem. Mater.* **2018**, *30* (21), 7727–7736. https://doi.org/10.1021/acs.chemmater.8b03050.

(56) Woehl, T. J.; Moser, T.; Evans, J. E.; Ross, F. M. Electron-Beam-Driven Chemical Processes during Liquid Phase Transmission Electron Microscopy. *MRS Bull.* **2020**, *45* (9), 746–753. https://doi.org/10.1557/mrs.2020.227.
(57) Jiang, N. Note on in Situ (Scanning) Transmission Electron Microscopy Study of Liquid Samples. *Ultramicroscopy* **2017**, *179*, 81–83. https://doi.org/10.1016/j.ultramic.2017.04.012.
(58) Woehl, T. J.; Abellan, P. Defining the radiation chemistry during liquid cell electron microscopy to enable visualization of nanomaterial growth and degradation dynamics. *J. Microsc.* **2017**, *265* (2), 135–147. https://doi.org/10.1111/jmi.12508.
(59) Hamai, C.; Cremer, P. S.; Musser, S. M. Single Giant Vesicle Rupture Events Reveal Multiple Mechanisms of Glass-Supported Bilayer Formation. *Biophys. J.* **2007**, *92* (6), 1988–1999. https://doi.org/10.1529/biophysj.106.093831.
(60) Zheng, H.; Claridge, S. A.; Minor, A. M.; Alivisatos, A. P.; Dahmen, U. Nanocrystal Diffusion in a Liquid Thin Film Observed by in Situ Transmission Electron Microscopy. *Nano Lett.* **2009**, *9* (6), 2460–2465. https://doi.org/10.1021/nl9012369.
(61) Patterson, J. P.; Abellan, P.; Denny, M. S.; Park, C.; Browning, N. D.; Cohen, S. M.; Evans, J. E.; Gianneschi, N. C. Observing the Growth of Metal–Organic Frameworks by in Situ Liquid Cell Transmission Electron Microscopy. *J. Am. Chem. Soc.* **2015**, *137* (23), 7322–7328. https://doi.org/10.1021/jacs.5b00817.
(62) Banerjee, S.; Lyubchenko, Y. L. Topographically Smooth and Stable Supported Lipid Bilayer for High-Resolution AFM Studies. *Methods* **2021**. https://doi.org/10.1016/j.ymeth.2021.02.010.
(63) Keller, C. A.; Kasemo, B. Surface Specific Kinetics of Lipid Vesicle Adsorption Measured with a Quartz Crystal Microbalance. *Biophys. J.* **1998**, *75* (3), 1397–1402.
(64) Dorn, J.; Belegrinou, S.; Kreiter, M.; Sinner, E.-K.; Meier, W. Planar Block Copolymer Membranes by Vesicle Spreading. *Macromol. Biosci.* **2011**, *11* (4), 514–525. https://doi.org/10.1002/mabi.201000396.
(65) Yewdall, N. A.; André, A. A. M.; Lu, T.; Spruijt, E. Coacervates as Models of Membraneless Organelles. *Curr. Opin. Colloid Interface Sci.* **2021**, *52*, 101416. https://doi.org/10.1016/j.cocis.2020.101416.
(66) Li, C.; Chen Tho, C.; Galaktionova, D.; Chen, X.; Král, P.; Mirsaidov, U. Dynamics of Amphiphilic Block Copolymers in an Aqueous Solution: Direct Imaging of Micelle Formation and Nanoparticle Encapsulation. *Nanoscale* **2019**, *11* (5), 2299–2305. https://doi.org/10.1039/C8NR08922A.
(67) Gnanasekaran, K.; Chang, H.; Smeets, P. J. M.; Korpanty, J.; Geiger, F. M.; Gianneschi, N. C. In Situ Ni2+ Stain for Liposome Imaging by Liquid-Cell Transmission Electron Microscopy. *Nano Lett.* **2020**, *20* (6), 4292–4297. https://doi.org/10.1021/acs.nanolett.0c00898.
(68) Piffoux, M.; Ahmad, N.; Nelayah, J.; Wilhelm, C.; Silva, A.; Gazeau, F.; Alloyeau, D. Monitoring the Dynamics of Cell-Derived Extracellular Vesicles at the Nanoscale by Liquid-Cell Transmission Electron Microscopy. *Nanoscale* **2018**, *10* (3), 1234–1244. https://doi.org/10.1039/C7NR07576F.
(69) Discher, D. E.; Ahmed, F. Polymersomes. *Annu. Rev. Biomed. Eng.* **2006**, *8* (1), 323–341. https://doi.org/10.1146/annurev.bioeng.8.061505.095838.

Appendix D: Supplementary Information for Chapter 5

D.1 Materials and Instruments**:**

All reagents were purchased from Acros Organics, Fisher Scientific, or Sigma-Aldrich, and used without further purification unless otherwise noted. ^{1}H NMR spectra were collected on a 500 MHz Bruker Avance spectrometer. All samples were taken in $CDCl_{3.}$ Chemical shifts are provided in ppm, calibrated from the residual $CDCl_3$ peak (7.26 ppm). All TEM experiments were performed on a JEOL 2100 equipped with a 200 keV field emission gun and a OneView camera, Irvine Materials Research Institute, University of California, Irvine. Liquid Phase imaging was performed with a DENS solutions Ocean holder using 0 nm spacer chips. Optical imaging were performed using a Keyence Bz-X810 all in one microscope. Size exclusion chromatography (SEC) was performed in DMF using an Agilent 1100 chromatograph equipped with RID detector and a PL gel 5 µm 300x7.5 mm mixed column. All samples were calibrated against polystyrene standards (MW= 580, 1300, 5000, 10000, 30000, 70000, 130000 g/mol).

D.2 Experiential Methods

D.2.1 LP-TEM Methods:

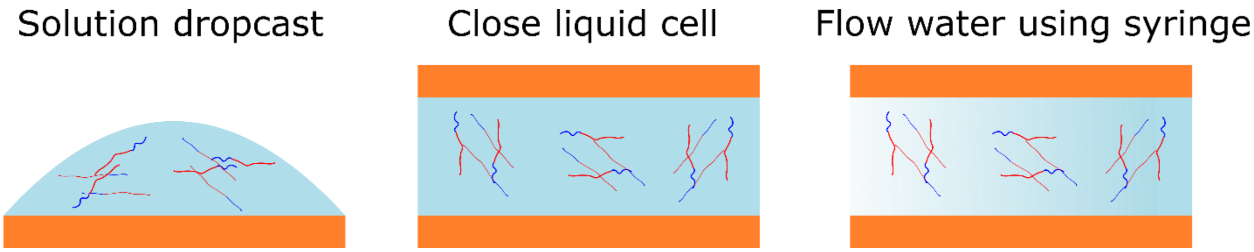

Figure D1: Schematic of liquid cell setup for imaging.

Silicon Nitride chips are washed with acetone, IPA, EtOH and cleaned using a Gatan plasma cleaner (Ar/O_2). The bottom chip is then loaded in the holder, a small droplet (≈ 0.5 uL) of the sample (PS_{200}-*b*-PAA_{35}, 10 mg mL^{-1} in THF:Dioxane)[1] is drop casted in the middle of the chip right above the silicon nitride window. The top chip is then placed above the droplet and the cell is sealed. The holder is then placed into a leak test station. Upon passing the leak test the holder is then inserted in the microscope, with pre-aligned electron beam and the apertures set to image. To initiate the self-assembly, water is flowed in using a 500 µL syringe.[2] TEM imaging was performed on a JEOL-2100F TEM using a Schottky type field emission gun operating at 200 kV with an electron dose rates ranging between 11 and 15 $e^-/nm^2 \cdot s$. Images were recorded with the following frametimes: 2 seconds for SI MOVIE 1, 5 seconds for Si MOVIE 2, and 2.6 seconds for the control experiments. TEM Recorder script for DigitalMicrograph was used and the images were collected using the Gatan Oneview Camera.[3]

D.2.2 Synthesis of P*t*BuA$_{30}$

To a schlenck tube, [S-dodecyl-S'-(α',α'-dimethyl-α''-acetic acid)] (DDMAT, 0.18 g, 0.5 mmol), tert-butylacrylate (4.0 g, 31.2 mmol), AIBN (8.2 mg, 0.05) were added and dissolved in dioxane (5 mL). The solution was stirred and purged for 30 min with N_2 to deoxygenate the solution. The solution was heated to 65 ^oC for 70 min to initiate the polymerization. The polymerization was stopped by cooling the solution down to 0 ^oC. The viscous solution was dissolved in minimum amount of THF and poured into a mixture (by volume of 7:1 cold $MeOH:H_2O$. The $MeOH:H_2O$ solution was decanted, and the polymer was dissolved in THF and the solution was dried over $MgSO_4$. The solution was filtered and the solvent was removed *in vacuo* yielding a yellow foam, P^tBuA. M_n (^1H NMR) = 4200 g mol^{-1}, M_w/M_n (SEC) = 1.17. ^1H NMR ($CDCl_3$): δ (ppm) 3.33 (t, J =

7.4 Hz, 2H, SCSC*H2*), 1.20-1.50 (br, C(CH3)3 polymer backbone), 1.30-2.30 (br, CH and CH2 polymer backbone) 0.88 (t, J 6.8 Hz, 3H, (CH2)11C*H*3).

Chain Extension of P*t*BuA with Styrene to give P*t*BuA$_{30}$-b-PS$_{200}$

To a schlenck tube, **P^{t}BuA$_{30}$** (2.7 g, 0.42 mmol), Styrene (18.3 g, 175.4 mmol) were added and the solution was purged with N_2 while stirring to deoxygenate the solution. The solution was then heated to 110 ^{o}C overnight and cooled to 0 ^{o}C to stop the polymerization. The reaction mixture had “gelled” due to high styrene concentration, which restricted the conversion calculation. The gelled solution was dissolved in THF with sonication for several hours. The dissolved polymer solution was precipitated into cold MeOH three times. The Polymer was filtered and dried *in vacuo* (16 g). M_n (^{1}H NMR)= 25,000 g mol^{-1}. M_w/M_n (SEC) = 1.21. ^{1}H NMR (CDCl3): δ (ppm) 6.25-7.25 (br, Ar-H polymer backbone), 3.33 (br, 2H, SCSC*H2*), 1.20-1.50 (br, C(CH3)3 polymer backbone), 1.30-2.30 (br, CH and CH2 polymer backbone) 0.88 (br, 3H, (CH2)11C*H*3).

Conversion of P*t*BuA$_{30}$-b-PS$_{200}$ to PAA$_{30}$-b-PS$_{200}$

P*t*BuA$_{30}$-b-PS$_{200}$ (2.0 g, 0.09 mmol) was charged into a 250 mL round bottom flask with a stir bar. The polymer was dissolved in DCM (80 mL) and cooled to 0 ^{o}C in an ice bath. After the solution was cooled, TFA (40 mL) was slowly added to the reaction mixture, the reaction was stirred overnight. The cloudy solution was dried in air and the solids were dissolved in THF, the undissolved precipitate was filtered, and the polymer solution was precipitated twice into cold MeOH. The polymer was filtered and dried *in vacuo* (1.1 g). FT-IR was used to confirm the deprotection of the tertbutyl group (Figure S9).

D.2.3 Size exclusion chromatography

A solution of 1 mg ml^{-1} is made in DMF and filtered using a 0.2 um syringe filter. A GPC vial is charged with the filtered solution and sealed with slit containing cap. The vial is placed in the autosampler, and the standard GPC method is used to collect the chromatogram. The results are then evaluated using the most recent polystyrene standards. The SEC results are mainly used to measure the poly dispersity pf the block copolymers as the MW of block copolymers cannot be estimated with confidence using homopolymer standards.

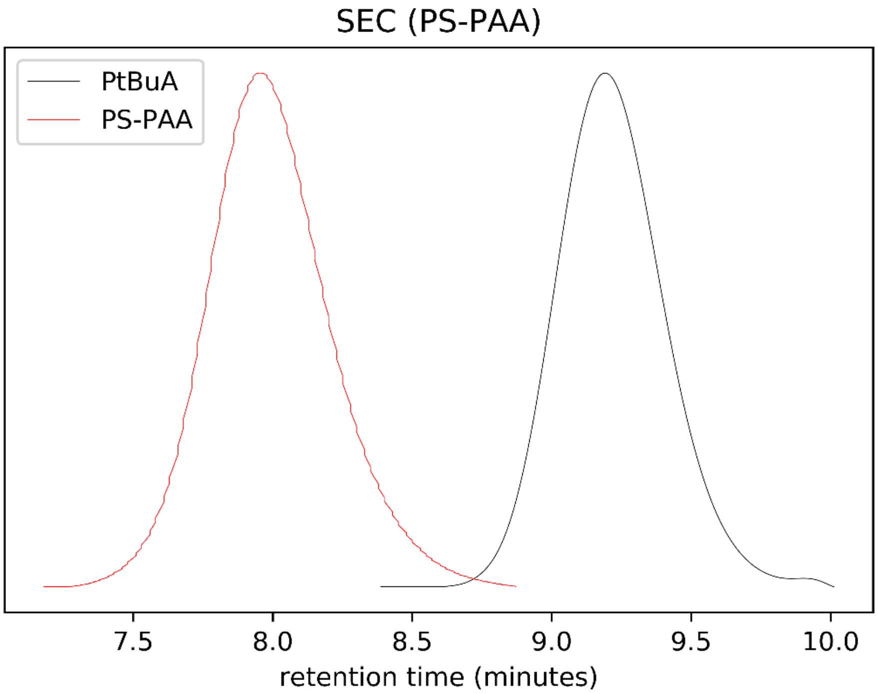

Figure D2: Chromatogram of PolytertButyl acrylate and Poly(styrene)$_{200}$-*b*-polyacrylic acid$_{30}$.

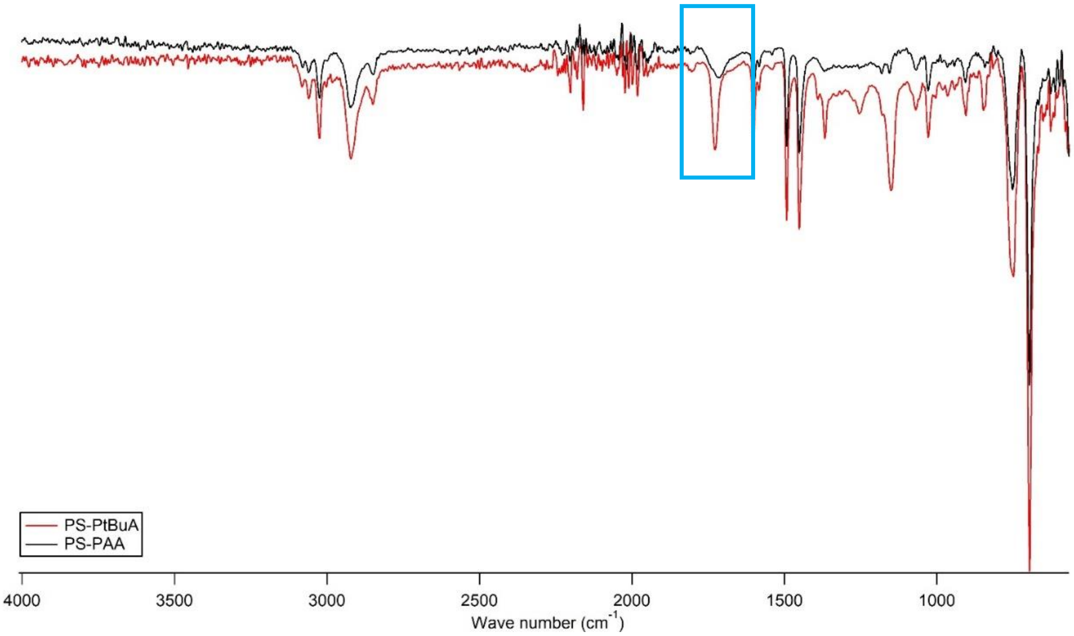

Figure D3**:** FTIR spectra of PS$_{200}$-PtBuA$_{30}$ and PS$_{200}$-PAA$_{30}$ overlayed. The blue box highlights the conversion of the sharp ester carbonyl peak to the broader carboxylic acid carbonyl peak.

D.2.4 Control LP-TEM experiments:

Identical LP-TEM experiment control experiments of PS-b-PAA in a mixture of THF:Dioxane and water (1:1) and in pure water. Controls were imaged at 13 e^- /nm^2·s under the same conditions as the experimental datasets. No morphological changes were observed in the vesicles. In all controls there was a background precipitation event which is discussed in more detail below. The droplet phase was not imaged as a control as it is impossible to prepare stable nano-droplets for the control. However, from our own experiments and known mechanisms of electron beam damage we suspect significantly less beam damage in the droplet phase as the organic content is greater for droplet formation (≈ 90%) as compared to vesicles (<70%).[4]

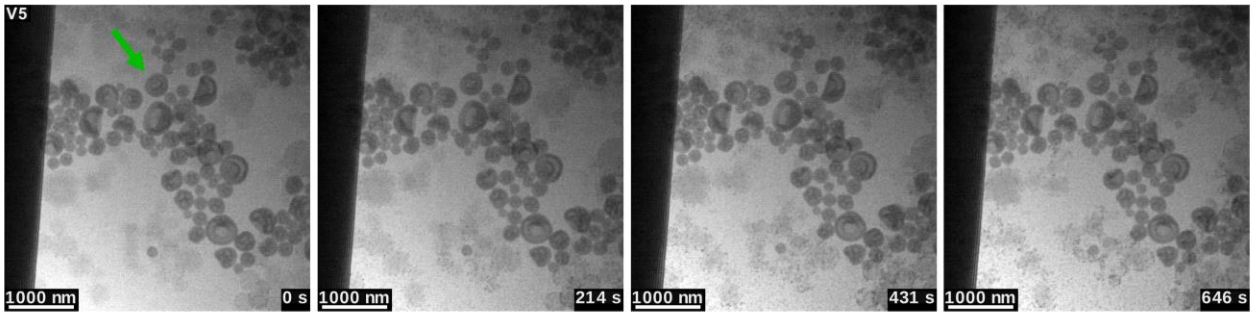

Figure D4: Imaging preformed vesicles at 13 e^-/nm^2·s in organic:water mixture to visualize any electron beam induced transformations. Arrow indicated particle used for quantitative analysis (Figure S7).

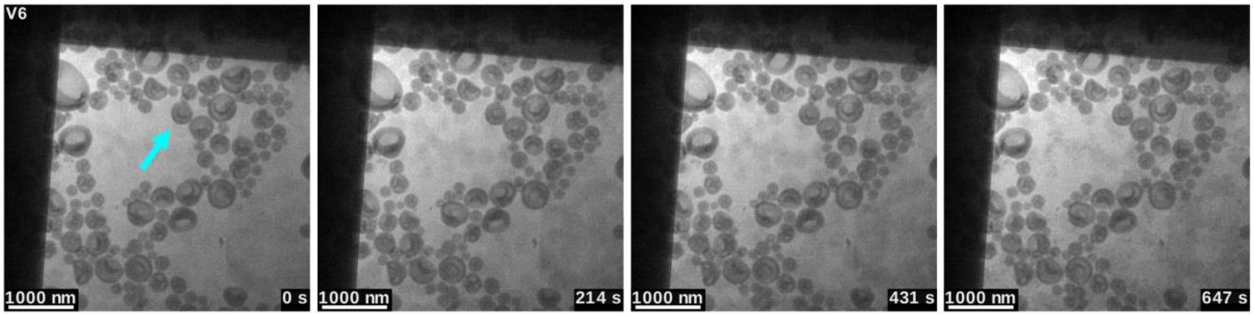

Figure D5: Imaging preformed vesicles at 13 $e^-/nm^2\cdot s$ in organic:water mixture to visualize any electron beam induced transformations. Arrow indicated particle used for quantitative analysis (Figure S9).

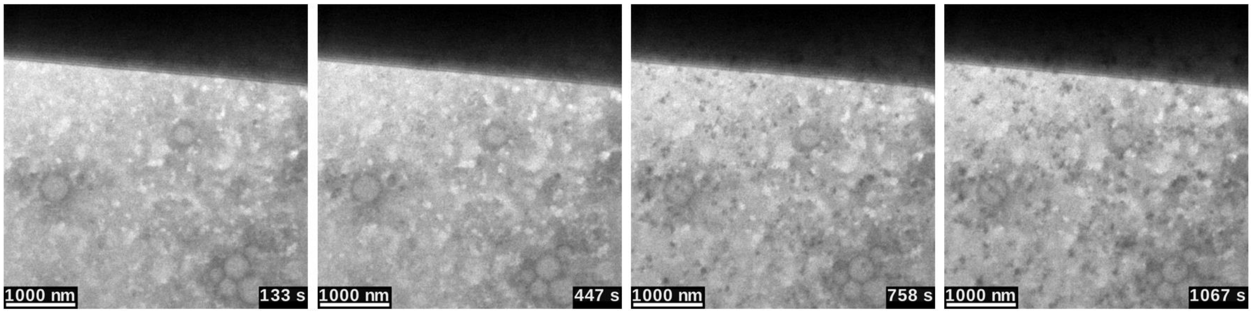

Figure D6: Imaging preformed vesicles at 13 $e^-/nm^2\cdot s$ in pure water. Note the first and last frames are not shown due to camera movement.

D.2.6 Estimation of the electron dosage

The electron dose for each experiment was calculated by using the conversion factor of the detector provided by the manufacturer. Flat field images (where no sample was inserted) were collected prior to the experiment with the same microscope setting used for the experiment. The flat field images are used to obtain the average number of counts per unit area based on the pixel size of the image. The conversion factor conversion factor is given in counts per electron and can be used to determine the number of $e^-/nm^2\cdot s$.

D.2.6 Electron beam effects during LP-TEM imaging

It has been well established that the electron beam will affect all LP-TEM experiments.[5,6] The purpose of the control experiments is to determine which features of our SB formation experiments are related to changes in the solvent composition and which are related to exposure by the electron beam. As SB formation occurs in an of organic solvent: water, the controls in Figure S2 and S3 are the most important. The vesicles did not undergo any changes in morphology indicating that our observations of rupture and spreading in the SB formation experiments are initiated by the solvent exchange and not the electron beam. This does not mean the electron beam is not having any effect, however further experiments which are outside the scope of this paper would need to be performed to elucidate that effect. The control sample showed some background precipitation which may occur due to the crosslinking of residual polymer chains in the solvent.[7] This precipitation event was not observed in the experimental datasets.

Although our experiment system is an organic : water mixture we performed a control in pure water to see if the organic solvent aids in our visualization. It is well known that there is a stark difference in the behavior of fast electrons in aqueous and organic media.[8,9] Organic solvents are known to act as scavengers towards the reactive species minimizing/slowing down electron beam induced damage.[4,10] Our control in pure water shows that the vesicles have much worse feature resolution and the beam induced precipitation occurs much earlier. This was observed over multiple experiments for both controls. Both these observations suggest that the presence of organic solvent (THF and Dioxane) in our experiments are improving resolution are protective against beam damage.

D.2.7 Bilayer Coverage Calculation

The percent coverage of the bilayer in the liquid cell viewing area was calculated based on the last frame of the SI MOVIE 2. The area of the cell covered by the bilayer was traced by hand in ImageJ (Figure S13). The dark edges of the cell were omitted from the percent coverage calculation. The number of pixels representing the covered area (green tint) was divided by the number of pixels in the viewing area (the rest of the image, not including the edge of the cell). The result was 99.8% coverage of the bilayer.

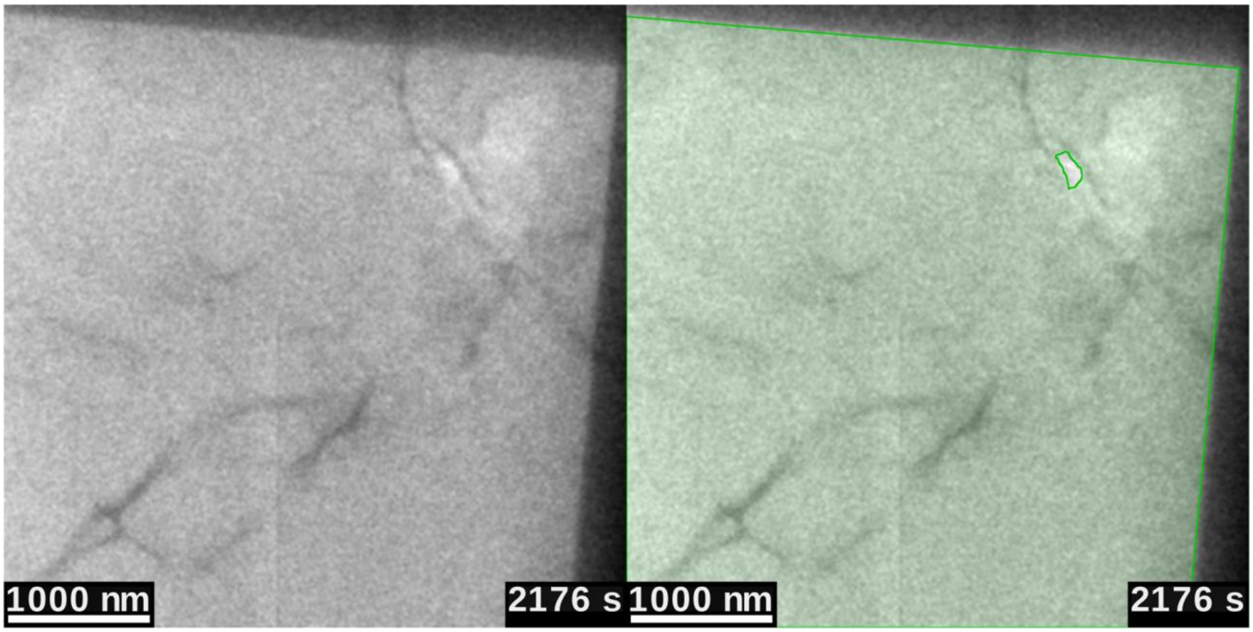

Figure D7: Percent coverage of the bilayer in the viewing area for the last frame of SI MOVIE 2. The covered area was segmented manually and given a green tint in the right image.

D.2.8 Dynamic Light Scattering

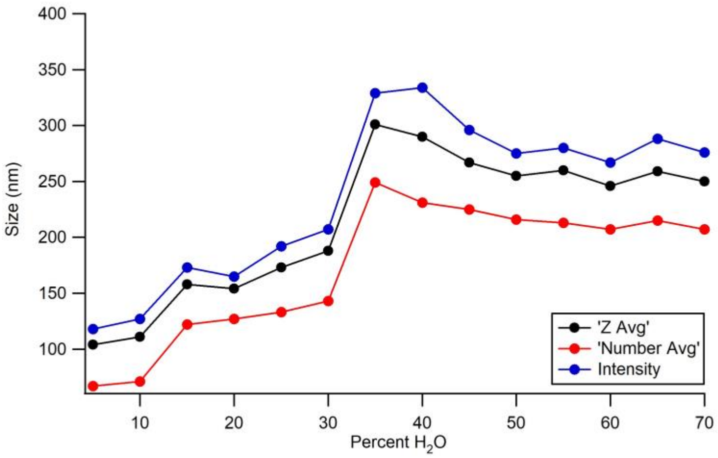

Figure D8**:** Dynamic light scattering of ex-situ vesicle formation and evolution as the water content increases.

D.2.9 Solvent Switch Ex-situ

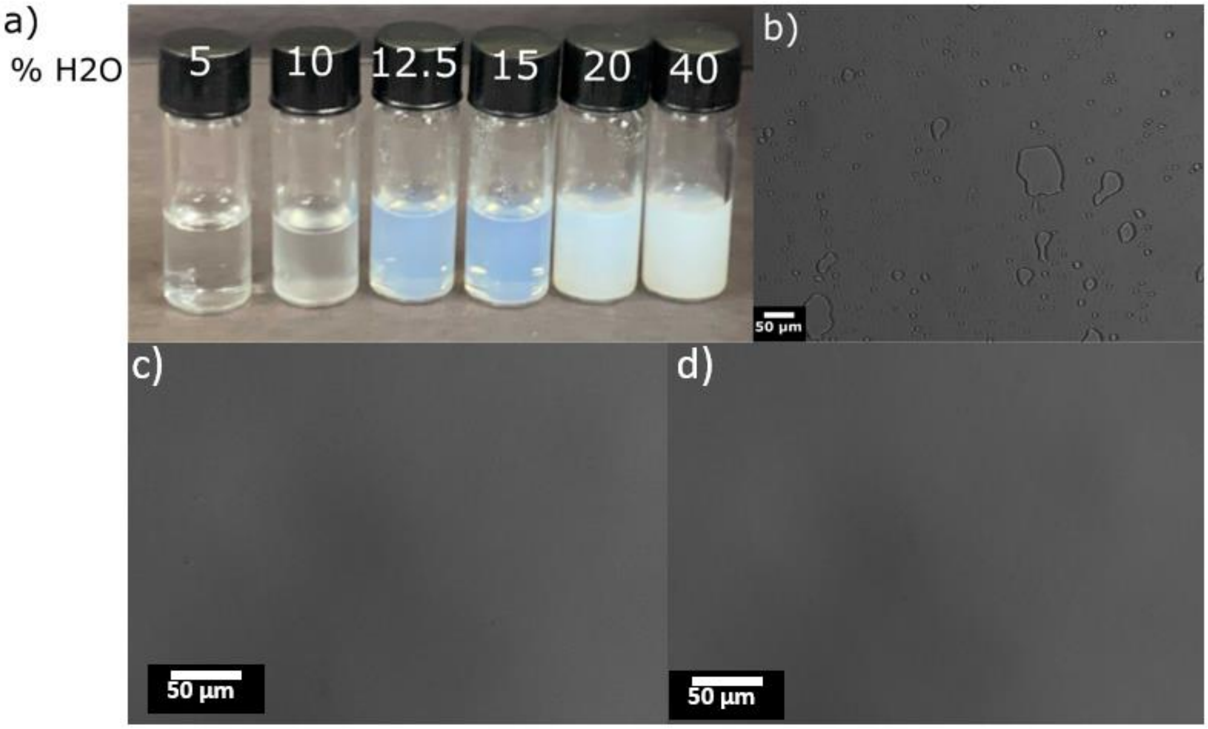

Figure D9**:** Solvent switch of PS_{200}-*b*-PAA_{30} in (THF 44:DIOXANE 56) and water mixture. a) Solvent switch experiment showcasing stable coacervate formation at ≈ 10% H_2O b) Bright field optical microscopy image of droplets (coacervates) formed at 10% H_2O. c) Bright field optical microscopy image showing no droplets at 30% H_2O. d) Bright field optical microscopy image showing no droplets at 50% H_2O.

D.2.9 References

(1) Luo, L.; Eisenberg, A. Thermodynamic Size Control of Block Copolymer Vesicles in Solution. *Langmuir* **2001**, *17* (22), 6804–6811. https://doi.org/10.1021/la0104370.

(2) Ianiro, A.; Wu, H.; Rijt, M. M. J. van; Vena, M. P.; Keizer, A. D. A.; Esteves, A. C. C.; Tuinier, R.; Friedrich, H.; Sommerdijk, N. A. J. M.; Patterson, J. P. Liquid–Liquid Phase Separation during Amphiphilic Self-Assembly. *Nat. Chem.* **2019**, *11* (4), 320–328. https://doi.org/10.1038/s41557-019-0210-4.

(3) Mitchell, D. R. G.; Schaffer, B. Scripting-Customised Microscopy Tools for Digital Micrograph^{TM}. *Ultramicroscopy* **2005**, *103* (4), 319–332. https://doi.org/10.1016/j.ultramic.2005.02.003.

(4) Woehl, T. J.; Moser, T.; Evans, J. E.; Ross, F. M. Electron-Beam-Driven Chemical Processes during Liquid Phase Transmission Electron Microscopy. *MRS Bull.* **2020**, *45* (9), 746–753. https://doi.org/10.1557/mrs.2020.227.

(5) Rizvi, A.; Mulvey, J. T.; Carpenter, B. P.; Talosig, R.; Patterson, J. P. A Close Look at Molecular Self-Assembly with the Transmission Electron Microscope. *Chem. Rev.* **2021**. https://doi.org/10.1021/acs.chemrev.1c00189.

(6) Wu, H.; Friedrich, H.; Patterson, J. P.; Sommerdijk, N. A. J. M.; Jonge, N. de. Liquid-Phase Electron Microscopy for Soft Matter Science and Biology. *Adv. Mater.* **2020**, *32* (25), 2001582. https://doi.org/10.1002/adma.202001582.

(7) Dissanayake, T. U.; Wang, M.; Woehl, T. J. Revealing Reactions between the Electron Beam and Nanoparticle Capping Ligands with Correlative Fluorescence and Liquid-Phase Electron Microscopy. *ACS Appl. Mater. Interfaces* **2021**, *13* (31), 37553–37562. https://doi.org/10.1021/acsami.1c10957.

(8) Mincher, B. J. The Effects of Radiation Chemistry on Radiochemistry: When Unpaired Electrons Defy Great Expectations. *J. Radioanal. Nucl. Chem.* **2018**, *316* (2), 799–804. https://doi.org/10.1007/s10967-018-5728-1.

(9) Radiochemistry and Nuclear Chemistry - 3rd Edition https://www.elsevier.com/books/radiochemistry-and-nuclear-chemistry/choppin/978-0-7506-7463-8 (accessed 2021 -08 -20).

(10) Woehl, T. J.; Abellan, P. Defining the radiation chemistry during liquid cell electron microscopy to enable visualization of nanomaterial growth and degradation dynamics. *J. Microsc.* **2017**, *265* (2), 135–147. https://doi.org/10.1111/jmi.12508.

(11) Yao, L.; Ou, Z.; Luo, B.; Xu, C.; Chen, Q. Machine Learning to Reveal Nanoparticle Dynamics from Liquid-Phase TEM Videos. *ACS Cent. Sci.* **2020**, *6* (8), 1421–1430. https://doi.org/10.1021/acscentsci.0c00430.

(12) Otsu, N. A Threshold Selection Method from Gray-Level Histograms. *IEEE Trans. Syst. Man Cybern.* **1979**, *9* (1), 62–66. https://doi.org/10.1109/TSMC.1979.4310076.

(13) Xiong, G. Local Adaptive Thresholding - File Exchange - MATLAB Central https://www.mathworks.com/matlabcentral/fileexchange/8647-local-adaptive-thresholding (accessed 2021 -08 -31).

(14) Mat Said, K. A.; Jambek, A.; Sulaiman, N. A Study of Image Processing Using Morphological Opening and Closing Processes. *Int. J. Control Theory Appl.* **2016**, *9*, 15–21.

Chapter 6: Revealing nanoscale structure and interfaces of polymer and protein condensates via Cryo-Electron Microscopy

6.1 INTRODUCTION

Liquid-liquid phase separation (LLPS) is a process through which a homogenous solution separates into two or more liquid phases. This phenomenon is observed in various systems including small molecules, polymers, peptides, and proteins. Protein phase separation is commonly observed in biological systems to carry out biochemical functions such as transcription, DNA repair, and chromatin organization.[1,2] Additionally, LLPS of polymers has various applications in other fields as well, including in chemical synthesis, development of new materials, energy storage and the food industry.[3] Consistent across these different modes of LLPS is the generation of liquid-like droplets composed of dense material within a dilute solution. Droplets are highly dynamic and can undergo fusion and fission events, exchanging material with their surroundings. The material properties of condensates can be described through measures including viscosity, interfacial tension, elasticity, and macromolecular diffusion, among others.[4] The function of condensates depends in part on their material properties, because these influence their form, molecular dynamics, partitioning of non-phase separating macromolecules, and interactions with other intracellular assemblies. In the case of naturally occurring protein-based condensates, a close connection between the viscosity of a condensate and its function has been identified. [5,6] That is, condensates need to be highly dynamic to operate as a reaction center, while rigidity can be important for functions such as storage, protection, or organization of components.[7] This range of behaviors exists condensates such as liquid-like stress granules versus gel-like centrosomes. Dysregulation of a condensate has been associated with neurodegenerative diseases and certain types of cancer.[6]

Recent work has made progress towards quantitatively describing the material properties of condensates, including their viscous and elastic components.[8] The liquid-like nature of droplets arises from the transient nature of intermolecular interactions including hydrogen bonds, hydrophobic interactions, and electrostatic interactions.[1] This implies that the material properties of condensates are governed by internal microstructures. However, we lack understanding of the internal structure of the condensates that result in these properties. Recently, Wu et al. have showed that proteins are distributed in-homogenously within condensates, creating hub-and-spoke-like percolated networks of molecules.[9] This observation was made by monitoring fluorescent probes that interact differently with hubs and voids. While useful, this study provides minimal information regarding the organization of proteins at these regions. Greater understanding of the internal structural features of these condensates is crucial for deciphering or designing their function and developing new strategies for controlling their behavior.

Several techniques can be applied to elucidate the nanoscale structure of condensates, including super-resolution microscopy,[10] small-angle X-ray scattering (SAXS),[11] and cryo-electron microscopy (cryo-EM).[12] Cryo-EM is emerging to be a powerful method for elucidating nanoscale condensate morphology because of its nanometer resolution and retention of native-like structure of the specimen. Recently, Zhang et. al studied teteranucleosome condensate forming mechanism using cryo-electron tomography (Cryo-ET).[13] They prepared specialized electron microscopy grids with a streptavidin layer for high specimen loading. Their data show a spinodal decomposition followed by a nucleation and growth mechanism of condensate formation. Furthermore, Mahamid and co-workers recently developed a method for cryo-EM of reconstituted condensates.[12] Their approach requires correlative light microscopy to explore preformed condensate specimens prior to electron microscopy. All these methods are impactful by enabling nanoscale elucidation of condensates. However, the requirement of special grids and additional steps like correlative light microscopy limits these approaches.

As the field of phase separation continues to grow, methodology, that is easily adaptable by non-experts, is required to expand the exploration of nanoscale condensate morphologies. Here we present a workflow for preparing cryo-EM samples of protein and polymer condensates by modifying routine cryo-EM sample preparation. We envision an acceleration of nanoscale understating of condensates as conventional cryo-EM methods get adapted by the condensate field. Our approach presented here is suitable to gain 2D and 3D information for any biomolecular or polymeric condensate.

6.2 RESULTS & DISCUSSION

To support the range of samples that can be studied using cryo-EM, we applied our technique to protein-based condensates with single and multiple components as well as polymer-based condensates. We focused on the RGG domain from LAF-1, a prototypical arginine/glycine-rich intrinsically disordered protein (IDP) involved in P granule assembly in C. elegans. LAF-1 RGG contains a diverse set of amino acids that promote several modes of interactions including electrostatic, π–π, and cation-π interactions.[14] The pattering of these amino acid sequences has shown a direct relationship to the material properties of their respective condensates.[15] Here, we explore two charge variants, RGG WT and RGG ShD, to visualize how the sequence patterning may affect the nanoscale organization of material within the condensates. Furthermore, we also use the combination of single stranded DNA and polyLysine to image multicomponent condensate, or complex coacervates. Complex coacervates of DNA and PLK have been used to prepare coacervates for nucleotide delivery and model systems to understand membranelles organelles.[16,17] Lastly, we also imaged block copolymer coacervates to visualize how two distinct blocks arrange within condensates. Simulation studies have shown that di-block copolymers can form structured liquid due to microphase separation of the two blocks, yet no experimental reports exist as of now.[18] In total we have imaged three different class of condensates/coacervates to show the generality of our developed approach.

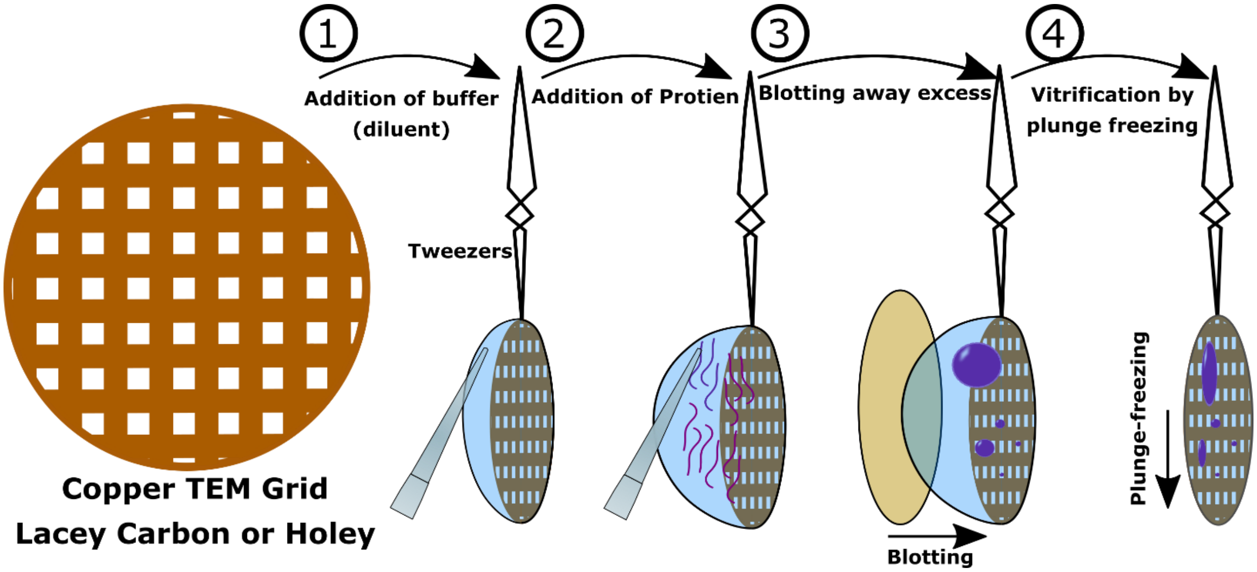

Figure 6.1: Overview of on-grid sample preparation for cryo-EM samples of RGG condensates (This may slightly vary each sample). In this procedure, phase separation was induced by reducing the salt concentration of the protein solution. In Step 1, we add the known amount of diluent to the grid. In Step 2, the protein solution is added, and the droplet formation is initiated. In Step 3 the excess solvent is blotted away for a known amount of time resulting in a thin layer of the specimen. In Step 4, the grid is plunged in a cryogen bath to vitrify the thin layer.

Condensate specimens were prepared following the steps summarized in Figure 1 and imaged using cryo-EM to elucidate nanoscale morphologies within the condensates. All protein cryo-EM specimens were prepared on-grid by first adding the buffer followed by the protein solution. The addition of the protein resulted in a lower final salt concentration which initiates the condensate formation. This allows the formation of condensate on-grid and vitrification of condensates in the nanoscale. Using this approach, condensate growth can be managed at different time points for the desired sizes and stages in the phase separation process. As seen in Figure 6.1, by waiting either between step 2 and 3 or between step 3 and 4, condensates can be grown before or after the blotting process. Ideally, if the goal is just for the condensates to start appearing, it is best to let the condensate grow after step 2. This is because any evaporation effects will be minimal at this stage, and the formation of droplets can be observed as the liquid on the grid can be seen turning turbid. Furthermore, if the protein or polymer is susceptible to shear induced morphological transition it is best to let the condensates grow after the blotting step.

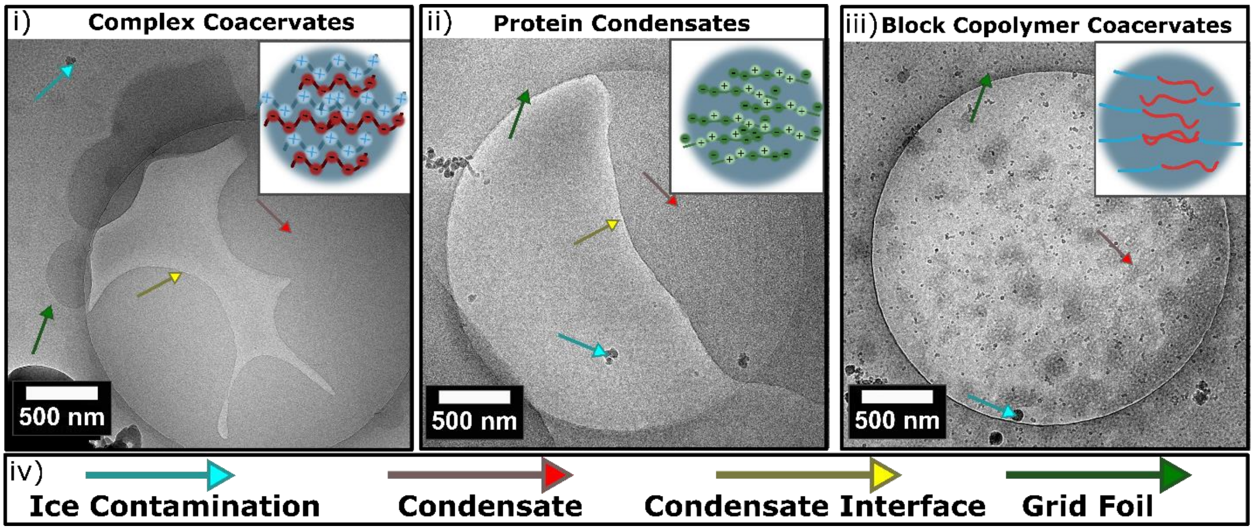

Figure 6.2: Cryo-TEM images of a variety of condensates/coacervates. i) Complex coacervates made of polyLysine (cationic) and single stranded DNA (anionic). ii) Protein condensate of RGG domain (polyelectrolyte). iii) Block copolymer coacervates of polyethylene glycol-*block*-polymethyl methacrylate polymer (non-ionic). iv) Legend for viewing cryo-EM micrographs and identify common features. Please refer to this for all micrographs presented in this publication.

We explored a series of condensates and coacervates to demonstrate that our sample preperation methods are effective for the most common classes of condensates: complex coacervate, protein condensate, and block copolymer coacervates (Figure 6.2). Here, the complex coacervates are made up of polyLysine and ssDNA. Protein condensates are of RGG and its charge variants, and the block copolymer coacervates are of polyethylene oxide-*block*-poly methyl methacrylate (PEO-*b*-PMMA). As shown in Figure 2i, complex coacervate condensates form and grow rapidly across the TEM grid. Additionally, the thin films of the condensed material show liquid like structure and a clear interface at the two-phase boundary. In Figure 2ii, RGG WT condensate show similar behavior in which large films of the condensed material are seen with a distinct interface, we follow our discussion of the interface and internal morphologies using the RGG condensates and its variants. Block copolymer coacervates are shown in Figure 2iii, in which the internal and interface of looks different from the others. This is due to the microphase separation of the two incompatible blocks which gives it the porous structure.[18] As seen in Figure 6.2 i&ii, complex coacervates and protein condensates show smooth, round edges of the thin film, showcasing liquid-like properties. On the other hand, block copolymer coacervates do not show a distinct edge of the condensed phase, which could be a result of a liquid to solid transition of the coacervate that we have observed before.[19]

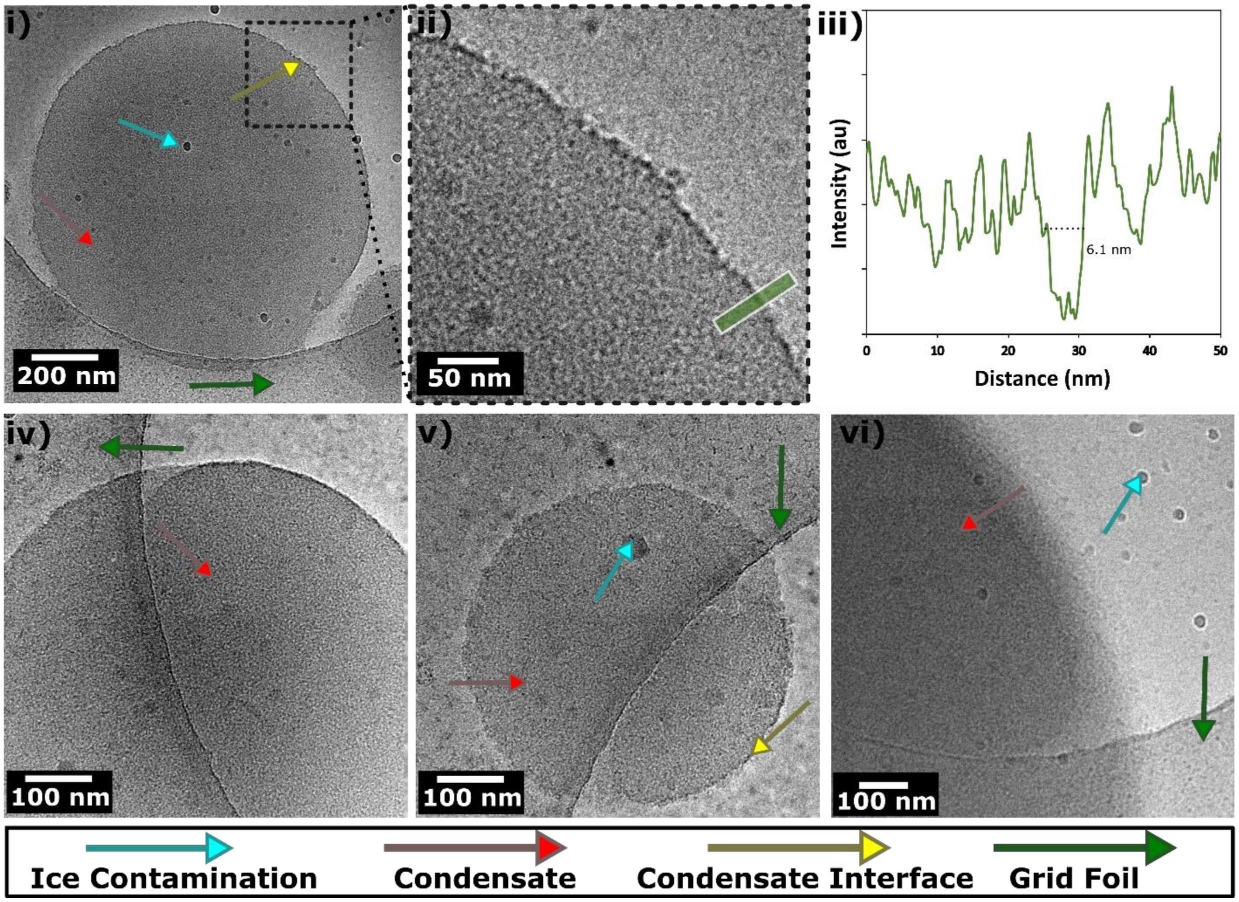

Figure 6.3: Interfaces of the condense phases. i) Image of RGG WT condensate, the higher magnification clearly shows the distinct interface (6.1nm) between the condensate and the dilute phase. ii) Close up of RGG WT thin film of the condensed material, the distinct interface can be seen between the condensed and the dilute phase. iii) Cross section intensity of the highlighted area to estimate the interface thickness, 6.1nm. iv-vii) Images of RGG WT showcasing distinct interface structures.

Biomolecular condensates are found responsible for important biological processes and disease formation. A term commonly used to describe such condensates is membrane less organelles (MLOs), as these droplets are found in cells with no lipid membranes.[20] While membrane bound organelles utilize the lipids at their interface to control partitioning of proteins and other biomolecules, MLOs achieve such control by non-specific interactions, and active reactions that can control size and chemical components of the condensates.[20] Inspired from synthetic droplet work, Stroberg et al. have suggested that interfaces of biomolecular condensates could be the local hubs for enhanced reaction efficiencies.[21] However, little is known about the interfaces of biomolecular condensate structure and morphologies. Recently, using Monte Carlo based simulations Farag et al. proposed the varying states of macromolecules within the condensates and at the interface.[22] Their simulations predict that proteins at the interface organize perpendicular to the center of mass of the droplet, resulting in a highly stretched confirmation which is very distinct from the conformation away from the interface. However, no experimental evidence of this prediction has been reported. Our experimental observations support these simulation claims as discussed below.

In our data, we find multiple examples of a distinct interface between the two phases which can resemble a membrane or a bilayer visually. As seen in (Figure 3) the interface boundary wraps the spherical droplet (Figure 3i) and is also present in the thin film of the condensed material (Figure 3ii). Measuring the interface of the condensates revealed the thickness to be close to that of a stretched out RGG protein(Figure 3iii), supporting recently published simulations.[22] Furthermore, we also observe inhomogeneity at the condensate interfaces as shown in Figure 3iv- vi. As seen in

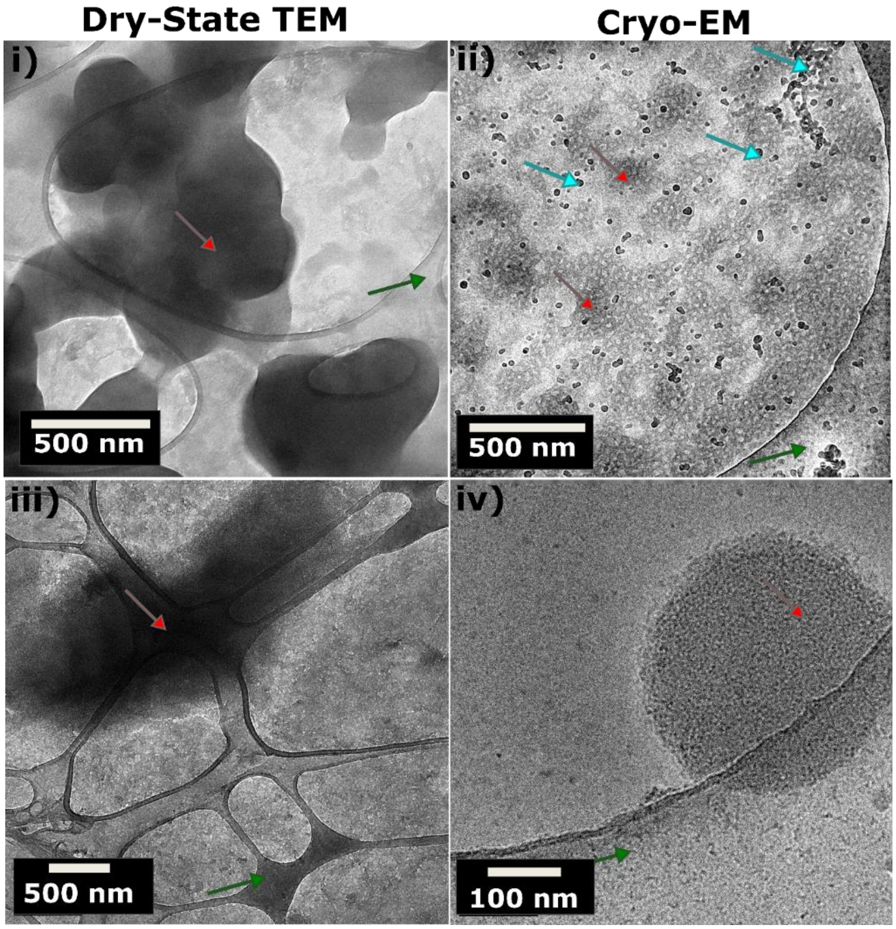

Figure 6.4: Comparison of dry-state TEM and Cryo-EM of protein condensates. i & ii) Comparison of dry state and Cryo-EM images of amphiphilic block copolymer coacervates. iii & iv) Comparison of dry state and cryo-EM images of RGG ShD variant condensates. In both examples, the morphologies of the condensates are conserved in the cryo-EM samples, while the dry state samples show no internal morphologies.

Figure 6.3iv, the interface is disconnected at the highlighted location, in Figure 3v the spherical condensate displays a patchy interface, and Figure 3vi shows an example of no distinct interface. We don’t have a clear understanding of these observations, but we hypothesize that multiple mechanisms could be at play during interface formation which can lead to the differences we can observe at the nanoscale. The distinct interface raises many questions about its function in relation to the cellular environment. Recent studies have shown enhanced activities and partitioning of biomolecules at the interface of condensates,[23] so moving forward, it will be crucial to relate these functional observations to the nanoscale structure at the two-phase interphase. To do this, cryo-EM approaches like the one presented here will be crucial.

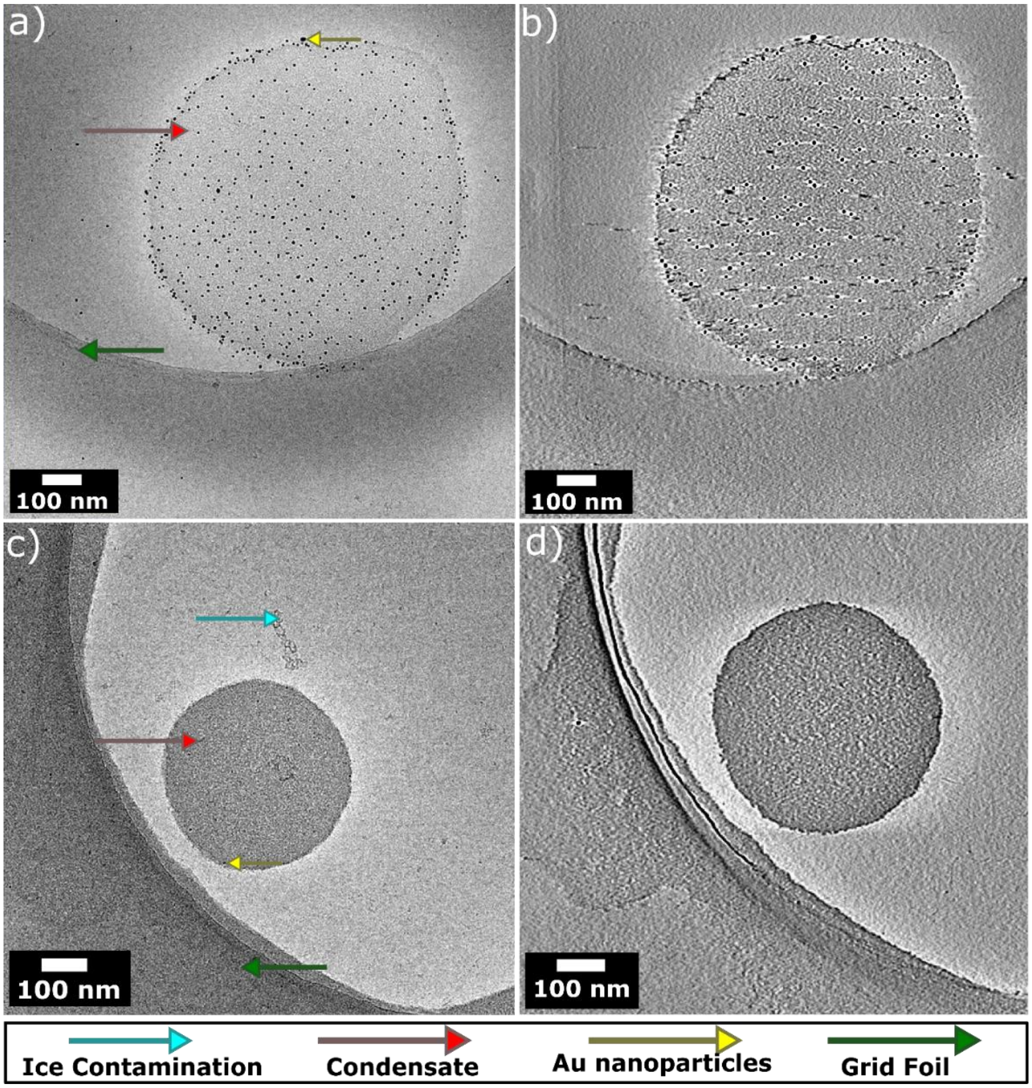

Figure 6.5: Cryo-electron tomography of ShD and WT RGG ShD. a) Image of a ShD RGG condensate with Au nanoparticles for tomographic analysis. b) Tomogram of central z-slices collected of the ShD RGG condensate from -65° to + 65°. c) Image of a WT RGG condensate with Au nanoparticles for tomographic analysis. d) Tomogram of central z-slices collected of the WT RGG condensate from -65° to + 65°.

While cryo-EM is the state of art electron microscopy methodology, often conventional TEM is still used in which the sample is dried out. It is well known that the drying of many macromolecular assemblies damages the native organization of them as they are held together by weak noncovalent interactions. Here, we examined the difference in the condensate structures after drying them. In Figure 3, we present the dried samples of protein and block copolymer condensates compared to their respective cryo-EM Image. In Figure 6.3i, the dried coacervates resemble solid particles with no preservation of the porous condensate structure as seen in Figure 3ii. Similarly, in Figure 3iii dried condensate of RGG ShD can be seen with no structure or shape as compared to the spherical droplet with internal structure seen in Figure 3iv. While dry-state TEM is often the easiest method, such studies stress the importance of not using dry-state TEM to infer condensate structure or sizes as the drying process destroys the native state of condensates.

Condensates have been shown to spatially organize cellular components, and within them structural heterogeneity has also been observed. However, the nanoscale structure of these organizations is yet to be explored. Being able to capture 3-D structure of condensates will further help us understand how condensates may organize its components, and what function this organization may play in cellular processes. To gain 3D structural information, we collected tilt-series for RGG condensates as shown in Figure 6.4. The series of images are then aligned to create tomograms which show features of the condensates in all planes. Figure 6.4a presents the 2D projection of a ShD condensate, the spherical condensate can be seen with a distinct interface. The dark spots on the condensate are gold nanoparticles which are used as fiducial markers that help align all frames during tomographic reconstructions. In Figure 6.4b the tomogram reconstruction of the central slices can be seen of the condensate. The distinct interface, and porous nature of the condensate can be visualized here as well.

Furthermore, we see similar behavior in the WT RGG condensate in Figure 6.4c, however, the droplet is of higher contrast signifying higher in protein concentration compared to its variant ShD RGG. The tomogram of it shown in Figure 6.4d clearly shows a network formation within the condensate without any order. The presence of such networks with voids has been predicted recently using Monte Carlo simulations of IDPs.[22] It was suggested that these voids immerge due to the regions of high versus low crosslinking densities for a given protein. We suspect that our data here is direct visual evidence of such predictions; however, more work will be needed to confirm this. Moving on, we will use the tilt-series collected above to create 3-D reconstruction models of the condensates for better visualization in 3D space.

6.3 CONCLUSION

Condensates and coacervates made from LLPS are droplets containing proteins or polymers within them. We have demonstrated here a simple workflow to prepare condensate specimen for cryo-EM imaging that can be used to gain 2D and 3D information. The wealth of information from these experiments is exactly what is needed to further our understanding of coacervates and biomolecular condensates on the nanoscale. We imaged 3 classes of phase separated droplets to show that this approach is adaptable for most materials. We discovered the presence of distinct interface which had only been predicted before computationally. Furthermore, we compared the outcomes of dry-state TEM and cryo-TEM in imaging condensates which showed that condensates lose structural integrity once dried out. Lastly, we used our specimens prepared to collect a tilt series which allowed for 3D analysis of the protein condensates. This revealed unique nanoscale network structure within the condensates which has not been experimentally reported before. With a wealth of knowledge already present about imaging biological samples and soft material using cryo-EM, we imagine this approach to be easily adapted. Future work will require nanoscale analysis like SAXS, cryo-EM imaging, and correlating material property characterizations to complete the structure-property-function relationship of biomolecular condensates.

6.4 References:

(1) Banani, S. F.; Lee, H. O.; Hyman, A. A.; Rosen, M. K. Biomolecular Condensates: Organizers of Cellular Biochemistry. *Nat Rev Mol Cell Biol* **2017**, *18* (5), 285–298. https://doi.org/10.1038/nrm.2017.7.
(2) Sabari, B. R. Biomolecular Condensates and Gene Activation in Development and Disease. *Developmental Cell* **2020**, *55* (1), 84–96. https://doi.org/10.1016/j.devcel.2020.09.005.
(3) Keating, C. D.; Pappu, R. V. Liquid–Liquid Phase Separation: A Widespread and Versatile Way to Organize Aqueous Solutions. *J. Phys. Chem. Lett.* **2021**, *12* (45), 10994–10995. https://doi.org/10.1021/acs.jpclett.1c03352.
(4) Wang, Z.; Lou, J.; Zhang, H. Essence Determines Phenomenon: Assaying the Material Properties of Biological Condensates. *Journal of Biological Chemistry* **2022**, *298* (4), 101782. https://doi.org/10.1016/j.jbc.2022.101782.
(5) Lee, K.-H.; Zhang, P.; Kim, H. J.; Mitrea, D. M.; Sarkar, M.; Freibaum, B. D.; Cika, J.; Coughlin, M.; Messing, J.; Molliex, A.; Maxwell, B. A.; Kim, N. C.; Temirov, J.; Moore, J.; Kolaitis, R.-M.; Shaw, T. I.; Bai, B.; Peng, J.; Kriwacki, R. W.; Taylor, J. P. C9orf72 Dipeptide Repeats Impair the Assembly, Dynamics, and Function of Membrane-Less Organelles. *Cell* **2016**, *167* (3), 774-788.e17. https://doi.org/10.1016/j.cell.2016.10.002.
(6) Mathieu, C.; Pappu, R. V.; Taylor, J. P. Beyond Aggregation: Pathological Phase Transitions in Neurodegenerative Disease. *Science* **2020**, *370* (6512), 56–60. https://doi.org/10.1126/science.abb8032.
(7) Feric, M.; Sarfallah, A.; Dar, F.; Temiakov, D.; Pappu, R. V.; Misteli, T. Mesoscale Structure–Function Relationships in Mitochondrial Transcriptional Condensates. *Proceedings of the National Academy of Sciences* **2022**, *119* (41), e2207303119.
(8) Alshareedah, I.; Thurston, G. M.; Banerjee, P. R. Quantifying Viscosity and Surface Tension of Multicomponent Protein-Nucleic Acid Condensates. *Biophysical Journal* **2021**, *120* (7), 1161–1169. https://doi.org/10.1016/j.bpj.2021.01.005.
(9) Wu, T.; King, M. R.; Farag, M.; Pappu, R. V.; Lew, M. D. Single Fluorogen Imaging Reveals Spatial Inhomogeneities within Biomolecular Condensates. bioRxiv January 27, 2023, p 2023.01.26.525727. https://doi.org/10.1101/2023.01.26.525727.
(10) Pandey, G.; Budhathoki, A.; Spille, J.-H. Characterizing Properties of Biomolecular Condensates Below the Diffraction Limit In Vivo. In *Phase-Separated Biomolecular Condensates: Methods and Protocols*; Zhou, H.-X., Spille, J.-H., Banerjee, P. R.,

Eds.; Methods in Molecular Biology; Springer US: New York, NY, 2023; pp 425–445. https://doi.org/10.1007/978-1-0716-2663-4_22.

(11) Martin, E. W.; Hopkins, J. B.; Mittag, T. Chapter Seven - Small-Angle X-Ray Scattering Experiments of Monodisperse Intrinsically Disordered Protein Samples Close to the Solubility Limit. In *Methods in Enzymology*; Keating, C. D., Ed.; Liquid-Liquid Phase Coexistence and Membraneless Organelles; Academic Press, 2021; Vol. 646, pp 185–222. https://doi.org/10.1016/bs.mie.2020.07.002.

(12) Tollervey, F.; Zhang, X.; Bose, M.; Sachweh, J.; Woodruff, J. B.; Franzmann, T. M.; Mahamid, J. Cryo-Electron Tomography of Reconstituted Biomolecular Condensates. In *Phase-Separated Biomolecular Condensates: Methods and Protocols*; Zhou, H.-X., Spille, J.-H., Banerjee, P. R., Eds.; Methods in Molecular Biology; Springer US: New York, NY, 2023; pp 297–324. https://doi.org/10.1007/978-1-0716-2663-4_15.

(13) Zhang, M.; Díaz-Celis, C.; Onoa, B.; Cañari-Chumpitaz, C.; Requejo, K. I.; Liu, J.; Vien, M.; Nogales, E.; Ren, G.; Bustamante, C. Molecular Organization of the Early Stages of Nucleosome Phase Separation Visualized by Cryo-Electron Tomography. *Molecular Cell* **2022**, *82* (16), 3000-3014.e9. https://doi.org/10.1016/j.molcel.2022.06.032.

(14) Wei, M.-T.; Elbaum-Garfinkle, S.; Holehouse, A. S.; Chen, C. C.-H.; Feric, M.; Arnold, C. B.; Priestley, R. D.; Pappu, R. V.; Brangwynne, C. P. Phase Behaviour of Disordered Proteins Underlying Low Density and High Permeability of Liquid Organelles. *Nature Chem* **2017**, *9* (11), 1118–1125. https://doi.org/10.1038/nchem.2803.

(15) Schuster, B. S.; Dignon, G. L.; Tang, W. S.; Kelley, F. M.; Ranganath, A. K.; Jahnke, C. N.; Simpkins, A. G.; Regy, R. M.; Hammer, D. A.; Good, M. C.; Mittal, J. Identifying Sequence Perturbations to an Intrinsically Disordered Protein That Determine Its Phase-Separation Behavior. *Proceedings of the National Academy of Sciences* **2020**, *117* (21), 11421–11431. https://doi.org/10.1073/pnas.2000223117.

(16) Marras, A. E.; Vieregg, J. R.; Ting, J. M.; Rubien, J. D.; Tirrell, M. V. Polyelectrolyte Complexation of Oligonucleotides by Charged Hydrophobic—Neutral Hydrophilic Block Copolymers. *Polymers* **2019**, *11* (1), 83. https://doi.org/10.3390/polym11010083.

(17) Abbas, M.; Lipiński, W. P.; Wang, J.; Spruijt, E. Peptide-Based Coacervates as Biomimetic Protocells. *Chem. Soc. Rev.* **2021**, *50* (6), 3690–3705. https://doi.org/10.1039/D0CS00307G.

(18) Statt, A.; Casademunt, H.; Brangwynne, C. P.; Panagiotopoulos, A. Z. Model for Disordered Proteins with Strongly Sequence-Dependent Liquid Phase Behavior. *The Journal of Chemical Physics* **2020**, *152* (7), 075101. https://doi.org/10.1063/1.5141095.

(19) Rizvi, A.; Patel, U.; Ianiro, A.; Hurst, P. J.; Merham, J. G.; Patterson, J. P. Nonionic Block Copolymer Coacervates. *Macromolecules* **2020**, *53* (14), 6078–6086. https://doi.org/10.1021/acs.macromol.0c00979.

(20) Gomes, E.; Shorter, J. The Molecular Language of Membraneless Organelles. *J. Biol. Chem.* **2019**, *294* (18), 7115–7127. https://doi.org/10.1074/jbc.TM118.001192.

(21) Stroberg, W.; Schnell, S. Do Cellular Condensates Accelerate Biochemical Reactions? Lessons from Microdroplet Chemistry. *Biophysical Journal* **2018**, *115* (1), 3–8. https://doi.org/10.1016/j.bpj.2018.05.023.

(22) Farag, M.; Cohen, S. R.; Borcherds, W. M.; Bremer, A.; Mittag, T.; Pappu, R. V. Condensates Formed by Prion-like Low-Complexity Domains Have Small-World Network Structures and Interfaces Defined by Expanded Conformations. *Nat Commun* **2022**, *13* (1), 7722. https://doi.org/10.1038/s41467-022-35370-7.

(23) Dai, Y.; Chamberlayne, C. F.; Messina, M. S.; Chang, C. J.; Zare, R. N.; You, L.; Chilkoti, A. Interface of Biomolecular Condensates Modulates Redox Reactions. *Chem* **2023**. https://doi.org/10.1016/j.chempr.2023.04.001.

(24) Schuster, B. S.; Reed, E. H.; Parthasarathy, R.; Jahnke, C. N.; Caldwell, R. M.; Bermudez, J. G.; Ramage, H.; Good, M. C.; Hammer, D. A. Controllable Protein Phase Separation and Modular Recruitment to Form Responsive Membraneless Organelles. *Nature Communications* **2018**, *9* (1), 1–12. https://doi.org/10.1038/s41467-018-05403-1.

(25) Elbaum-Garfinkle, S.; Kim, Y.; Szczepaniak, K.; Chen, C. C. H.; Eckmann, C. R.; Myong, S.; Brangwynne, C. P. The Disordered P Granule Protein LAF-1 Drives Phase Separation into Droplets with Tunable Viscosity and Dynamics. *Proceedings of the National Academy of Sciences of the United States of America* **2015**, *112* (23), 7189–7194. https://doi.org/10.1073/pnas.1504822112.

(26) Studier, F. W. Stable Expression Clones and Auto-Induction for Protein Production in E. Coli. In *Methods in molecular biology (Clifton, N.J.)*; 2014; Vol. 1091, pp 17–32. https://doi.org/10.1007/978-1-62703-691-7_2.

Appendix E: Supplementary for Chapter 6

E.1 Cryo-EM Imaging

CryoTEM Quantifoil Holey Carbon Films were purchased from Electron Microscopy Sciences, grids were glow discharged for 70 s to increase hydrophilicity prior to sample preparation. Vitrification was carried out by an Automatic Plunge Freezer ME GP2 (Leica Microsystems) where sample preparation onto cryoTEM grids was carried out at 95% humidity to prevent evaporation and blotted for (2, 3 or 4) s before autoplunging into liquid propane. Vitrified samples were studied on a JEOL-2100F TEM using a Schottky type field emission gun operating at 200 kV. Size measurements for cryoTEM images were performed using the measurement tool in ImageJ.

Block copolymer samples

Block copolymer solution (PEO_{45}-*b*-$PMMA_{300}$ in Dioxane 10 mg mL^{-1}) was applied to a glow discharge cryotome grid inside the humidity chamber at 95% relative humidity (RH). The samples were blotted (3s) and frozen without further changes to the system. The high humidity and hygroscopic nature of dioxane drives water absorption within the polymer solution which induces LLPS.

Complex Coacervates

Complex coacervate cryo-EM samples were prepared by mixing the individual solution of each polyelectrolyte on the grid and rapidly blotting and freezing the samples. In this case 2uL of ss DNA was first deposited onto the grid within the chamber. 2uL of PLK was then added and the droplet on the grid turned turbid immediately, indicating coacervate formation. The excess solution was blotted away (3s) and the sample was vitrified rapidly after that.

E.2 Protein Synthesis

RGG-RGG

MESNQSNNGGSGNAALNRGGRYVPPHLRGGDGGAAAAASAGGDDRRGGAGGGGY
RRGGGNSGGGGGGGYDRGYNDNRDDRDNRGGSGGYGRDRNYEDRGYNGGGGG
GGNRGYNNNRGGGGGGYNRQDRGDGGSSNFSRGGYNNRDEGSDNRGSGRSYNN
DRRDNGGDGEFGKLMESNQSNNGGSGNAALNRGGRYVPPHLRGGDGGAAAAASA
GGDDRRGGAGGGGYRRGGGNSGGGGGGGYDRGYNDNRDDRDNRGGSGGYGRD
RNYEDRGYNGGGGGGGNRGYNNNRGGGGGGYNRQDRGDGGSSNFSRGGYNNRD
EGSDNRGSGRSYNNDRRDNGGDGLEHHHHHH

Cloning

All genes of interest were cloned into pET vectors in frame with C-terminal 6x-His tags. RGG-RGG was cloned as previously described [24]. Other constructs were cloned by PCR and DNA assembly (NEBuilder HiFi DNA Assembly Master Mix; New England Biolabs). The RGG domain used here is the N-terminal IDR (residues 1-168) of C. elegans P granule protein LAF-1 [25]. Gene sequences were verified by Sanger sequencing (Genewiz).

Protein expression and purification

For bacterial expression, plasmids were transformed into BL21(DE3) competent E. coli (New England BioLabs). Colonies picked from fresh plates were grown for 8h at 37 °C in 1 mL LB + 1% glucose while shaking at 250 rpm. This starter culture (0.5 mL) was then used to inoculate 0.5 L cultures. For RGG and Shuffle proteins, cultures were grown in 2 L baffled flasks in Autoinduction medium (Formedium) supplemented with 4 g/L glycerol at 37 °C overnight while shaking at 250 rpm. The pET vectors used contained a kanamycin resistance gene; kanamycin was used at concentrations of 50 μg/mL in cultures [26]. After overnight expression at 18 ˚C or 37 °C, bacterial cells were pelleted by centrifugation at 4100 x g at 4 ˚C. Pellets were resuspended in lysis buffer (1 M NaCl, 20 mM Tris, 20 mM imidazole, Roche EDTA-free protease inhibitor, pH 7.5) and lysed by sonication. Lysate was clarified by centrifugation at 25000 x g for 30 minutes at 25 ˚C. The clarified lysate was then filtered with a 0.22 μm filter. Lysis was conducted on ice, but other steps were conducted at room temperature to prevent phase separation.

Proteins were purified using an AKTA Pure FPLC with 1 mL nickel-charged HisTrap columns (Cytiva) for affinity chromatography of the His-tagged proteins. After injecting proteins onto the column, the column was washed with 500 mM NaCl, 20 mM Tris, 20 mM imidazole, pH 7.5. Proteins were eluted with a linear gradient up to 500 mM NaCl, 20 mM Tris, 500 mM imidazole, pH 7.5. Proteins were dialyzed overnight at 45°C using 7 kDa MWCO membranes (Slide-A-Lyzer G2, Thermo Fisher) into physiological buffer (150 mM NaCl, 20 mM Tris, pH 7.5).

Proteins were snap frozen in liquid N_2 in single-use aliquots and stored at -80 °C.

For microscopy experiments, protein samples were prepared as follows: RGG protein aliquots were thawed above the phase transition temperature and diluted into the desired concentration with 20 mM Tris, 150 mM NaCl, pH 7.5 buffer. Protein concentrations were measured based on their absorbance at 280 nm using a Nanodrop spectrophotometer (ThermoFisher); RGG and shuffle proteins were mixed in a 1:1 ratio with 8 M urea to prevent phase separation during concentration measurements.

SDS-PAGE

For chromatographically purified proteins, SDS-PAGE was run using NuPAGE 4-12% Bis-Tris gels (Invitrogen) and stained using a Coomassie stain (SimplyBlue SafeStain; Invitrogen).

Image Processing

Image J was used to manipulate all cryo-EM images.

Chapter 7: Conclusion

This thesis has explored how liquid-liquid phase separation of block copolymers can influence self-assembly. In Chapter 2 the first system of stable block copolymer coacervate was presented and it was discovered that the coacervate phase encodes information of the final self-assembled structures as the block copolymers change phases. The caocervates was also shown to be a modular liquid-precursor that can be used to access self-assembled structures on varying length scales from nanoscale to macroscopic scale. In Chapter 3, it is shown that LLPS during the self-assembly of block copolymers can induce confinement effects producing unique structures. This mechanism has not previously been reported, but it could enable the development of new ways to access confined block copolymer morphologies that are typically made with energy intensive procedures. In Chapter 4, a system was developed that undergoes LLPS as the block copolymer is synthesized inspired by biological phase separation and known PISA processes. This process was titled polymerization induced condensation (PICON). The encapsulation of small molecules and gelation was further explored during the PICON process. Systems based on this process may be created that behave like active biological systems that also phase separate. In Chapter 5, LP-TEM was used to observe a new mechanism for supported bilayer formation. It was shown that, upon LLPS, block copolymer coacervates spread onto a surface more easily compared to when vesicles first form and spread. The knowledge of this mechanism will allow the development of new synthesis of supported bilayers with minimal defects. In Chapter 6, a workflow was developed to image the macromolecular organization within phase separated droplets of proteins and polymers using cryo-TEM. Unique network morphologies were observed inside the phase separated droplets and distinct interfaces at the two-phase boundaries which have only been predicted by simulations before. Use of this approach will accelerate further research in understanding condensate structures on the nanoscale, a front of research that is under explored.

Future work on understanding phase separating systems should focus on the nanoscale structures within the droplets. Many properties of such droplets, like adhesion, surface tension, encapsulation, are all related to the structure present at the nanoscale. Electron microscopy methods like cryo-TEM and LP-TEM will be crucial in understanding nanoscale structure and dynamics. However, in addition to these microscopy methods, bulk measurement, like X-ray scattering, viscos-elastic behavior, and permeability of these materials should be measured to develop structure-property relationships. The development of this research will directly aid in better understanding biological processes that also undergo LLPS and form similar materials.